Stability and Control of a Morphing Vehicle

Thomas S. Koch

A thesis
submitted in partial fulfillment of
the requirements for the degree of

Master of Science in Aeronautics and Astronautics

University of Washington

2012

Committee:

Juris Vagners

Kristi Morgansen

Stefan Bieniawski

Program Authorized to Offer Degree:
Aeronautics & Astronautics

University of Washington

Abstract

Stability and Control of a Morphing Vehicle

Thomas S. Koch

Chair of Supervisory Committee:
Professor Juris Vagners
Aeronautics & Astronautics

Air vehicle design is a study in compromises. Aircraft configurations are optimized to perform at one point in their flight envelope at the expense of performance at off nominal flight conditions. Two wildly different missions require two wildly different vehicles or one vehicle that does not perform either mission optimally. Morphing refers to the ability of an aircraft to significantly change its aerodynamic configuration to meet disparate mission requirements or optimize its performance based on changing flight conditions. Accomplishing this goal relies on technologies that touch every area of aerospace engineering including shape changing structures, configuration optimization, and stability and control.

Here, the latter of these will be addressed. A configuration is developed that is capable of significant configuration change. The bare airframe stability characteristics are determined using a vortex lattice code in each nominal configuration. An outer loop and guidance controller are developed to allow for autonomous flight in the Boeing Vehicle Swarm Test Lab (VSTL). The vehicle dynamics are augmented with inner loop controllers in the lateral and directional axes. A simple nonlinearity is introduced to represent a nonlinearity that may be present during configuration changes. An adaptive control scheme is employed to maintain stability and performance during the transition between the nominal configurations in the presence of the nonlinearity. Autonomous flight tests of static configurations were performed to validate the aerodynamic code and control design techniques.

TABLE OF CONTENTS

LIST OF FIGURES

LIST OF TABLES

Chapter 1 - Introduction

Morphing refers to technologies that enable an aircraft to change its aerodynamic configuration significantly to allow performance optimization over a large portion of its flight envelope or in changing environmental conditions. Morphing can also be used to allow a single vehicle to perform multiple disparate missions. Current airframe designs are optimized for a handful of critical points in the flight envelope; and for the rest of the envelope, the configuration is a compromise. Morphing aims to allow designers to create configurations that are optimal over a majority of the flight envelope, thereby increasing overall mission performance and efficiency.

Some of the challenges that must be overcome to enable morphing include material technologies to allow for dramatic shape changes, actuation technologies capable of performing the required movements while not adding significant weight to the vehicle, and modeling, simulation, and control techniques to allow for safety and maneuverability across a wide range of configurations. This thesis addresses the last of those areas, namely the design and implementation of a controller to allow safe and stable autonomous flight across multiple configurations while maintaining satisfactory performance.

Background

The idea of changing aerodynamic configurations to obtain better performance over a wide range of flight conditions is not a new concept. Some older fighter aircraft such as the F-111 and F-14 featured wings with variable sweep angles to allow better performance for high-speed flight. This feature has not been included on a large number of aircraft because the mechanisms to actuate such a system are heavy, costly, and complex. Most transport category airplanes feature high lift devices such as flaps and slats that can be deployed during takeoff and landing to boost performance during low speed flight. More recently, the Boeing 787 was outfitted with a system that allows these same devices to be repositioned during cruise as the weight, altitude, and speed vary to optimize aerodynamic efficiency [1].

While these features meet some of the objectives of morphing, they do not meet the definition of morphing as laid out by DARPA in their Morphing Aircraft Structures (MAS) project [2]. The MAS program was focused on large-scale planform alterations including:

- 200% change in aspect ratio
- 50% change in wing area
- 50% change in wing twist
- 20 degree change in wing sweep

DARPA's definition of morphing is vehicles that:

- Change state substantially to adapt to changing missions and mission environments
- Provide superior system capability not possible without reconfiguration
- Designs that integrate innovative combinations of advanced materials, actuators, flow controllers, and mechanisms to achieve the required state change.

The main contractors working on the MAS project are Raytheon, NextGen Aeronautics, and Lockheed Martin. Figure 1-1 shows a picture of the NextGen Aeronautics UAV that is capable of large-scale shape change.

Figure 1-1: NextGen morphing wing UAV

Figure 1-2 shows the Lockheed Martin study aircraft.

Figure 1-2: Lockheed Martin “Z-Wing” morphing concept vehicle

These vehicle configurations and others have been the topic of research on various aspects of the design. The following sections briefly cover some of the trends in the areas of research relevant to this thesis.

Modeling and Simulation

A great deal of work has been done on developing the equations of motion and aerodynamic models required to successfully design and model morphing aircraft [2] [3] [4]. The main differences in dynamic modeling of morphing aircraft as related to more conventional configurations can be summarized by three main points:

First, the center of gravity and moments of inertia can change significantly with large-scale shape changes. This means that extra moment and force terms appear in the standard equations of motion and the inertia tensor becomes a function of time that has dynamics that can be close to the frequency ranges of the rigid body dynamics. Research in this area has led to several well-developed models of the aircraft equations of motion that either treat the vehicle as a single non-rigid body, or as a collection of several rigid bodies.

The second major difference is that the aerodynamic forces and moments become not only a function of the flight conditions and Euler angles, but also the state of the morphed configuration. For morphing designs with a large number of configuration degrees of freedom, this can make the standard database build up of aerodynamic force and moment coefficients intractable [3]. One solution to this has been to solve for the aerodynamic forces and moments at each time step of the simulation using a vortex lattice method [3].

Finally, if the morphing rate is sufficiently fast, unsteady aerodynamic forces can come into play. Some work has been done to create “pseudo-steady” vortex lattice methods to take this effect into account [3].

Control Methods

A couple of directions can be taken when considering control of a morphing aircraft. First, morphing can be thought of as a configuration change requiring different controllers at each configuration. Alternatively, morphing can be studied as the method of dynamic control in lieu of conventional effectors [5]. Using configuration changes as control effectors can result in non-unique solutions if the number of degrees of freedom of the morphing is large. The solutions for different control inputs would become functions of their initial conditions. Work has been done in this area to find optimal control allocation based on “least control energy” solutions [5].

In [5] the author tackles the configuration change control problem by treating each morphed state as separate control problems then using gain scheduling for the transition periods. In [6] the same author delves deeper and designs nonlinear dynamic inversion controllers and suggests that adaptive methods could also be useful.

Approach

In this work, lower order aerodynamic modeling techniques were used and robustness to model variation was ensured through control law design. Because of the difficulties and the time that would be required to accurately model and simulate a morphing vehicle, the aerodynamics were modeled using a steady state vortex lattice code. Morphing was limited to a small number of degrees of freedom and assumed to only change from configuration to configuration occasionaly to simplify the effect on the dynamics, and enable a simple prototype to be built. The system was simulated as a linear parameter varying system (LPV) that varies as a function of the morphing configuration. Nonlinear and unsteady inertial and aerodynamic effects introduced by morphing were ignored during controller design as the lower order aerodynamic models do not sufficiently capture their contribution. Gain and phase margins are kept large to make the controllers robust to the presence of these effects.

The focus of this thesis is the control of a vehicle as it goes through configuration changes via morphing rather than on the use of morphing aerodynamic surfaces as control effectors. The strategy is to design controllers using linear methods that are sufficiently robust to the nonlinear and unsteady effects that exist in the actual vehicle.

In order to better understand the complexities involved with actual implementation of morphing aerodynamic configurations and the suitability of the low order aerodynamic modeling used here, flight tests were performed. Flight tests were enabled by the use of the Boeing Vehicle Swarm Technology Lab (VSTL). The VSTL is an indoor flight test facility used for the rapid prototyping and testing of flight configurations for use in research in guidance, navigation, and control and swarm technologies as documented in [4]. Moving directly to a low cost flying model has the advantage of capturing all of the non-linear effects mentioned above without the time, cost, and complexity associated with completely modeling such a vehicle.

This thesis project consisted of three major steps. The first step, documented in Chapter 2, was the preliminary design of a morphing configuration capable of significant aerodynamic configuration change. Three nominal configurations were designed: a representative low-speed configuration, an intermediate configuration for increased stability, and a high-speed configuration. The design was evaluated using a vortex lattice aerodynamic code to generate basic aerodynamic stability and control data.

Chapter 3 documents the design of control laws to augment the bare airframe dynamics and enable autonomous flight. Controllers were designed at each of the nominal configurations based on the vortex lattice results, and gain scheduling was used to maintain control of the vehicle at off-design configurations and during configuration changes. A linear simulation of the vehicle as a linear parameter varying (LPV) system was built based on the vortex lattice aerodynamic results and used to analyze the controllers at each of the individual configurations, as well as during the transition periods.

The final part of the project was the construction and flight test of low cost prototypes in the Boeing VSTL and is documented in Chapter 4. The flight tests were used to verify the VLM generated aerodynamic models, and show that the controllers designed using the linear models in Chapter 3 translate well to the real world. Chapter 5 summarizes the project and offers some direction for possible future work.

Chapter 2 - Configuration Design

This chapter covers the development of the baseline configuration of the morphing vehicle on which the remainder of this project was based. Initial sizing and configuration of the vehicle developed here was based on several factors:

- Review of previous configurations from morphing studies
- Ease of assembly and kinematic implementation
- Constraints of flying vehicles in the VSTL
- Results of vortex lattice aerodynamic modeling
- Results from glide tests

Initial sizing was based on rough estimates of weight, thrust, and flight speed. Then a rough sketch of a configuration that met these sizes was created based on previous examples and brainstorming. These initial configurations were then run through a vortex lattice code that estimates aerodynamic forces and moments and trim requirements. Finally models of the configurations were constructed for glide tests to confirm the analyses. The goal was not to create an optimized configuration, but rather to create a solid configuration that served the needs of the rest of the project.

Requirements

For this project, the aim was to create a configuration that significantly changes its configuration. The change in configuration should be significant enough that a controller designed for one configuration will not have adequate performance in the other configuration. The high level requirements for the vehicles are:

- Exhibit a significant and interesting configuration change
- Easy to manufacture
- Capable of autonomous flight in the Boeing Vehicle Swarm Technology Lab (VSTL)
  - Low stall speed (less than ~7 m/s)
  - Minimum turn radius less than ~8 m
  - Carry propulsion, telemetry, and control system that weighs approximately 150g

Previous Morphing Vehicle Concepts

The focus of most morphing vehicles has been on changing the main parameters of wing planform such as area, chord, sweep, camber, twist, and dihedral. Camber and twist are relatively difficult to implement from an actuation and structural standpoint, so the configuration studies for this project focused on the others. In particular, dihedral was varied significantly in this study.

Fixed wing vehicles that are flown in the VSTL are generally lightweight, fly slowly, and are constructed from Depron foam board. Depron is a foam material that is widely available. Most configurations consist of flat plate aerodynamic surfaces. This material eases construction significantly, but also limits configuration complexity and performance.

From reviews of previous work, the concept that fits into this construction framework most readily is the "Z-wing" concept developed by Lockheed Martin for the DARPA morphing aircraft project. Lockheed's concept is shown in Figure 1-2 above. This basic configuration concept served as the starting point for the configuration developed for this project. Compared to the Z-wing aircraft, the configuration developed features an additional dihedral break that creates a more interesting and bird like configuration as is discussed later in this section.

Configuration Sizing

The basic low speed configuration sizing was based on constraints presented by the equipment available in the VSTL and general rules of thumb regarding aircraft performance from flying other MAV's in the limited physical space available in the VSTL. The weight estimate for the initial sizing studies was based on weights of previous vehicles flown in the VSTL as well as the known density of Depron foam from the manufacturer's website and confirmation from weighing of the actual material. The rough estimates for the preliminary design included safety factors to make sure that once the vehicle was assembled, it would still be flyable in the VSTL.

Foam Structural Weight

From the manufacturer's website [7], Depron foam weighs approximately 80 grams/m^2 for the 3mm thickness foam that is generally used to construct vehicles in the VSTL. For all of the sizing done here, this figure was doubled to allow for the chance that the vehicle needs to use thicker foam than the 3mm standard, or that structure must be added to increase the rigidity of the vehicle

Fuselage

The purpose of the main body section of the vehicle is to serve as a mounting location for the electronics and propulsion system. Here the fuselage also contained the actuation components for the morphing mechanisms, and was used to contribute to the total lift of the vehicle. The fuselage length was set to 500mm and the width taken as 250mm. Based on the 80 grams/m^2 for 3mm Depron, the fuselage weight was estimated to be approximately 10 grams. With the 100% safety factor, this becomes 20 grams.

Wings

Previous experience has shown that a good maximum flight speed for vehicles in the VSTL is 7 m/s; if they go much faster, they have trouble in the enclosed space of the lab. With this in mind, 6 m/s was used as the design airspeed. The wings were sized using the design airspeed, sea level atmospheric conditions, a first guess weight estimate of 400 g, and a reasonable C_L range (~0.50 to 0.75). Based on these initial guesses, the estimated wing area required was found by solving the lift equation for wing area and was found to be approximately 0.3 to 0.5 m^2. Because the fuselage plate also acts as a lifting surface, its planform area of 0.125 m^2 is included in the reference area.

Initial wing dimensions were found by simply sketching the planform to scale until the vehicle looked about right and had the required amount of total wing area. For the inboard wing sections, a couple of iterations of span and chord lengths led to the final dimensions of a root chord of 350 mm, a tip chord of 250 mm and a span of 150 mm. This gives a surface area of 0.045 m^2 per side for a total of 0.090 m^2. The outboard wing sections have a 250 mm root chord, a 200 mm tip chord, and a span of 250 mm for an area of 0.0563 m^2 per side and a total of 0.1126 m^2. Finally, tip extensions were added that have a root chord of 200 mm and tip chord of 150 mm and a span of 100 mm for an area of 0.0175 m^2 per side and a total of 0.035 m^2. The addition of all these components brings the total wing surface area to 0.3626 m^2, which falls within the required wing area estimate from earlier. This was the initial configuration that was evaluated using the vortex lattice method (VLM) in the following sections. The total wing weight estimate (not including the fuselage weight) based on 80g/m^2 came to approximately 19 grams. With the safety factor, this becomes 38 grams. Based on this wing weight estimate and the weight estimate for the fuselage above, the total weight estimate for the foam came to 58 grams.

Propulsion and Control System Weight

The weight of the "Disk" vehicle shown in Figure 2-1 was used as the starting point. This vehicle weighs roughly 170 grams and based on the surface sizes, and Depron foam density, the foam structure weighs approximately 15 grams. Therefore the remaining components consisting of the motor, propeller, battery, and control electronics are approximately 155 grams.

Figure 2-1: Disk aircraft flown in VSTL

The components used on the Disk are largely similar to what was used on the configuration for this project. Since the vehicle is slightly larger overall, however, it may require a larger propulsion or control system. To compensate, a 50% increase over the disk vehicle's component weight was used as the baseline. This makes the baseline component weight 233 g.

Morphing

One of the strengths of this configuration is the ease of implementing morphing. With three individual wing panels per side the angles between each panel can be varied in any number of ways to change the performance and stability characteristics of the vehicle. In the original Z-Wing design concept, the morphing was implemented by simply rotating the inboard wing section relative to the fuselage while maintaining the outboard wing angles relative to the fuselage constant. This allows for a low-speed loiter type configuration with all of the wing panels flat, and a high-speed configuration with the wings folded in to reduce the wing area. This type of morphing is easily accomplished with the configuration presented here.

Further inspiration can be drawn from the flight of birds. Wings in nature are almost infinitely morphable and are used for all aspects of flight. A great example of a bird with morphing characteristics similar to that of the Z-Wing concept is the Peregrine Falcon. Figure 2-2 shows pictures of a Peregrine Falcon in a low-speed configuration and a high-speed configuration similar to those of the Z-wing aircraft.

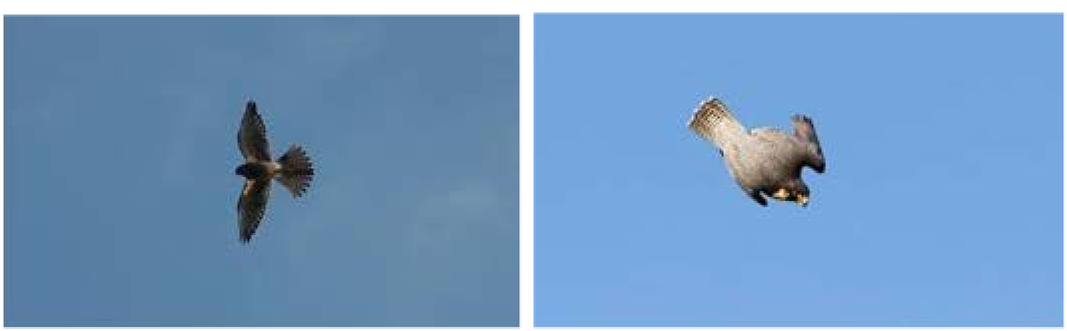

Figure 2-2: Peregrine Falcon in a low-speed soaring configuration (left) and in a high-speed dive configuration (right)

Birds also often use a third intermediate configuration when they are soaring in gusty conditions. In this instance, the inner portions of the wings are raised and then the wings gradually bend down towards the tip. This is the so-called gull-wing configuration. A seagull is shown in this state in Figure 2-3.

Figure 2-3: Seagull with wings in the “gull-wing” configuration

This type of configuration could also be useful to small lightweight UAV’s that are easily disturbed by gusts. The configuration concept developed here is readily adaptable to include this type of configuration as an intermediate position between the low-speed and high-speed configurations. For this configuration, the inboard wing sections are rotated to 45 degrees, the outboard wing sections remain flat, and the wing tip sections are rotated down 45 degrees. This configuration leaves most of the wing area of the low-speed configuration intact, while adding directional stability and, as will be shown later, increased directional control power with the addition of dihedral. Figure 2-4 shows unpowered glide models of the three design configurations.

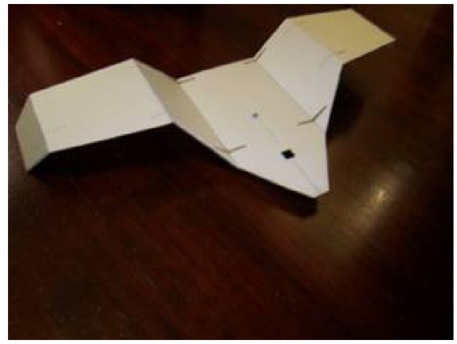

(a) (b)

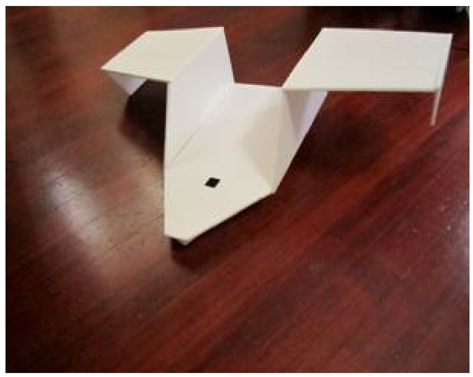

(c)

Figure 2-4: Glide models of (a) low-speed (b) gull wing and (c) high speed configurations

To make the three configurations more easily implementable and analyzable, the concept was to have the wing tip sections rotate through the same angle as the inboard wing sections, but in the opposite direction. This means the morphing configuration of the wings is completely defined by a single degree of freedom, which will be referred to as the "morph angle" and designated by the symbol μ. In the low-speed configuration, the wing sections are completely flat relative to the fuselage and μ is 0. As morphing begins, the inboard wing sections rotate upward, the outboard wing sections remain flat relative to the fuselage and the wing tips rotate downwards. When the morph angle reaches 45 degrees, the vehicle is in the increased stability gull-wing configuration. As the morph angle continues to increase, it will eventually reach the high-speed configuration with μ=90 degrees. In this configuration, the inboard wing sections are vertical, the outboard wing sections are still flat relative to the fuselage, and the wing tip sections point vertically down. This transition can be seen in Figure 2-5.

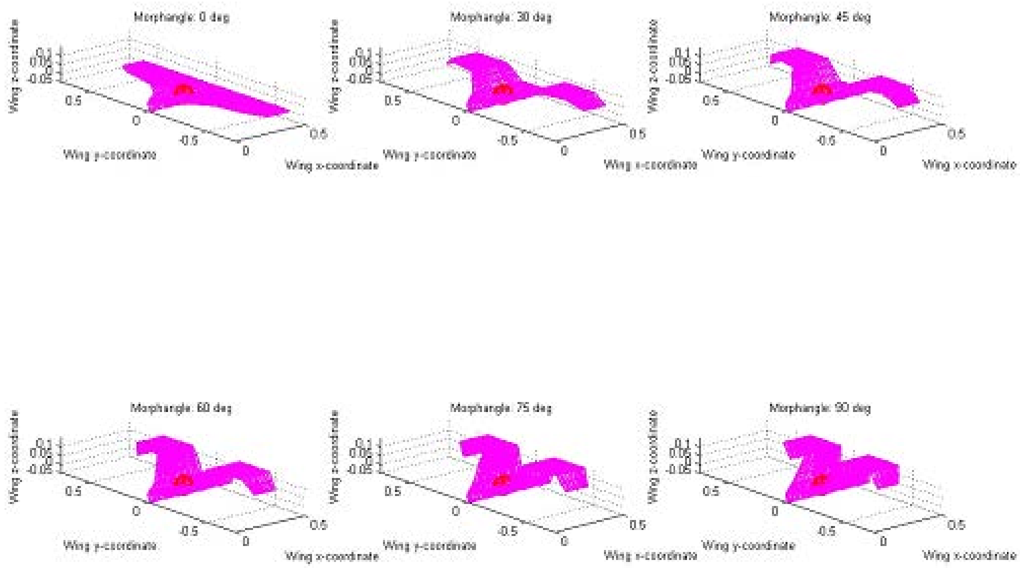

Figure 2-5: Configuration transition. Upper left is low-speed configuration and lower right is high-speed configuration

The overall configuration change results in a 34% change in the total wing area between the low-speed and high-speed configuration. The morphing mechanism will likely require the addition of 1 or 2 servos and some mechanical linkages that will add weight to the total configuration. The servos in standard use on vehicles in the VSTL weigh approximately 6 grams each. Assuming that the configuration will need 2 servos and adding in approximately 10 grams for the mechanism, gives an added weight of 22 grams.

Initial Configuration

The total weight estimate based on the above comes out to be 313 grams. Since this is lighter than the weight estimate used to size the wing surfaces, the vehicle will be able to generate sufficient lift in the low-speed configuration at 6 m/s. The C_L at the estimated weight and 6 m/s comes out to be 0.41. The wing area of the high-speed configuration is roughly equal to the low-speed configuration wing area minus the inboard wing area and wing tip wing area. In this configuration the wing area is 0.2376 m^2. Based on this wing area and the 313 gram weight estimate, the vehicle generates enough lift for level flight at 6 m/s at a C_L of 0.63, which is reasonable. Table 2-1 contains a summary of the important parameters for the low-speed and high-speed configurations.

Table 2-1: Configuration parameters for high-speed and low-speed configurations

	Low-Speed	High-Speed
Weight	313 grams	313 grams
S	0.3626 m^2	0.2376 m^2
b	1.25 m	0.75 m
$\mathbf{V_{cruise}}$	6 m/s	6 m/s
$\mathbf{C_{L,cruise}}$	0.41	0.63

Once the powered flight models were built and weighed, the total weight came out to approximately 350 grams, somewhat higher than the values in Table 2-1. This weight was used in aerodynamic analyses that follow and the results indicate that the vehicle is still flyable at 6 m/s at this weight.

Vortex Lattice Code

After the initial sizing exercise described above, the configurations were built and run through a vortex lattice code and associated analyses were run to confirm the suitability of the configurations. The underlying vortex lattice method (VLM) code was first developed by Uy-Loi Ly at the University of Washington. Dr. Ly and other members of the Boeing Research & Technology Guidance, Navigation, and Control group in Seattle, Washington subsequently added additional features and analysis routines to the package. The code has been used extensively in the design and analysis of MAVs for use in the VSTL, see [4] for example. The code includes the capability to model engine thrust and control effector mixing schemes. The following sections cover the background of the vortex lattice method employed followed by a discussion of the analyses performed on the initial configurations and their results.

Vortex Lattice Method Theory

The vortex lattice method (VLM) is a computational fluid dynamics routine that relies on the superposition principle to calculate the forces and moments acting on a vehicle in flight. The method is based on the assumption that the flow around an aircraft is a potential flow; that is that the flow field is irrotational and the velocity field can be described as the gradient of a scalar function known as the velocity potential function. Further it assumes that the fluid is incompressible, inviscid, and steady. Thus the velocity potential function satisfies Laplace's equation. These assumptions have been shown in practice to apply well to a large number of engineering problems, including the flow around a subsonic airfoil at small angles of attack. Because the solutions to Laplace's equation are linear, the super position principle holds. The vortex lattice method takes advantage of this fact by dividing a complex geometry into simple geometries represented by flow singularities (horseshoe vortices) with known solutions and then using super position to solve for the entire flow field.

The method has three main steps: 1) Describe the vehicle geometry as a combination of flat plates and attach a horseshoe vortex to each flat plate, 2) setup flow tangency boundary conditions, use the Biot-Savart law to calculate the influence of each vortex on each plate, and simultaneously solve the flow tangency boundary conditions at every panel to find the strength of each vortex, 3) use The Kutta-Joukowski theorem to calculate the forces on each panel due to the vortices and sum the forces on each plate to find the total force and moment. More in depth information can be found in [8] which describes the historical development of the method and a description of the method as implemented in the code used here can be found in [9].

VLM Limitations

A brief discussion of the limitations of the vortex lattice method as they apply to this project is in order. There are three main issues that have an impact on this project:

1. The vortex lattice method is most applicable at small angles of attack that have little or no flow separation.
2. The VLM code used here does not have a profile drag model, so drag figures for the overall configuration, and individual components are likely to not be accurate.
3. The results only apply to steady flow conditions.
4. The code does not accurately calculate the effect of blowing on control surfaces.

As is seen in Table 2-2 below, item 1 above could be of concern because the vehicle flies at somewhat high angles of attack, especially in the high-speed configuration. This could prove to be troublesome, but experience with the code and flying other vehicles in the VSTL (the disk in particular) indicate that while the results may not be perfect, they are typically good enough to use for control law design and analysis. Item 2 is of concern because as will be discussed in the section on control mixing that follows, differential drag is the main method of imparting a yawing moment on the airplane in the low-speed configuration. Item 3 means that while the results shown here are valid while the morph angle remains constant or changes slowly. Fast morphing would likely create some non-steady aerodynamic effects that are not accurately modeled with the VLM method. Item 4 will have an impact on the accuracy of the elevator control power derivatives. On the powered model, the elevator is placed directly in the propeller wash and thus could be more effective than predicted.

Preliminary Analyses

Once the geometries are created, the tool is capable of performing a number of analyses including giving aerodynamic forces and moments at given flight conditions and configurations, calculating trim conditions at a given speed, and linearizing the model about a trim point for use in control law synthesis. For the initial configuration investigations, the low-speed, gull-wing, and high-speed configurations were run through level flight trims as a reality check to the results found in Table 2-1. All conditions result in reasonable trim conditions. The results are summarized in Table 2-2.

Table 2-2: Vortex lattice code trimmed flight conditions with CG at 26 cm

	Low-Speed	**Gull Wing**	**High-Speed**
Airspeed	6 m/s	6 m/s	6 m/s
C_L	0.4	0.5	0.6
Angle of Attack	10.5 deg	10.7 deg	17.3 deg
Elevator Deflection*	-24 deg	-14 deg	-15 deg

* Positive elevator deflection is trailing edge down (airplane nose down). See Figure 2-9 to see elevator configuration

As is shown in the tables, the results of the VLM code match the preliminary results from Table 2-1 well, which implies the methods are sound. Figure 2-6, Figure 2-7, and Figure 2-8 show the normalized trimmed lift distribution in the high-speed, gull wing, and low-speed configurations respectively as determined by the VLM routine.

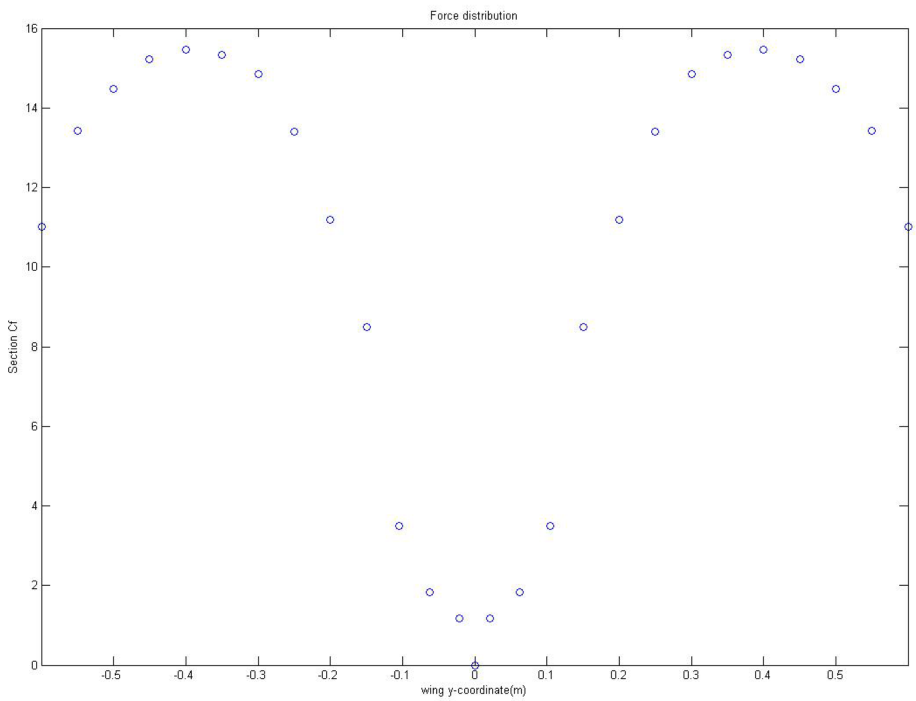

Figure 2-6: Trimmed lift distribution for the low-speed configuration at 6m/s and CG at 26 cm

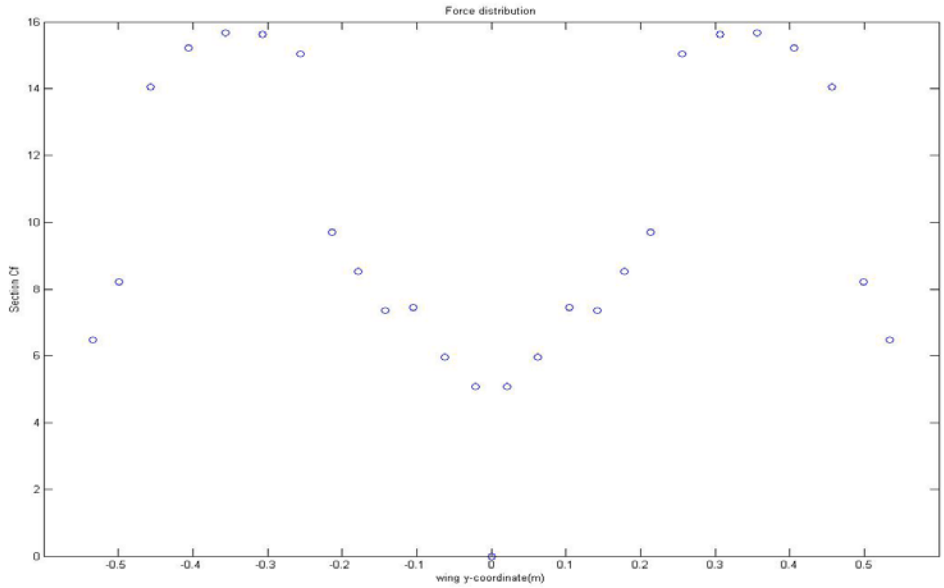

Figure 2-7: Trimmed lift distribution for the gull-wing configuration at 6 m/s and CG at 26 cm

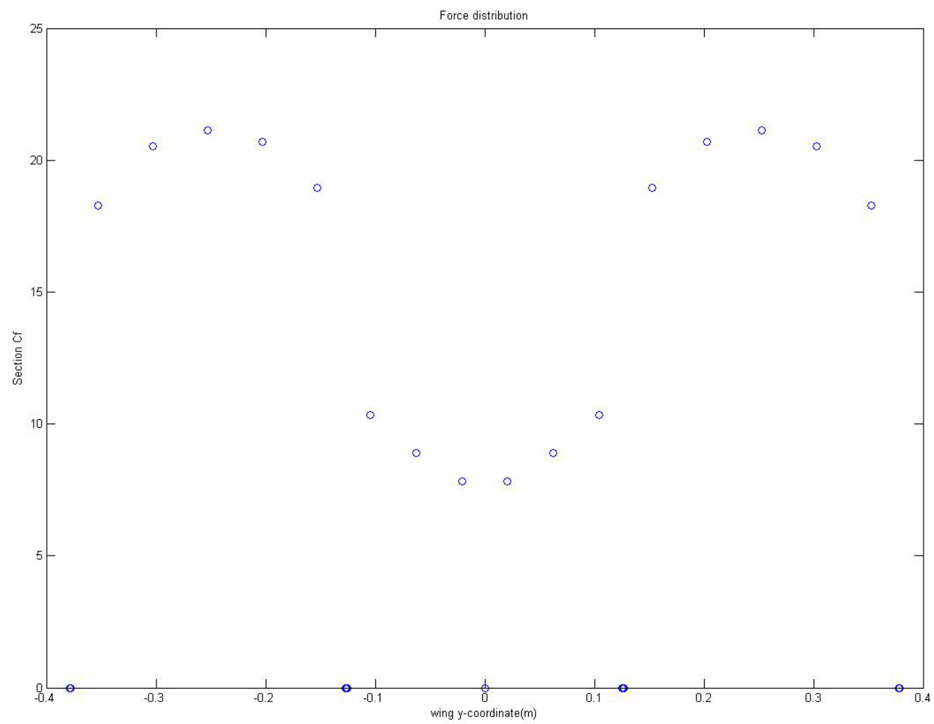

Figure 2-8: Trimmed lift distribution for the high-speed configuration at 6 m/s and CG at 26 cm

Note that in the figures each configuration has a significant low point over the part of the span that corresponds to the fuselage, this is due to the large amount of nose up elevator required to trim. The amount of elevator required is because the CG location chosen is somewhat forward to increase static stability. As noted below in the longitudinal dynamics analysis section, the stability is still somewhat marginal in the low-speed and gull-wing configurations, but moving the CG any further forward would require an unacceptably large amount of elevator to trim successfully. This nose down pitching tendency is typical of swept flying wing configurations and can often be countered by adding wing twist (washout) to lower the lift generated by the outboard (and thus further aft) wing sections. The construction technique used for this project does not lend itself to including wing twist with much accuracy, so that option was not seriously explored here. If the pitch characteristics prove to be deficient during flight testing a form of washout could be added by biasing the control surfaces on the outboard wing sections trailing edge up slightly.

Glide Models

The final step in the design of the basic aerodynamic configuration was construction and flight of unpowered models to test the basic stability aspects of the design, and as a final reasonableness check of the VLM results. A separate prototype was constructed for the high-speed, low-speed, and gull-wing configurations as seen above in Figure 2-4. The models were thrown with various speeds and initial pitch and sideslip angles to get a rough idea of the bare airframe characteristics. The CG location was also adjusted using small weights until sufficient longitudinal characteristics were achieved to prevent either stall or immediate nosedive. The CG location that gave the best results was found to be 260 mm from the nose of the aircraft, and was used as the baseline location for the rest of the project.

Control Surface Sizing and Control Mixing

The control surfaces were sized based on prior experience in the VSTL, which has shown that having excess control authority is almost never a problem, while having too little is very often a problem. To this end, the entire trailing edge of the wings with the exception of the tip extensions is moveable. Five control surfaces make up the moveable trailing edge as shown in Figure 2-9: 1 outboard aileron on each outboard wing section, 1 inboard aileron on each inboard wing section, and an elevator located on the fuselage plate section.

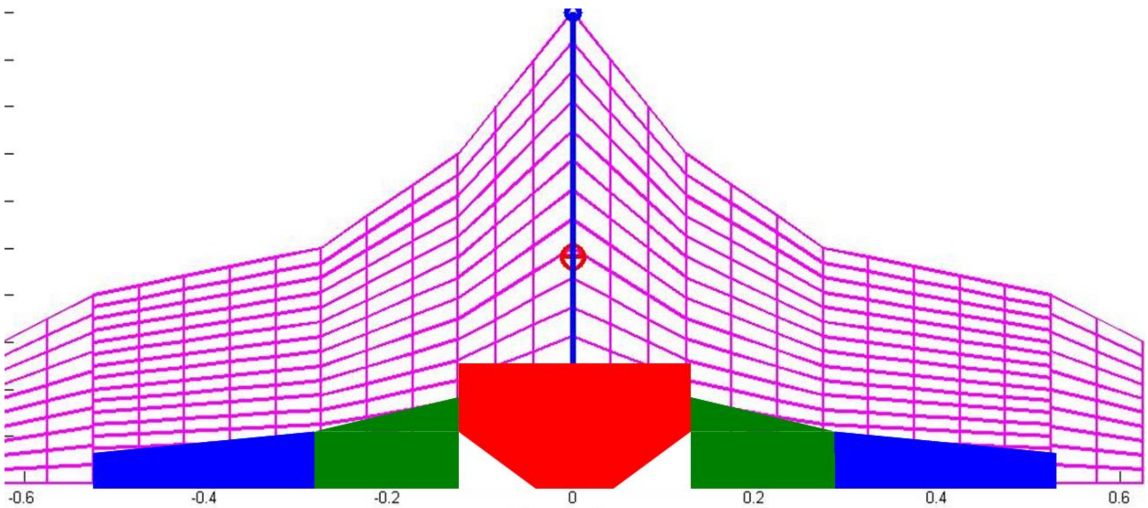

Figure 2-9: Approximate control surface locations. Red is elevator, green is inboard aileron, and blue is outboard aileron. Low-speed configuration shown

Each control surface was designed to be the full span of each section, with small cutouts to allow for full control authority with the wings in the folded positions. The aileron chords are set to 25% of the wing chord, and the elevator chord is 20 % of the wing chord.

The control surface mixing for the elevator is straightforward and does not change as the morph angle μ is varied. Trailing edge down is positive and results in a nose down pitching moment.

The mixing for the lateral directional axes is not as simple. We will define two virtual control inputs, wheel and pedal denoted as δ_w and δ_p respectively. The outboard aileron surfaces are always in the horizontal plane and act as conventional ailerons when a wheel command is issued. Positive wheel input is defined as a command to roll to the left, so the left outboard aileron will move trailing edge up proportionally to the wheel command and the right outboard aileron will move trailing edge down proportional to the wheel command. This action will be unchanged over the range of the values of μ.

Directional control is trickier because there is no conventional vertical tail or rudder surface in the low-speed configuration. In the high-speed configuration, the inboard wing sections are in the vertical plane, and therefore the inboard ailerons act as conventional rudder surfaces. A positive pedal command results in the nose yawing to the right, so with positive pedal input the left inboard aileron moves trailing edge up, which corresponds to trailing edge right in the high-speed configuration, and the right inboard aileron moves trailing down, which corresponds to trailing edge right. In the gull-wing and high-speed configurations, the inboard ailerons do not directly act like rudder controls. It would be desirable for the effects of the virtual pedal command to have only a limited change as the morphing configuration is varied. It is clear from examining the different configurations, that it is impossible to have as much side force or yawing moment authority in the low-speed configuration as compared to the other configurations. A realistic design goal then, is to define a control mixer that ensures the side force, yawing moment, and rolling moment imparted by pedal commands have the same sign across all configurations. Figure 2-10 shows a block diagram of this arrangement.

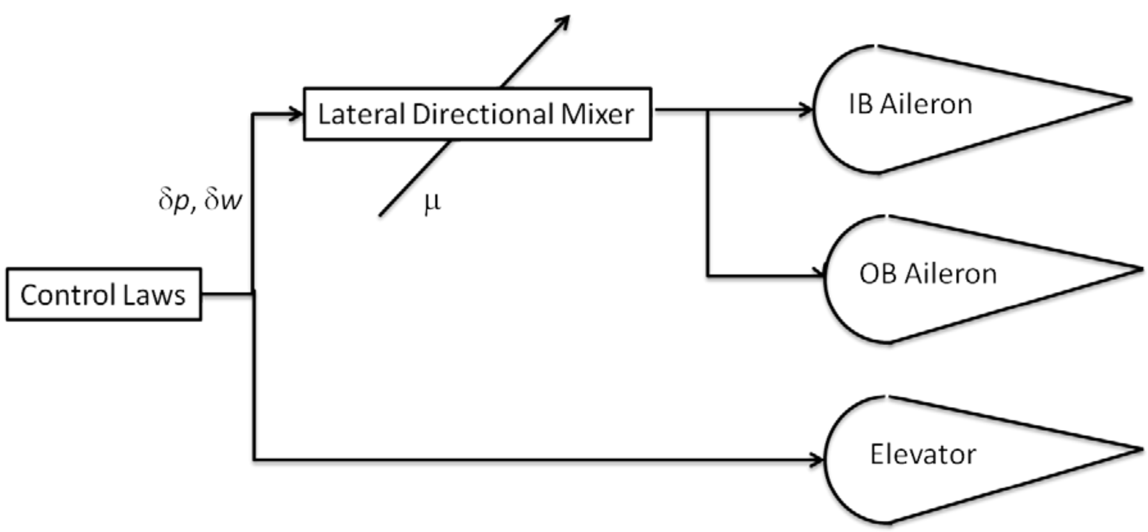

Figure 2-10: Diagram of control mixing scheme

Most flying wing configurations use "split" ailerons that create drag on one side of the vehicle to create a yawing moment for directional control. That arrangement would be too heavy and too complex for this application. Instead all of the other available control surfaces were used to get as close to the high speed configurations pedal response characteristics as possible in the low-speed and gull-wing configurations. To do this, a simple optimization routine was used to find mixing ratios between the control surfaces that result in 1) pedal input having a response that is the same sign as the responses in the high-speed configuration and 2) has magnitudes that are as close as possible to the high-speed configuration within reason.

The three control derivatives of interest are the side force due to pedal, $C_{Y\delta p}$, the rolling moment due to pedal, $C_{L\delta p}$, and the yawing moment due to pedal $C_{N\delta p}$. The vortex lattice code can give the side force, rolling moment and yawing moment coefficients of each of the aileron surfaces in each configuration. This data is shown in Table 2-3.

Table 2-3: Variation of side force, rolling moment, and yawing moment coefficients of each flap with morphing configuration

	Inboard*	Outboard*
	CY/CL/CN	CY/CL/CN
High-Speed	-0.15/0.02/-0.01	-0.01/0.07/0.008
Gull-Wing	-0.09/0.04/-0.01	-0.005/0.1/0.007
Low-Speed	0.004/0.04/0.003	0.007/0.1/0.006

* Right wing values shown, left wing values are equal magnitude and opposite sign. Positive surface deflection is trailing edge down

It can be seen that there are sign changes when going from the low-speed configuration to the gull-wing and high-speed configurations. The roll derivatives all stay the same as expected, but both the inboard and outboard ailerons' side-force coefficients switch signs and the yawing moment coefficient for the inboard ailerons also switches signs. In the low-speed configuration, the side force generated by the inboard and outboard ailerons is very small as expected for a configuration with a small amount of sweep. The sign change there makes sense because as the inboard wings fold upwards, their lift vector tilts to point along the y-axis, and thus there is an order of magnitude change in the side force generated as the wings are drawn up. The yawing moment is a little more troubling and has some relation to vortex lattice limitation number 2 noted above. In the low-speed configuration, the only yawing moment created by an individual aileron is due to the side force it generates and by any drag increase it produces as it is deflected. As is stated in VLM limitation number 2, the drag predictions of the vortex lattice method tend to be somewhat inaccurate because it does not calculate form drag. The only drag captured by this method is the change in induced drag due to the change in lift created by deflecting the surface, which as is shown above, is so small that it gets overcome by the moment created by the side force generated by the control surface.

This shortcoming could lead to a mixing solution that is correct for the aerodynamic data given here and that used in the simulation, but that could result in bad behavior when actually flying the vehicle. Moving forward it is assumed that the vortex lattice answer is correct, since this is the same data that will be used for the simulation studies later. It should be noted that the method used to design the mixer that follows would work just as well given a more accurate answer for the yaw control power in the low-speed configuration. An extension of the VLM method to allow a more accurate calculation of the profile drag change could be employed in the future to provide a more reasonable answer. Alternatively, flight data and parameter estimation techniques could be used to refine the model and thus the mixer and the control law that will be developed later.

The total derivatives for the virtual pedal inputs are given by the summation of the contributions of each surface multiplied by its mixing factor as shown in Equation 2.1.

$$
\begin{aligned}
C_{Y\delta p} &= a_{LIB}C_{YLIB} + a_{LOB}C_{YLOB} + a_{RIB}C_{YRIB} + a_{ROB}C_{YROB} \\
C_{L\delta p} &= a_{LIB}C_{LLIB} + a_{LOB}C_{LLOB} + a_{RIB}C_{LRIB} + a_{ROB}C_{LROB} \\
C_{N\delta p} &= a_{LIB}C_{NLIB} + a_{LOB}C_{NLOB} + a_{RIB}C_{NRIB} + a_{ROB}C_{NROB}
\end{aligned}
\tag{2.1}
$$

In Equation 2.1, a_{LIB}, a_{LOB}, a_{RIB}, and a_{ROB} are constant mixer coefficients that define the total contribution of each aileron to a unit input of the virtual pedal. For the case of the high-speed configuration, in which the inboard ailerons simply function as conventional rudders in response to pedal commands, and the outboard ailerons are not involved, we see that $a_{LIB} = -1$, $a_{LOB} = 0$, $a_{RIB} = +1$, and $a_{ROB} = 0$. The maximum allowable value for each surface is set to 1. This means the mixer coefficients serve as a ratio of the deflection of each surface to the others. The mixer coefficients for the high speed configuration indicate that the left inboard aileron and the right inboard aileron act in equal amounts, but in the opposite direction from each other in response to pedal.

The goal of the optimization problem is to make the total derivatives as given in Equation 2.1 for the gull-wing, and low-speed configuration as close as possible to the values for the high-speed configuration by varying the mixer coefficients a_{LIB}, a_{LOB}, a_{RIB}, and a_{ROB}, and if possible, they should have the same sign. To solve this problem, define the cost function J as in Equation 2.2.

$$C_{X\ \delta p\ error} = C_{X\ \delta p\ HS} - C_{X\ \delta p\ design},\ C_{X\ \delta p\ sign\ error} = sign(C_{X\ \delta p\ HS}) - sign(C_{X\ \delta p\ design})$$
$$J = C_{Y\ \delta p\ error}{}^{2} + C_{L\ \delta p\ error}{}^{2} + C_{N\ \delta p\ error}{}^{2} + 10C_{Y\ \delta p\ sign\ error}{}^{2} + 10C_{L\ \delta p\ sign\ error}{}^{2} + 10C_{N\ \delta p\ sign\ error}{}^{2} \tag{2.2}$$

Where $C_{X\ dp\ design}$ is either the total low-speed or gull-wing coefficients. This cost function penalizes the error from the high-speed total derivative value and a sign change from the high-speed derivative value. The sign change penalties are weighted higher because getting the sign correct is more important than matching the values exactly. In addition to the errors and sign changes, we would like to make sure that the outboard ailerons do not get weighted more by more than 0.5 to ensure that there is sufficient travel left to perform roll maneuvers.

The MATLAB function *fmincon* was used to minimize J over the possible values of the mixer coefficients, with the constraints that a_{LIB}, a_{RIB} are between +/- 1 and that a_{LOB} and a_{ROB} are between +/- 0.5. The resulting coefficients are shown in Figure 2-11.

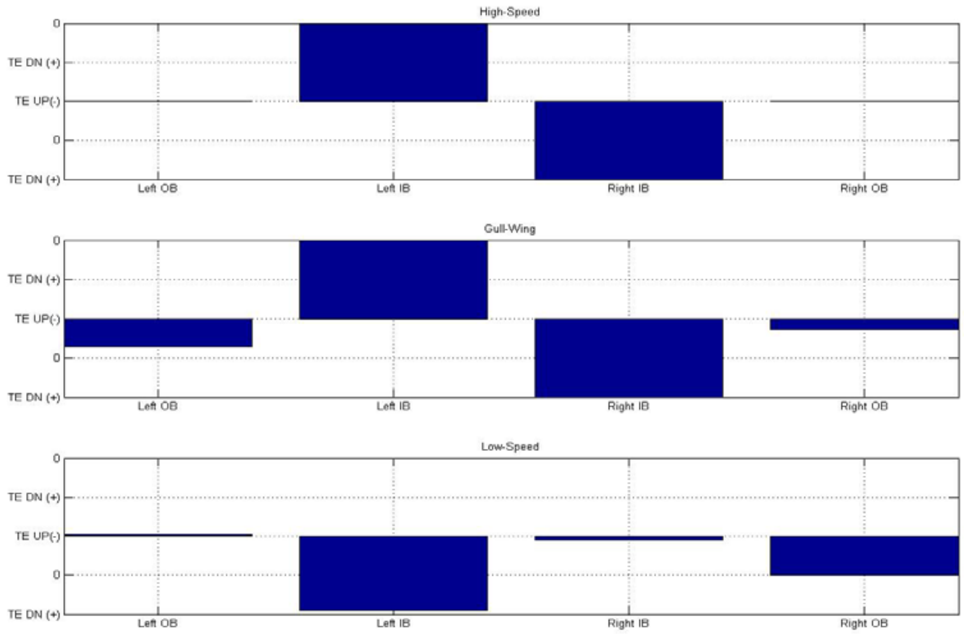

Figure 2-11: Optimal pedal mixer coefficients represented graphically for the high-speed, gull-wing, and low-speed configurations

The resulting total control derivatives are plotted as a function of morph angle in Figure 2-12.

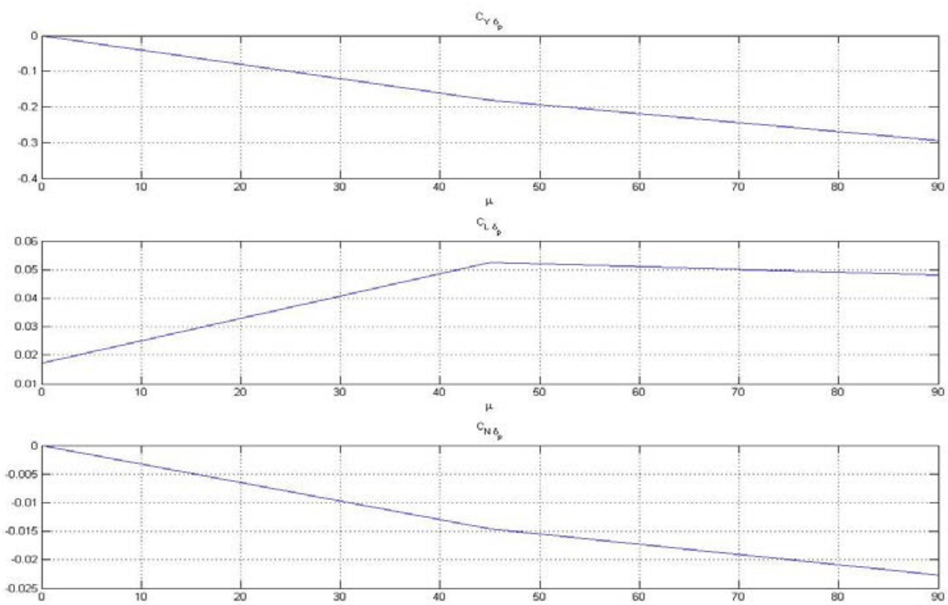

Figure 2-12: Optimal total pedal control derivatives as a function of morph angle

While the information shown in Figure 2-11 and Figure 2-12 represents the theoretically optimal solution to the problem, it would be convenient if the mixer coefficients were nice round numbers. Figure 2-11 shows that in the gull wing configuration the main driving surfaces are the inboard ailerons operating in the same manner as they do in the high-speed configuration. If the mixer could stay constant between the two configurations with acceptable results, this would be a great simplification. Note also that in the low-speed configuration the left outboard and right inboard ailerons only provide a small contribution. If these are zero, the low-speed mixer configuration is simpler as well. Implementing those two changes results in the mixer coefficients and total control derivatives shown in Figure 2-13 and Figure 2-14.

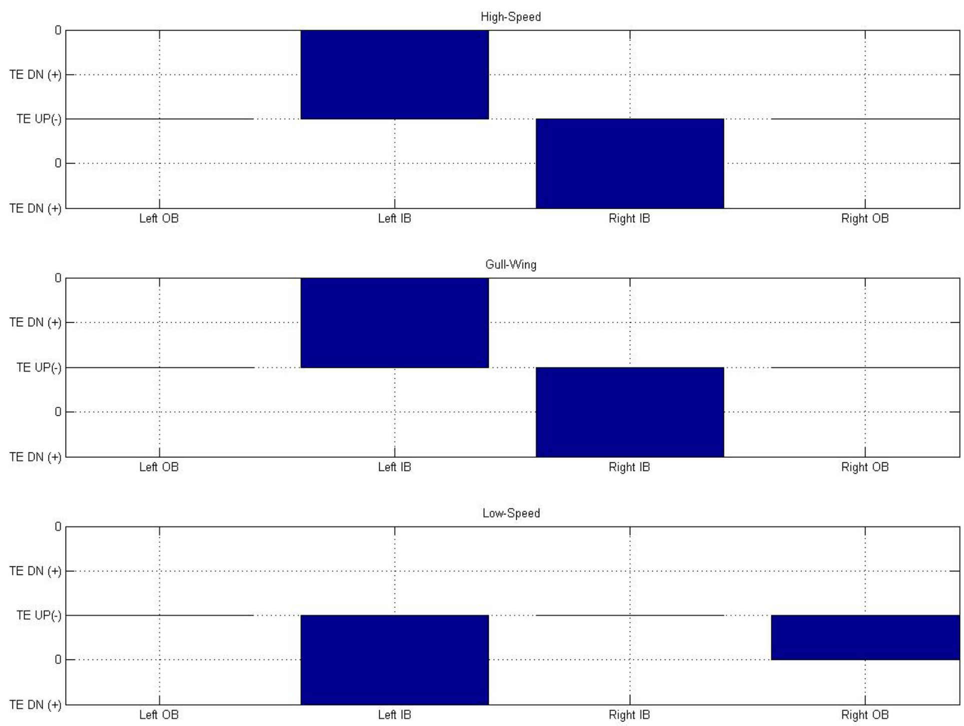

Figure 2-13: Chosen pedal mixer coefficients represented graphically for the high-speed, gull-wing, and low-speed configurations

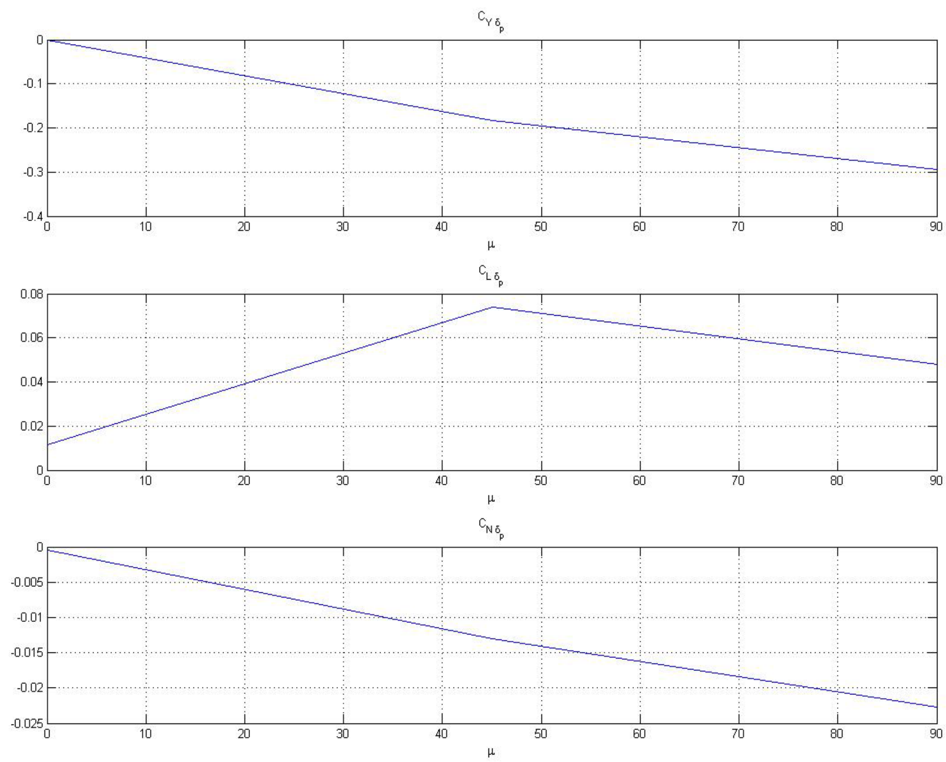

Figure 2-14: Chosen total pedal control derivatives as a function of morph angle

It is clear that these simplifications will make life easier while still ensuring that the total control derivatives remain relatively unchanged from the "optimal" solution shown above.

The last step was choosing how to transition between the different sets of mixing coefficients. It was decided to go with the simplest method which is to just change the coefficients linearly as a function of morph angle. This may lead to off-design configurations between the low-speed and gull-wing configuration where the total control derivatives become negative. Because the intent of the vehicle is to stay at intermediate configurations only momentarily, however, this possibility is ignored. For a more practical application of this vehicle, the signs would need to be determined for a larger number of intermediate configurations to account for the case where the morphing mechanism fails and the vehicle gets stuck off-design but needs to continue to be controllable.

More advanced techniques for determining the optimal mixing scheme are available. Both methods for determining the mixing *a priori* and in some instances attempting to optimize the mixing online during flight as conditions vary or control surfaces or systems become disabled by system malfunctions or damage have been explored, see for example [20] and [21]. The aircraft configuration developed here would be an excellent platform for research in these areas in the future, both for traditional vehicles, and for vehicles which change configuration (and thus control derivatives) significantly.

Bare Airframe Dynamics

The vortex lattice code was used to generate linearized state space representations of the bare airframe vehicle dynamics with the control mixer included about an equilibrium point. Small perturbations of the state variables and control inputs from the trimmed state are used to calculate the **A** and **B** matrices of a state space system in the form of Equation 2.3.

$$\dot{x} = Ax + Bu \tag{2.3}$$

Here, x is the state vector of the linearized system and u is the input vector. The results of this linearization can then be used to perform the normal range of linear system analysis techniques. Of particular interest will be the change in the modal characteristics of the airframe as the morph angle is varied.

Longitudinal Dynamics

Figure 2-15 shows the longitudinal axis sign conventions used.

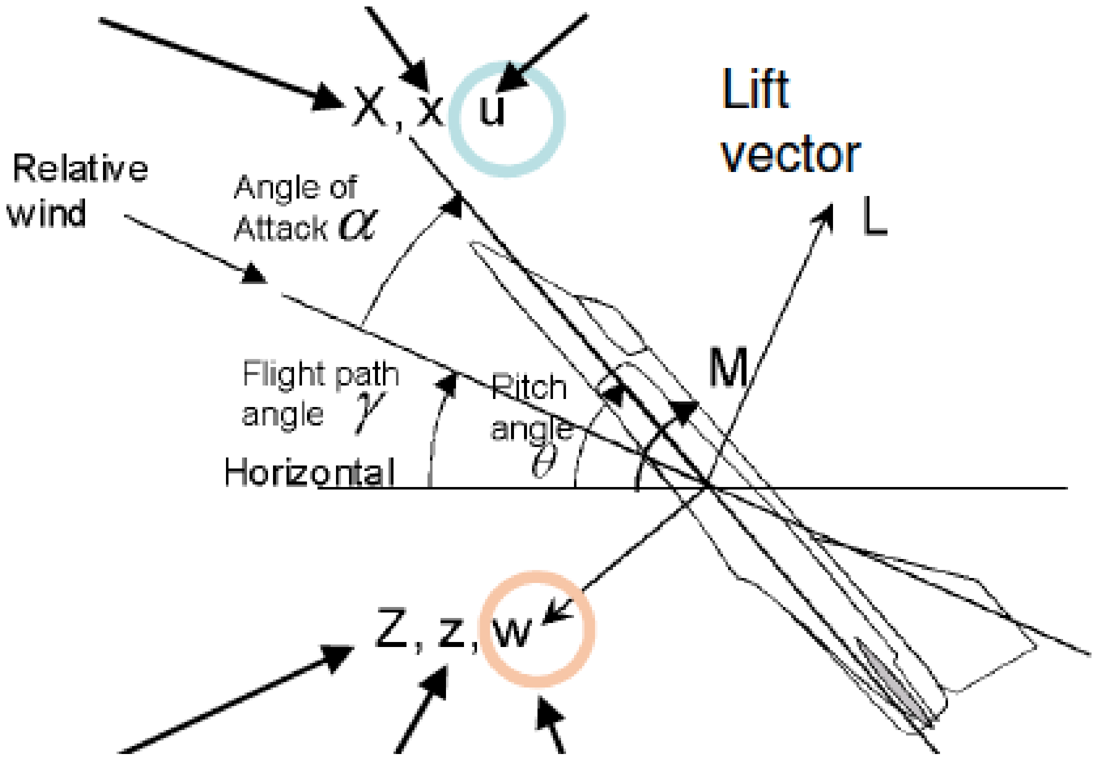

Figure 2-15: Longitudinal Axis Sign Conventions

The equations of motion for the longitudinal dynamics in the form of Equation 2.3 are shown in Equations 2.4 through 2.6 for the low-speed, gull-wing, and high speed configurations respectively.

$$\begin{bmatrix} \dot{V} \\ \dot{\alpha} \\ \dot{Q} \\ \dot{\theta} \end{bmatrix} = \begin{bmatrix} -1.1 & 5.5 & -0.2 & -9.8 \\ -0.5 & -13.8 & 0.6 & 0 \\ 0 & -19.6 & -1.7 & 0 \\ 0 & 0 & 1 & 0 \end{bmatrix} \begin{bmatrix} V \\ \alpha \\ Q \\ \theta \end{bmatrix} + \begin{bmatrix} 8.3 & 0.5 \\ -0.3 & -2.2 \\ 0 & -8.5 \\ 0 & 0 \end{bmatrix} \begin{bmatrix} T \\ \delta_e \end{bmatrix} \tag{2.4}$$

$$\begin{bmatrix} \dot{V} \\ \dot{\alpha} \\ \dot{Q} \\ \dot{\theta} \end{bmatrix} = \begin{bmatrix} -1.0 & 5.9 & -0.1 & -9.8 \\ -0.5 & -11.5 & 0.7 & 0 \\ 0 & -25.14 & -1.5 & 0 \\ 0 & 0 & 1 & 0 \end{bmatrix} \begin{bmatrix} V \\ \alpha \\ Q \\ \theta \end{bmatrix} + \begin{bmatrix} 8.3 & -0.4 \\ -0.3 & -2.3 \\ 0 & -9.2 \\ 0 & 0 \end{bmatrix} \begin{bmatrix} T \\ \delta_e \end{bmatrix} \tag{2.5}$$

$$\begin{bmatrix} \dot{V} \\ \dot{\alpha} \\ \dot{Q} \\ \dot{\theta} \end{bmatrix} = \begin{bmatrix} -1.0 & 6.1 & 0 & -9.8 \\ -0.5 & -6.9 & 0.8 & 0 \\ 0 & -21.4 & -1.1 & 0 \\ 0 & 0 & 1 & 0 \end{bmatrix} \begin{bmatrix} V \\ \alpha \\ Q \\ \theta \end{bmatrix} + \begin{bmatrix} 8.0 & -1.1 \\ -0.4 & -1.9 \\ 0 & -8.1 \\ 0 & 0 \end{bmatrix} \begin{bmatrix} T \\ \delta_e \end{bmatrix} \tag{2.6}$$

The state space equations in 2.4 through 2.6 have elements that are the dimensional stability derivatives. To allow more meaningful comparisons, these derivatives are placed in non-dimensional form by using the standard scaling factors [10]. It can then be placed into a convenient form that directly shows the controllability and observability of the systems' modes through a similarity transformation [19]. This is performed using the MATLAB function *canon* with the type set to '*modal'*. The result is a transformed system with each eigenvalue in block diagonal form in the **A** matrix and an indication of the controllability of each mode in the **B** matrix. Then by direct inspection, the controllability and observability of each mode can be ascertained. Let us first examine the controllability by looking at the state equations for each configuration. Equations 2.7, 2.8, and 2.9 show the low-speed, gull-wing, and high-speed configurations in non-dimensional modal coordinates. Note that the thrust input derivatives have been omitted because their non-dimensional form is of little utility and they have only a small influence on the dynamics [10].

$$\begin{bmatrix} \dot{z}_1 \\ \dot{z}_2 \\ \dot{z}_3 \\ \dot{z}_4 \end{bmatrix} = \begin{bmatrix} -0.7 & 0.6 & 0 & 0 \\ -0.6 & -0.7 & 0 & 0 \\ 0 & 0 & 0.3 & 0.6 \\ 0 & 0 & -0.6 & 0.3 \end{bmatrix} \begin{bmatrix} z_1 \\ z_2 \\ z_3 \\ z_4 \end{bmatrix} + \begin{bmatrix} 0.5 \\ -0.5 \\ 0.6 \\ -0.1 \end{bmatrix} [\delta_e] \tag{2.7}$$

$$\begin{bmatrix} \dot{z}_1 \\ \dot{z}_2 \\ \dot{z}_3 \\ \dot{z}_4 \end{bmatrix} = \begin{bmatrix} -0.7 & 0.7 & 0 & 0 \\ 0.7 & -0.7 & 0 & 0 \\ 0 & 0 & 0.3 & 0.6 \\ 0 & 0 & -0.6 & 0.3 \end{bmatrix} \begin{bmatrix} z_1 \\ z_2 \\ z_3 \\ z_4 \end{bmatrix} + \begin{bmatrix} 0.7 \\ 0.6 \\ -0.6 \\ 0.2 \end{bmatrix} [\delta_e] \tag{2.8}$$

$$\begin{bmatrix} \dot{z}_1 \\ \dot{z}_2 \\ \dot{z}_3 \\ \dot{z}_4 \end{bmatrix} = \begin{bmatrix} -0.6 & 0.6 & 0 & 0 \\ -0.6 & -0.6 & 0 & 0 \\ 0 & 0 & 0.3 & 0.6 \\ 0 & 0 & -0.6 & 0.3 \end{bmatrix} \begin{bmatrix} z_1 \\ z_2 \\ z_3 \\ z_4 \end{bmatrix} + \begin{bmatrix} -0.5 \\ -0.8 \\ -0.6 \\ 0.1 \end{bmatrix} [\delta_e] \tag{2.9}$$

It is clear from this representation, that the controllability of all of the modes from the elevator is relatively constant over the range of morph angles. Next let us examine the observability of each mode by looking at the transformed version of the **C** matrix for each configuration. Assuming all states are available for feedback, the original C matrices are simply $\mathbf{I}^{nxn}$. Equations 2.10, 2.11, and 2.12 show the transformed C matrices of the low-speed, gull-wing, and high-speed configurations respectively.

$$\begin{bmatrix} w_1 \\ w_2 \\ w_3 \\ w_4 \end{bmatrix} = \begin{bmatrix} 1.1 & 0.7 & -0.4 & -1.7 \\ 0.05 & 0.3 & 0.1 & 0.2 \\ -0.05 & 0.08 & -0.09 & -0.004 \\ 0.1 & -0.03 & -0.07 & 0.1 \end{bmatrix} \begin{bmatrix} z_1 \\ z_2 \\ z_3 \\ z_4 \end{bmatrix} \tag{2.10}$$

$$\begin{bmatrix} w_1 \\ w_2 \\ w_3 \\ w_4 \end{bmatrix} = \begin{bmatrix} -0.6 & 0.8 & 0.4 & 1.5 \\ -0.2 & 0.05 & -0.1 & -0.2 \\ -0.06 & -0.04 & 0.09 & 0.006 \\ 0.02 & 0.08 & 0.07 & -0.1 \end{bmatrix} \begin{bmatrix} z_1 \\ z_2 \\ z_3 \\ z_4 \end{bmatrix} \tag{2.11}$$

$$\begin{bmatrix} w_1 \\ w_2 \\ w_3 \\ w_4 \end{bmatrix} = \begin{bmatrix} 1.0 & -0.5 & 0.3 & 1.5 \\ 0.2 & 0.001 & -0.7 & -0.2 \\ 0.05 & 0.05 & 0.09 & 0.02 \\ 0.009 & -0.08 & 0.08 & -0.1 \end{bmatrix} \begin{bmatrix} z_1 \\ z_2 \\ z_3 \\ z_4 \end{bmatrix} \tag{2.12}$$

From the preceding equations it can be seen that in each case the modes are observable, and the degree of observability changes little from configuration to configuration.

For control design, it is common to isolate the short period approximation of the model. The short period approximation removes the speed, altitude, and theta states from the equations of motion and focuses on the angle of attack (α) and pitch rate (Q) state equations. The sole input is elevator deflection (δ_e).

Equation 2.13 shows the linearized state equations for the longitudinal axis at a trim airspeed of 6 m/s in the low-speed configuration (morph angle = 0°).

$$\begin{bmatrix} \dot{\alpha} \\ \dot{Q} \end{bmatrix} = \begin{bmatrix} -13.8 & 0.6 \\ -19.6 & -1.7 \end{bmatrix} \begin{bmatrix} \alpha \\ Q \end{bmatrix} + \begin{bmatrix} -2.2 \\ -8.5 \end{bmatrix} \delta_e \tag{2.13}$$

Equation 2.14 shows the same equations for the gull-wing configuration (morph angle = 45°).

$$\begin{bmatrix} \dot{\alpha} \\ \dot{Q} \end{bmatrix} = \begin{bmatrix} -11.5 & 0.7 \\ -25.1 & -1.5 \end{bmatrix} \begin{bmatrix} \alpha \\ Q \end{bmatrix} + \begin{bmatrix} -2.3 \\ -9.2 \end{bmatrix} \delta_e \tag{2.14}$$

Finally, Equation 2.15 shows the longitudinal state equations for the high-speed configuration (morph angle = 90°).

$$\begin{bmatrix} \dot{\alpha} \\ \dot{Q} \end{bmatrix} = \begin{bmatrix} -6.9 & 0.8 \\ -21.4 & -1.1 \end{bmatrix} \begin{bmatrix} \alpha \\ Q \end{bmatrix} + \begin{bmatrix} -1.9 \\ -8.1 \end{bmatrix} \delta_e \tag{2.15}$$

Equations 2.13 through 2.15 clearly show that the morph angle does not have a strong effect on the longitudinal dynamics. This is as expected because the majority of the geometry features that affect the pitch axis are not changed significantly as the wings are folded.

Figure 2-16 shows a bar graph of the variation of each element of the short period approximation **A** and **B** matrices for the low-speed, gull-wing, and high-speed configurations as a percentage of the value of each element in the low speed configuration.

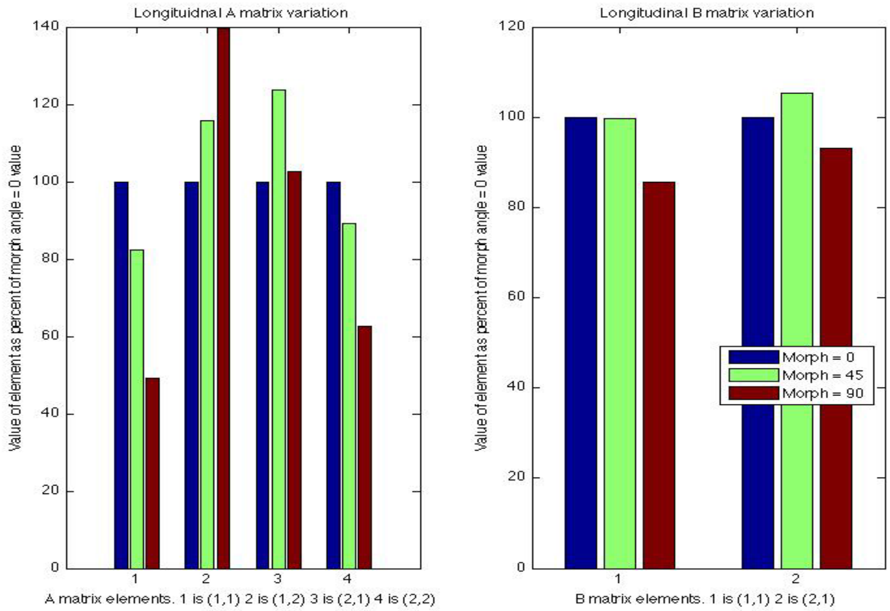

Figure 2-16: Variation in longitudinal **A** and **B** matrices at 6m/s. Each bar represents the value of one matrix element as a percentage of the same element in the low speed configuration

The largest change is in the $\mathbf{A_{11}}$ element. This element corresponds to the dimensional stability derivative Z_α, which is related to the lift curve slope of the overall airframe. The dimensional change in lift from a change in angle of attack will be quite different between the configurations because of the reduction in the projected wing area as the wings are folded. The $\mathbf{A_{11}}$ element has a strong influence on the short period damping ratio. As it is lowered we would also expect a decrease in the short period damping. This is confirmed by inspection of the longitudinal root locus in Figure 2-17. The short period initially has a damping ratio of 1 at 0 morph angle, but eventually moves towards a ratio of 0.8 as the morph angle is increased.

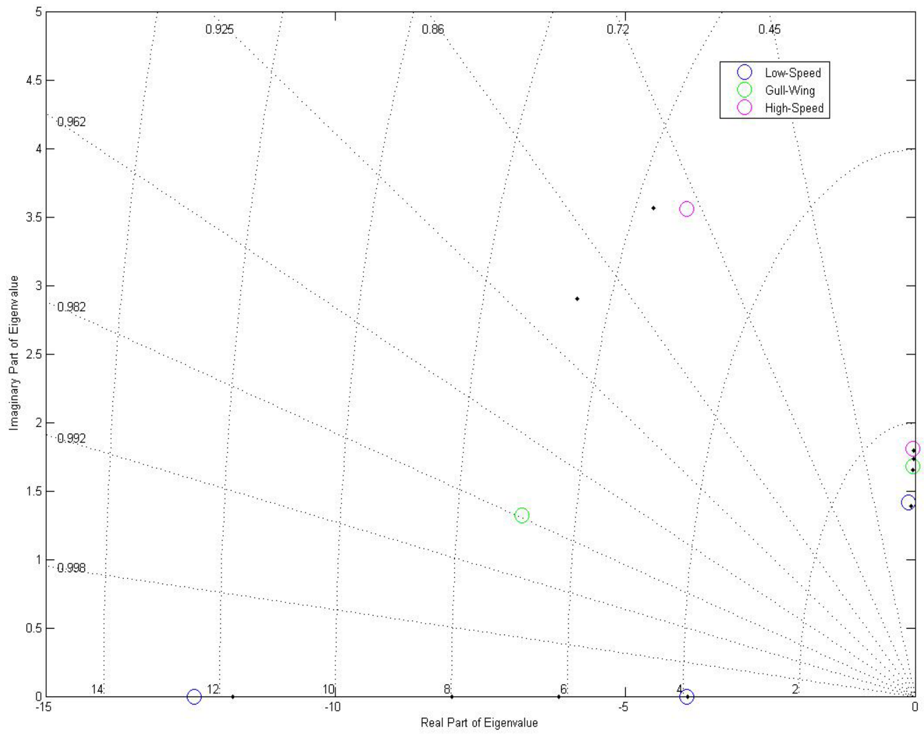

Figure 2-17: Root locus of longitudinal modes as the morph angle is swept from 0 to 90 degrees at a trim airspeed of 6 m/s. Open circles represent the three design configurations, small dots represent intermediate configurations

Figure 2-17 indicates that in the low-speed configuration, the short period poles lie on the real axis. This is an indication of an airplane that is marginally statically stable. A small movement of the center of gravity (CG) location aft could force one of the short period poles to the right half plane and cause instability. A root locus of the longitudinal eigenvalues as the CG is varied is shown in Figure 2-18. As is shown, a very slight change in the CG can cause the short period to go unstable.

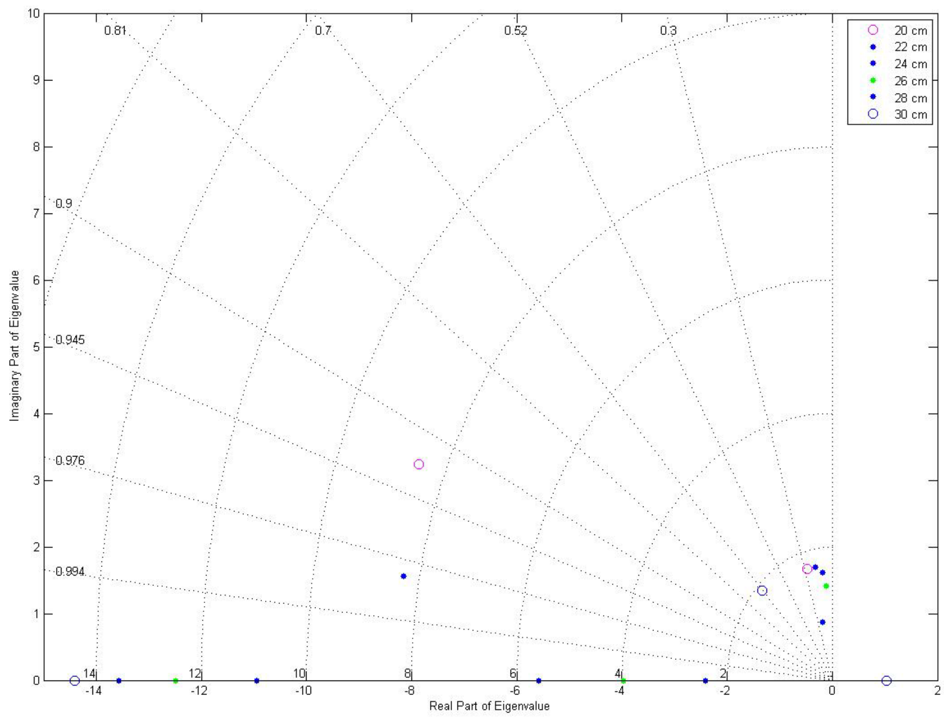

Figure 2-18: Root locus of low-speed configuration as CG is varied

Often, in order to stabilize an aircraft with this kind of reduced static stability, angle of attack feedback must be used, see for example [10]. This can be used to drive the pitching moment versus α curve to be negative, ensuring static stability. If possible, however, it is a good idea to avoid angle of attack feedback as the sensors used to measure it are often noisy. For this reason, two sets of control gains will be determined for the inner loop: one with α feedback and one without.

Figure 2-17 also shows that the phugoid mode is marginally stable at almost all values of μ. This is a normal situation for many aircraft and is easily overcome through the use of an autopilot that controls to a fixed altitude combined with an auto throttle to maintain airspeed, as will be used here.

Lateral Directional Dynamics

The lateral directional characteristics of the vehicle are examined by isolating the state equations for sideslip angle (β), roll rate (P), and yaw rate (R). Lateral directional inputs include aileron deflection (δ_a) and rudder deflection (δ_r). Figure 2-19 shows the sign conventions used.

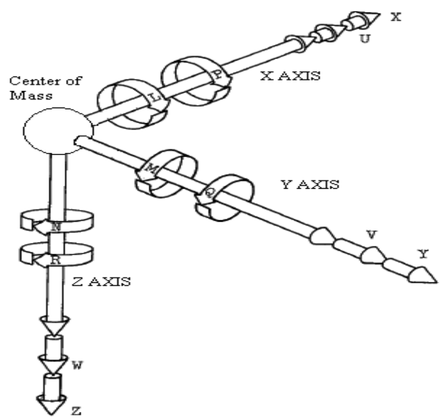

Figure 2-19: Lateral Directional Axis Sign Conventions. Positive x-axis is out the nose of the airplane, and positive y-axis is along the right wing

Equation 2.16 shows the linearized state equations for the lateral directional axes at a trim airspeed of 6 m/s in the low-speed configuration as given by the vortex lattice method.

$$\underbrace{\begin{bmatrix} \dot{\beta} \\ \dot{P} \\ \dot{R} \end{bmatrix}}_{\dot{x}_p^{latd}} = \underbrace{\begin{bmatrix} -0.16 & 0.22 & -0.97 \\ -337.0 & -356.82 & 76.51 \\ 9.16 & -6.92 & -2.99 \end{bmatrix}}_{A_p^{latd}} \underbrace{\begin{bmatrix} \beta \\ P \\ R \end{bmatrix}}_{x_p^{latd}} + \underbrace{\begin{bmatrix} 0.05 & -0.003 \\ -1926.90 & 109.45 \\ -7.98 & 0.29 \end{bmatrix}}_{B_p^{latd}} \underbrace{\begin{bmatrix} \delta_a \\ \delta_r \end{bmatrix}}_{u^{latd}} \tag{2.16}$$

Apparent in Equation 2.16 is how small the term corresponding to the side force generated by rudder deflection is in this configuration. This is expected for a vehicle with no true rudder control surface, and low wing sweep. This implies that in the low-speed configuration, the rudder control will have minimal effectiveness at controlling sideslip angle.

Equation 2.17 shows the same equations for the gull-wing configuration.

$$\underbrace{\begin{bmatrix} \dot{\beta} \\ \dot{P} \\ \dot{R} \end{bmatrix}}_{\dot{x}_p^{latd}} = \underbrace{\begin{bmatrix} -0.96 & 0.21 & -0.95 \\ -510.26 & -213.75 & 59.37 \\ 6.11 & -5.22 & -2.67 \end{bmatrix}}_{A_p^{latd}} \underbrace{\begin{bmatrix} \beta \\ P \\ R \end{bmatrix}}_{x_p^{latd}} + \underbrace{\begin{bmatrix} -0.03 & -0.58 \\ -1549.7 & -583.5 \\ -7.70 & 7.3 \end{bmatrix}}_{B_p^{latd}} \underbrace{\begin{bmatrix} \delta_a \\ \delta_r \end{bmatrix}}_{u^{latd}} \tag{2.17}$$

Finally, Equation 2.18 shows the lateral directional state equations for the high-speed configuration.

$$\underbrace{\begin{bmatrix} \dot{\beta} \\ \dot{P} \\ \dot{R} \end{bmatrix}}_{\dot{x}_p^{latd}} = \underbrace{\begin{bmatrix} -1.58 & 0.30 & -0.90 \\ -660.40 & -64.72 & 39.57 \\ 1.03 & -2.43 & -1.78 \end{bmatrix}}_{A_p^{latd}} \underbrace{\begin{bmatrix} \beta \\ P \\ R \end{bmatrix}}_{x_p^{latd}} + \underbrace{\begin{bmatrix} -0.05 & -0.73 \\ -871.19 & -300.05 \\ -7.24 & 10.07 \end{bmatrix}}_{B_p^{latd}} \underbrace{\begin{bmatrix} \delta_a \\ \delta_r \end{bmatrix}}_{u^{latd}} \tag{2.18}$$

As we did with the longitudinal dynamics, the controllability and observability of the lateral directional modes can be compared from configuration to configuration by changing the equations in 2.16 through 2.18 into their non-dimensional modal coordinate forms as shown in Equations 2.19 through 2.21, and the corresponding observability forms in Equations 2.22 through 2.24.

$$\begin{bmatrix} \dot{z}_1 \\ \dot{z}_2 \\ \dot{z}_3 \end{bmatrix} = \begin{bmatrix} -0.03 & 0.09 & 0 \\ -0.09 & -0.03 & 0 \\ 0 & 0 & -0.3 \end{bmatrix} \begin{bmatrix} z_1 \\ z_2 \\ z_3 \end{bmatrix} + \begin{bmatrix} -0.3 & 0.1 \\ -0.2 & 0.07 \\ -0.9 & 0.3 \end{bmatrix} \begin{bmatrix} \delta_a \\ \delta_r \end{bmatrix} \tag{2.19}$$

$$\begin{bmatrix} \dot{z}_1 \\ \dot{z}_2 \\ \dot{z}_3 \end{bmatrix} = \begin{bmatrix} -0.04 & 0.1 & 0 \\ -0.1 & -0.04 & 0 \\ 0 & 0.0 & -0.2 \end{bmatrix} \begin{bmatrix} z_1 \\ z_2 \\ z_3 \end{bmatrix} + \begin{bmatrix} -0.6 & -0.4 \\ -0.1 & 0.05 \\ -0.4 & -0.3 \end{bmatrix} \begin{bmatrix} \delta_a \\ \delta_r \end{bmatrix} \tag{2.20}$$

$$\begin{bmatrix} \dot{z}_1 \\ \dot{z}_2 \\ \dot{z}_3 \end{bmatrix} = \begin{bmatrix} -0.02 & 0.1 & 0 \\ -0.1 & -0.02 & 0 \\ 0 & 0 & -0.1 \end{bmatrix} \begin{bmatrix} z_1 \\ z_2 \\ z_3 \end{bmatrix} + \begin{bmatrix} -0.2 & 0.2 \\ -0.01 & 0.1 \\ -0.2 & 0.03 \end{bmatrix} \begin{bmatrix} \delta_a \\ \delta_r \end{bmatrix} \tag{2.21}$$

$$\begin{bmatrix} w_1 \\ w_2 \\ w_3 \end{bmatrix} = \begin{bmatrix} 0.3 & -0.5 & 0.03 \\ -0.04 & 0.04 & 0.2 \\ -0.1 & -0.09 & 0.07 \end{bmatrix} \begin{bmatrix} z_1 \\ z_2 \\ z_3 \end{bmatrix} \tag{2.22}$$

$$\begin{bmatrix} w_1 \\ w_2 \\ w_3 \end{bmatrix} = \begin{bmatrix} 0.08 & 0.4 & 0.04 \\ 0.2 & -0.1 & 0.03 \\ 0.08 & -0.02 & -0.1 \end{bmatrix} \begin{bmatrix} z_1 \\ z_2 \\ z_3 \end{bmatrix} \tag{2.23}$$

$$\begin{bmatrix} w_1 \\ w_2 \\ w_3 \end{bmatrix} = \begin{bmatrix} -0.09 & -0.4 & 0.04 \\ 0.2 & 0.03 & 0.1 \\ -0.01 & 0.08 & 0.05 \end{bmatrix} \begin{bmatrix} z_1 \\ z_2 \\ z_3 \end{bmatrix} \tag{2.24}$$

It is clear from the above that both the roll mode and the Dutch roll mode are controllable in each configuration. It can also be seen that the term in the **B** matrices corresponding to the aileron control of the roll mode gets progressively smaller as the morph angle is increased; this is because the surfaces have less effectiveness to impart roll moment as they are drawn in closer to the centerline of the vehicle. It also shows that as the morph angle is increased, the rudder becomes more and more effective at controlling the Dutch roll mode relative to the ailerons.

Figure 2-20 shows the variation in each parameter of the **A** and **B** matrices above as a function of morph angle μ. The figure shows that simple linear transition between the set of mixing coefficients has worked reasonably well.

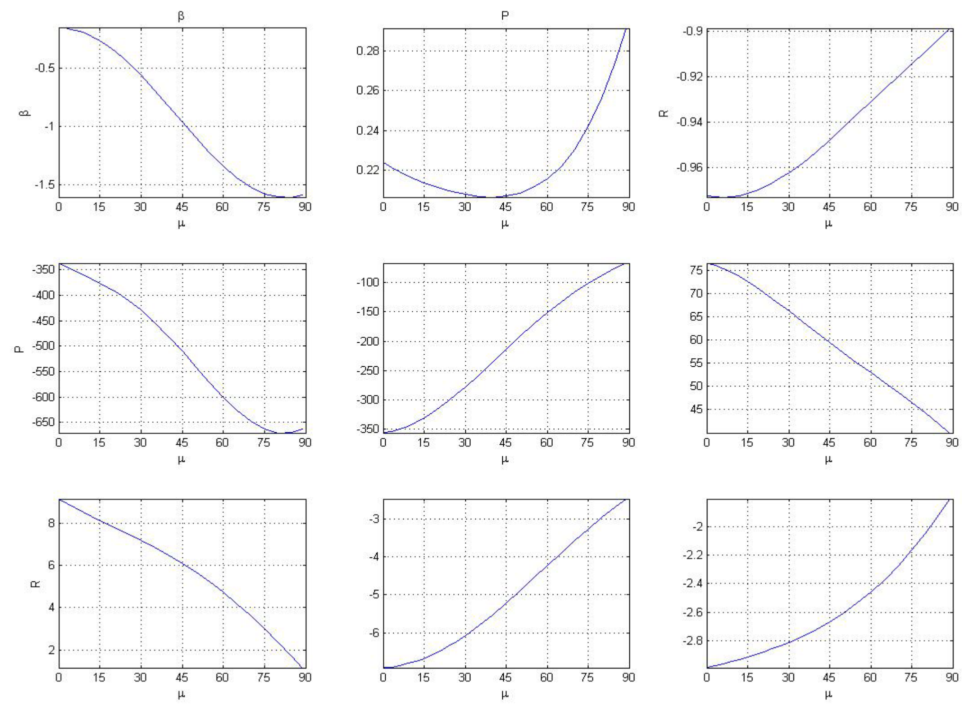

(a)

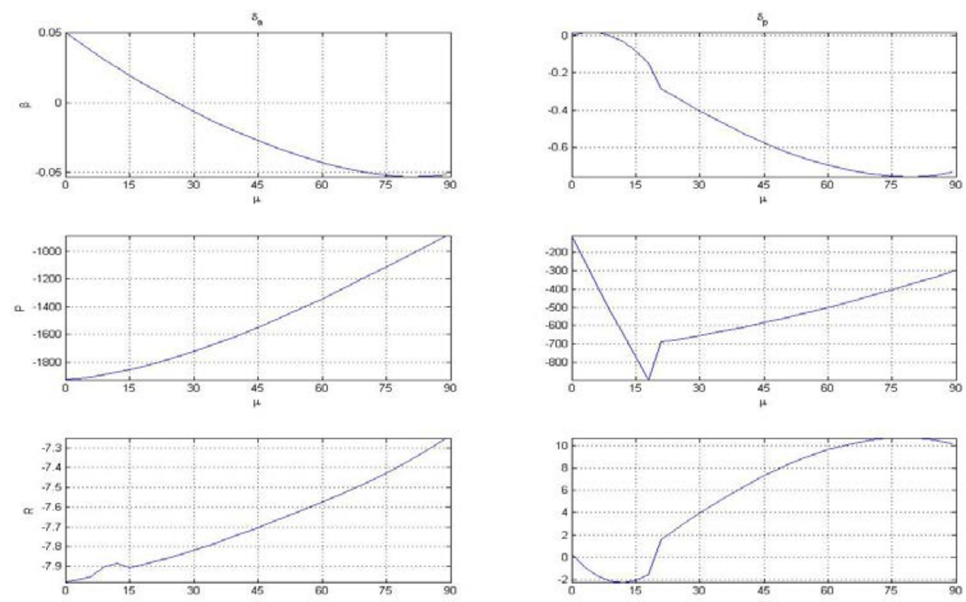

(b)

Figure 2-20: Variation of lateral-directional state-space dynamics model parameters as morph angle μ is varied (a) shows the **A** matrix elements and (b) is the **B** Matrix elements

Figure 2-21 shows the variations of each of the elements at each design configuration. The bar heights represent the value at each configuration as a percentage of the value in the low-speed configuration.

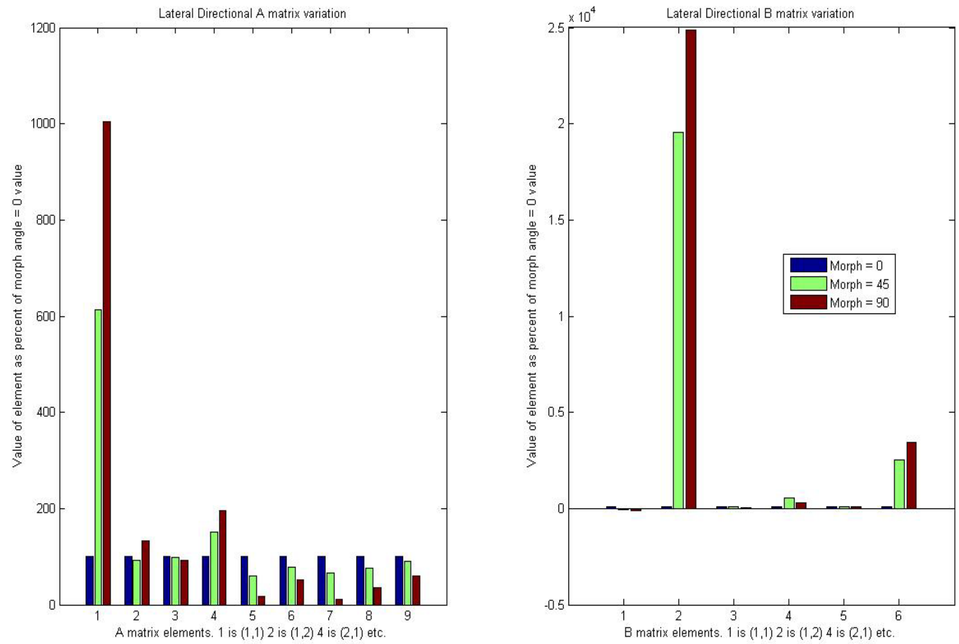

Figure 2-21: Lateral-Directional matrix variations as the morph angle is changed at 6 m/s airspeed. Bars represent the percentage of the low-speed configuration values for each configuration

The element in the **A** matrix with the largest variation is the $\mathbf{A}_{1,1}$ element, which corresponds to the dimensional derivative Y_β. This represents the change in side force due to a change in sideslip angle. This is expected considering the large increase in side area as the wings are folded into the high-speed configuration. This means that by drawing the wings of the vehicle inward, it becomes significantly more directionally stable. It is also apparent from Figure 2-21 that as the wings are folded upwards the effect of the rudder surfaces becomes much stronger as was discussed earlier. The combination of these two effects could give some insight into the why birds tend to draw their wings in when flying in gusty conditions. The added side area created by this reconfiguration, in combination with the increased control effectiveness means that a bird could both fly through a lateral disturbance more smoothly, and counteract a gust to maintain a desired trajectory more readily than in the straight winged soaring configuration. With the proper sensing and control law strategies, this type of configuration change could also be used by a man made vehicle to ride out violent gusts.

Figure 2-22 shows the root locus of the bare airframe lateral and directional modes as the morph angle is swept from 0 degrees (low-speed) to 90 degrees (high-speed) at a trim airspeed of 6 m/s.

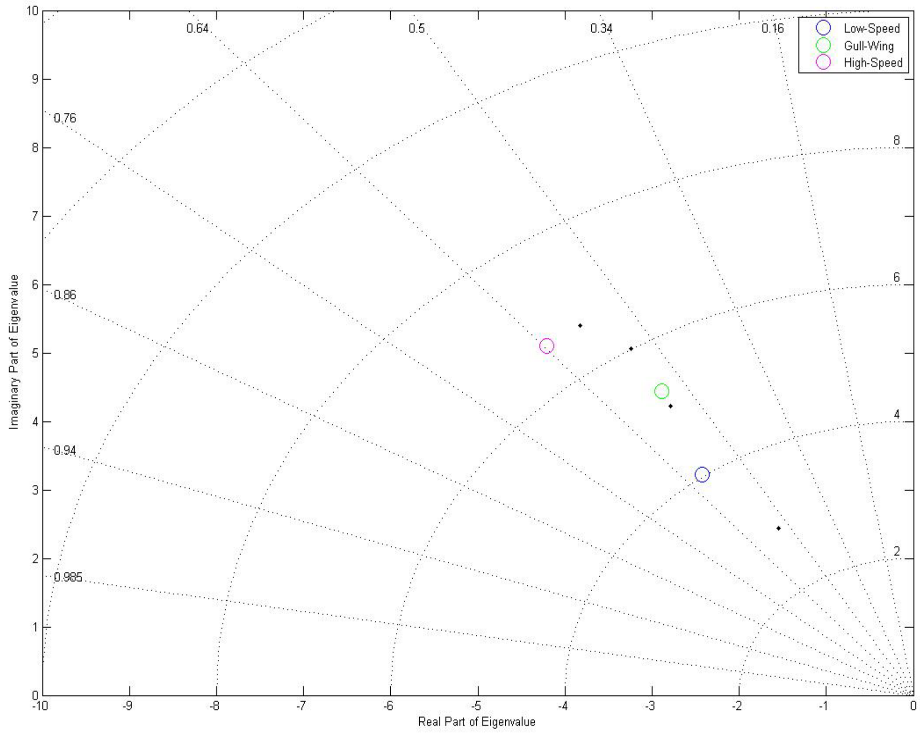

Figure 2-22: Root locus of Dutch roll mode as the morph angle is swept from 0 to 90 degrees. Airspeed is 6 m/s. Open circles represent the three design configurations, small dots represent intermediate configurations. Roll mode is far off to the left on the real axis; diagram is zoomed in on Dutch roll

As can be seen, the bare airframe shows a classic Dutch roll mode. Note that Figure 2-22 does not show the roll mode because it is far to the left and well damped so the figure is zoomed in to show detail of the more important Dutch roll mode. The locus starts at zero morph angle in the low-speed configuration with the Dutch roll poles near -2.4 ± 3.2i corresponding to a damping ratio of 0.6 and frequency of 4.0 rad/sec and proceeds towards the end of the locus where the morph angle is 90 degrees. In the high-speed configuration, the Dutch roll poles have moved to -4.0 ± 4.5i corresponding to damping ratio of 0.7 and a frequency of 6.0 rad/sec. This agrees well with the intuition from the variations shown in Figure 2-21. It is interesting to note that initially, the Dutch roll decreases in frequency as is seen by the black dot 3 rad/sec and 0.5 damping, corresponding to a morph angle of 20 degrees.

Having created a good configuration and studied the vehicle dynamics and especially how they change as the configuration is morphed, we will now move on to designing control laws to stabilize the vehicle dynamics and allow for autonomous flight in the VSTL.

Chapter 3 - Control Law Design

This chapter covers the design and analysis of the control laws to stabilize the aircraft dynamics in each configuration as well as during configuration transitions. First, the difficulties associated with control of a morphing vehicle are discussed and the approach to address these issues is given. Then, a description of the outer loop guidance command generation is given. This outer loop framework will guide design of the inner loop controllers. The outer loop controllers are based on control strategies developed for previous VSTL projects and their structure is maintained here. Next, linear controllers will be designed to stabilize the airframe dynamics and track the commands generated by the outer loops. The goal of the inner loop controllers will be to keep the response characteristics sufficiently similar over the range of possible configurations such that the outer loop controllers provide acceptable performance for all configurations. This thesis will focus on the inner loop controller designs, with background information of the outer loop controllers where appropriate. Figure 3-1 shows an overview of the controller structure.

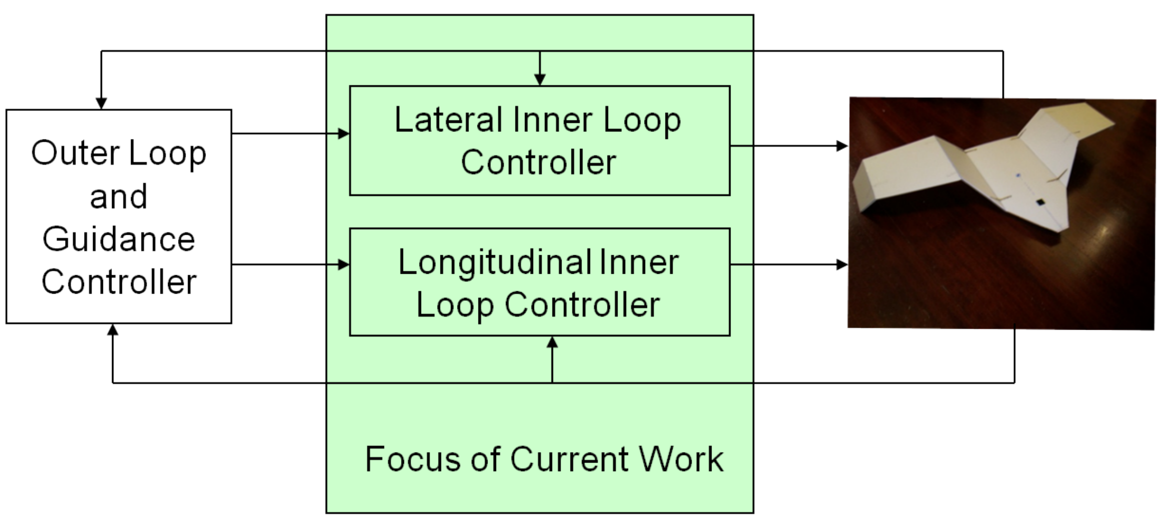

Figure 3-1: High Level Control Law Architecture

Challenges of Controller Design for Morphing Vehicles

In their most basic state-space form, the equations of motion for a vehicle can be given in the form of Equation 3.1.

$$\dot{x} = f(x,u) \tag{3.1}$$

In 3.1, *f* is a nonlinear function in the state variables *x* and the control inputs *u*. Generally in control design, these equations of motion are linearized about an operating point to obtain linear time invariant (LTI) state space systems of the form of Equation 3.2 that are valid at conditions close to the operating point and for which a multitude of control design and analysis techniques exist.

$$\dot{x} = Ax + Bu \tag{3.2}$$

For a morphing vehicle an additional complication is added; the dynamics also become a function of the morphing configuration, and possibly the rate of change of the morphing surfaces. So the equation then would take the form of Equation 3.3.

$$\dot{x} = f(x,u,\mu,\dot{\mu}) \tag{3.3}$$

In Equation 3.3, μ represents the morphing angle and $\dot{\mu}$ the morphing rate. The changes in dynamics come both from unsteady aerodynamic effects created by wing surface motion through the air, as well as inertial forces generated by accelerating the mass of the surfaces relative to the body.

Several possibilities exist to model the influence of the additional terms. These include adding μ and $\dot{\mu}$ as states in the system or control inputs to the system. The approach used here is to first linearize the model at a set of morphing angles under the assumption that the morphing rate is slow relative to the rigid body dynamics of airframe. Under these assumptions, the equations of motion can be represented as a linear parameter varying (LPV) system in the form shown in Equation (3.4).

$$\dot{x} = A(\mu)x + B(\mu)u \tag{3.4}$$

Linear controllers can then be designed at each of three design configurations (low-speed, gull-wing, and high-speed), and the gains scheduled between the design points as a function of μ. During the transition phase the LPV equations in 3.4 should provide a good approximation to the actual dynamics if $\dot{\mu}$ is slow compared to the dynamics of the system. In the case of higher $\dot{\mu}$ an additional term is needed that captures the unsteady effects. In this case the equations will be in the form of Equation 3.5.

$$\dot{x} = A(\mu)x + B(\mu)u + d(x, \mu, \dot{\mu}) \tag{3.5}$$

In 3.5, *d* represents the unsteady and likely nonlinear effects on the dynamics during morphing. The vortex lattice code that has been used to generate the aerodynamics model here is not capable of accurately capturing these unsteady terms. To accurately capture these effects would require a more complex CFD technique, wind tunnel runs, or flight tests. All of these would require a significant amount of time and expense to capture completely. In addition, attempting to design controllers to perfectly take the unsteady effects into account could lead to overly complex controllers. Instead, it is desirable to design controllers using systems of the form of Equation 3.4 and either make them robust to the unmodeled transient dynamics, or enforce a rate limit on the configuration change such that *d* is negligible.

Outer Loop and Guidance Controller

The outer loop and guidance controllers were designed to regulate the vehicle to a reference trajectory. The structure of these controllers was carried over from previous projects in the VSTL (for example [4]), and the inner loop controllers developed later were designed to work inside this framework. The guidance commands are generated based on track regulation to waypoints generated as Bezier curves. This is combined with pitch commands generated to maintain a constant altitude in straight and turning flight. The output from the guidance controllers is then passed through nonlinear constraint equations that generate aircraft attitude commands based on steady climb and coordinated turn constraints. The result is commands for pitch rate Q, sideslip angle β, and roll rate P that are used as the reference commands for the inner loop controllers. The following discussions are a condensed version of Reference [4].

Track Regulation

Guidance commands for track regulation are generated using a look-ahead scheme that computes a target heading to some reference trajectory. A pseudo location on the reference trajectory is chosen as the nearest point to the vehicle that lies on the reference trajectory as shown in Figure 3-2.

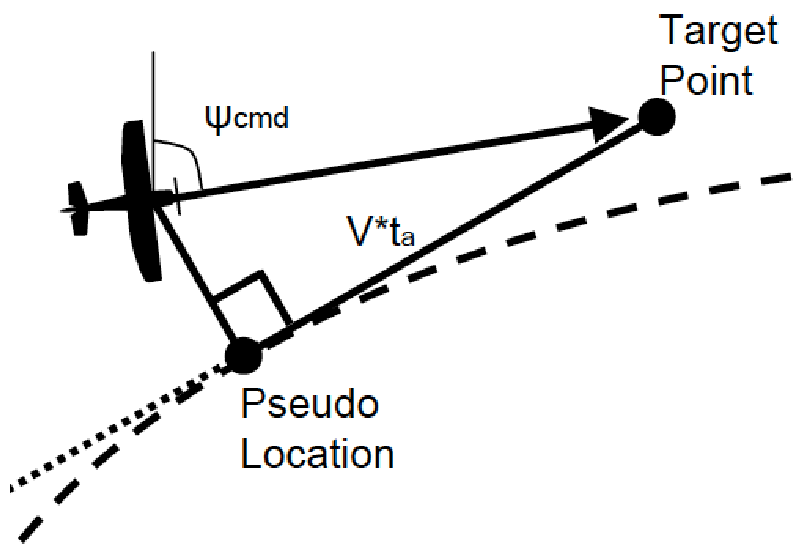

Figure 3-2: Cross track regulation using a look-ahead [4]

A target point is then computed at a distance equal to $|V|t_a$ where $|V|$ is the magnitude of the vehicle's velocity and t_a is the look-ahead time. The location of the target point, as implemented here, is selected to be along the line tangent to the reference trajectory at the pseudo location point.

The reference trajectories are composed of cubic Bezier curves between waypoints. Equation 3.6 gives a mathematical representation of a Bezier curve

$$\vec{B}(u) = \vec{x}_1(1-u)^3 + 3(\vec{x}_1 + \vec{c}_1)u(1-u)^2 + 3(\vec{x}_2 + \vec{c}_2)u^2(1-u) + \vec{x}_2 u^3 \quad (3.6)$$

where $u \in [0,1]$ is a parametric variable. Figure 3-3 shows a graphical representation of a Bezier curve waypoint track.

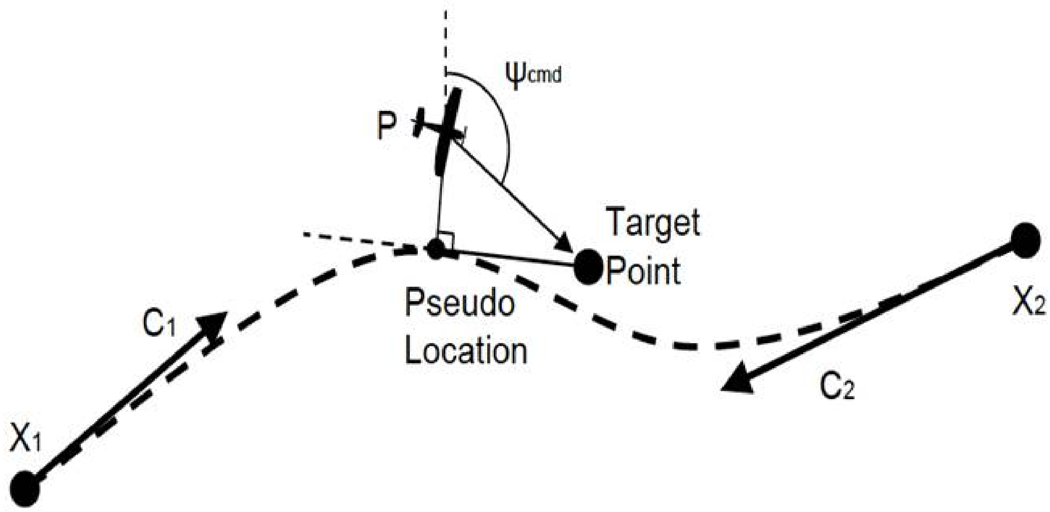

Figure 3-3: Geometric Definition of a Bezier Curve [4]

The pseudo location on the reference trajectory corresponds to a location where the tangent vector is perpendicular to a vector pointed at the vehicle as shown in Figure 3-3 and is shown mathematically in Equation 3.7.

$$\begin{aligned} \vec{r}(u) &= \vec{P} - \vec{B}(u) \\ 0 &= \vec{r}(u)^T \frac{d\vec{B}(u)}{du} \end{aligned} \tag{3.7}$$

This results in a 5^{th} order polynomial in u that has no analytical solution. This equation is solved iteratively using Newton's method as described in [4]. The result is a heading command required to turn the vehicle towards the target point. This command is also augmented with a turn rate command based on the reference track curvature at the pseudo location.

Nonlinear Outer Loop Control

The outer loop control is implemented to turn the guidance commands for altitude and track regulation into commands for pitch angle θ, sideslip angle β, and roll angle ϕ. In a steady climb, the flight path angle (γ), angle of attack (α), β, and θ are related by Equation 3.8 [10].

$$
\begin{aligned}
&a = \cos(\alpha)\cos(\beta) \\
&b = \sin(\phi)\sin(\beta) + \cos(\phi)\sin(\alpha)\cos(\beta) \\
&\tan(\theta) = \frac{ab + \sin(\gamma)\sqrt{a^2 - \sin^2(\gamma) + b^2}}{a^2 - \sin^2(\gamma)}
\end{aligned}
\tag{3.8}
$$

Similarly, in a steady, coordinated turn the aircraft's roll angle (ϕ) is related to the desired turn rate ($\dot{\psi}$) by Equation 3.9 [10].

$$
\begin{aligned}
&\aleph = \frac{\dot{\psi} V_T}{g} \\
&a = 1 - \aleph \tan(\alpha)\sin(\beta) \\
&b = \sin(\gamma)/\cos(\beta) \\
&c = 1 + \aleph^2 \sin^2(\beta) \\
&\tan(\phi) = \aleph \frac{\cos(\beta)}{\cos(\alpha)} \frac{(a - b^2) + b\tan(\alpha)\sqrt{c(1 - b^2) + \aleph^2 \sin^2(\beta)}}{a^2 - b^2(1 + c\tan^2(\alpha))}
\end{aligned}
\tag{3.9}
$$

To produce the appropriate θ, β, and ϕ commands for the desired trajectory, γ_{cmd} based on altitude error is substituted into Equation 3.8 to produce a commanded pitch θ_{cmd} for use in the inner loop controller and $\dot{\psi}$ from the guidance control law is substituted into Equation 3.9 to produce a roll angle command ϕ_{cmd}. The commanded sideslip angle, β_{cmd}, is initially set to 0 for all cases to attempt to execute sideslip free turns. Figure 3.4 shows a graphical description of the outer loop control function.

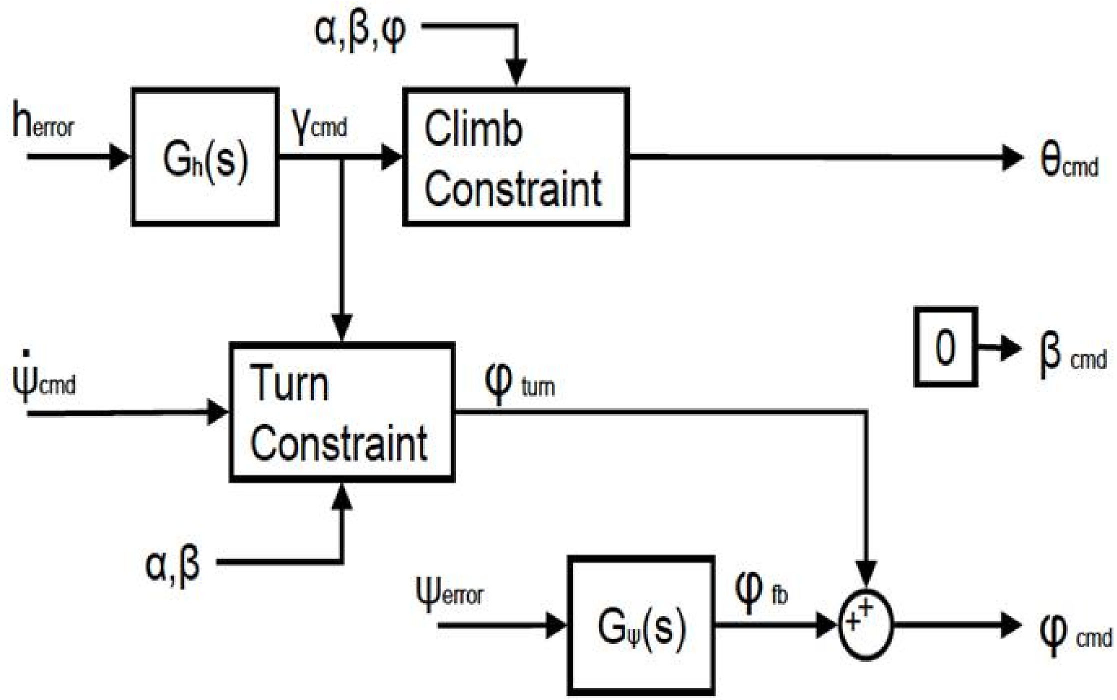

Figure 3-4: Nonlinear outer loop control architecture with turn and climb constraints [4].

As implemented here $G_h(s)$ is a PID controller on altitude error and $G_\psi(s)$ is a PI controller based on inertial heading error. The gains used in $G_h(s)$ and $G_\psi(s)$ were left unchanged from those used in Reference [4], but may require tuning to achieve acceptable performance during flight test.

Longitudinal Axes

The longitudinal axis control structure was designed to allow capture and tracking of a commanded altitude as well as compensation for the pitch rate required for a coordinated level flight turn. As shown in Figure 3-4 above, the guidance and outer loop controllers generate a pitch angle command. This pitch angle command is then passed through compensator to create a pitch rate command. Here the compensator is a simple proportional gain on the pitch angle error. Turn compensation is achieved through the use of a feed forward pitch rate bias added on top of this command. The inner loop controller is designed to track the final pitch rate command. This is accomplished through the use of a linear tracker with output feedback of pitch rate Q and angle of attack α to the elevator. An integrator is placed in the Q path to achieve small steady state error (type-1 controller). The design is carried out using an optimal control technique based on a quadratic cost function with time weighting. This leads to a controller that uses pitch to track altitude while speed is controlled by throttle. The speed controller is a simple proportional plus integral controller based on speed error from the commanded speed and will not be discussed in detail.

Longitudinal Inner Loop Controller Design

The goal of the inner loop longitudinal controller will be to regulate the vehicle to a commanded pitch angle θ generated by the outer loop and guidance laws. Because the change in the dynamics from one morph angle to another is relatively small, the goal will be to design one controller that provides satisfactory performance and robustness for all three configurations. The 45 degree morph angle gull-wing configuration will be used as the starting point as it represents a middle of the road configuration in terms of matrix element variation. Later, a model reference adaptive controller will be added to the pitch inner as an augmentation to account for dynamics due to morphing.

First the error to the commanded pitch angle is multiplied by a proportional gain to generate a pitch rate command (Q_{cmd}). The control scheme used for pitch rate control is an output feedback tracker with additional inner loop output feedback and a dynamic compensator as shown in Figure 3-5.

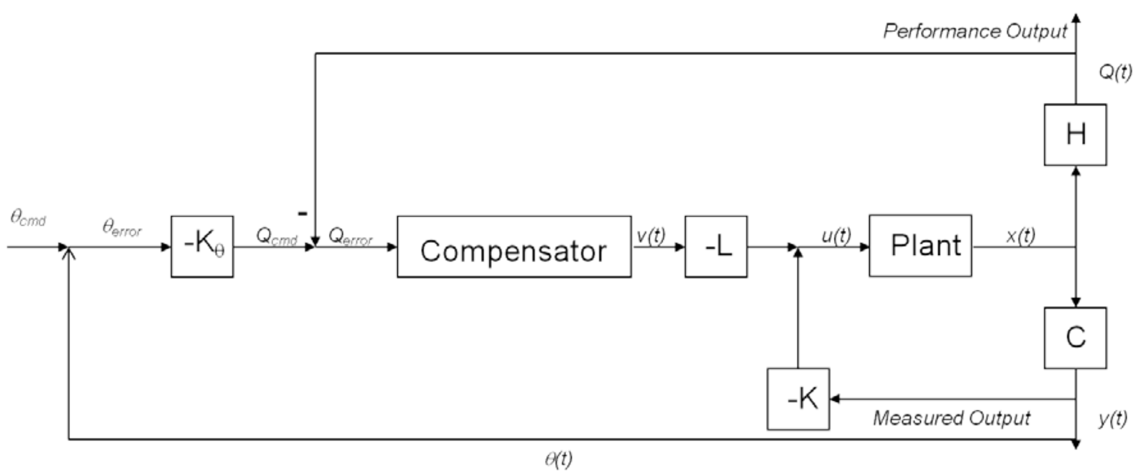

Figure 3-5: Output feedback tracker with a compensator of desired structure

The goal of the *Q* controller is to drive the performance output *Q(t)* to follow closely the reference command $Q_{cmd}(t)$. This structure was used in conjunction with an output feedback LQ optimal control design method using a time weighted cost function to find the optimal gain. This controller structure is a powerful tool for aircraft control design because it does not require state feedback, which is often not practical for real aircraft. It also allows the use of a compensator of any desired structure to be included in the forward path. This means that classical control architectures that have proven to give desired performance and robustness characteristics for different aircraft control problems can be recreated easily. The LQ design method allows us to find optimal gains K and L for all loops simultaneously, as well as set the parameters of complex compensators. For more background on the use of the output feedback tracker with a desired compensator and many examples of its application to aircraft control problems, see [10]. What follows is a discussion of the implementation used here.

Let us start with the plant in standard state space form, which here is the short period longitudinal dynamics as given in Equation 3.10.

$$
\begin{aligned}
\dot{x} &= Ax + Bu \\
y &= Cx \\
\begin{bmatrix} \dot{\alpha} \\ \dot{Q} \end{bmatrix} &= \begin{bmatrix} -11.5 & 0.7 \\ -26.2 & -1.6 \end{bmatrix} \begin{bmatrix} \alpha \\ Q \end{bmatrix} + \begin{bmatrix} -1.8 \\ -8.4 \end{bmatrix} \delta_e \\
\begin{bmatrix} \alpha \\ Q \end{bmatrix} &= \begin{bmatrix} 1 & 0 \\ 0 & 1 \end{bmatrix} \begin{bmatrix} \alpha \\ Q \end{bmatrix}
\end{aligned}
\tag{3.10}
$$

Next we define the *performance output* that should be driven to follow the reference command. Often, the performance output is simply a plant output, although this is not a requirement. Here the performance output is the pitch rate *Q*.

$$
\begin{aligned}
z &= Hx \\
Q &= \begin{bmatrix} 0 & 1 \end{bmatrix} \begin{bmatrix} \alpha \\ Q \end{bmatrix}
\end{aligned}
\tag{3.11}
$$

The dynamic compensator can be of any desired structure. Here, a simple integrator on the error between the commanded pitch rate and the actual pitch rate was used. Equation 3.12 shows the state space equations of the compensator.

$$
\begin{aligned}
\dot{w} &= Fw + Ge \\
v &= Dw + Je \\
\dot{e}_I^Q &= 0e_I^Q + 1e \\
e_I^Q &= 1e_I^Q + 0e \\
e &= r - z = r - Hx = Q_{ref} - Q
\end{aligned}
\tag{3.12}
$$

The control input to the plant, u, is given by equation 3.13

$$
\begin{aligned}
u &= -Ky - Lv \\
\delta_e &= -\begin{bmatrix} K_\alpha & K_Q \end{bmatrix} \begin{bmatrix} \alpha \\ Q \end{bmatrix} - L_{e_I^Q} e_I^Q
\end{aligned}
\tag{3.13}
$$

This set of dynamics can be arranged into the augmented form representing the entire system as

$$
\begin{aligned}
&\underbrace{\begin{bmatrix} \dot{x} \\ \dot{w} \end{bmatrix}}_{\dot{\tilde{x}}} = \underbrace{\begin{bmatrix} A & 0 \\ -GH & F \end{bmatrix}}_{\tilde{A}} \underbrace{\begin{bmatrix} x \\ w \end{bmatrix}}_{\tilde{x}} + \underbrace{\begin{bmatrix} B \\ 0 \end{bmatrix}}_{\tilde{B}} u + \underbrace{\begin{bmatrix} 0 \\ G \end{bmatrix}}_{\tilde{G}} r \\
&\underbrace{\begin{bmatrix} y \\ v \end{bmatrix}}_{\tilde{y}} = \underbrace{\begin{bmatrix} C & 0 \\ -JH & D \end{bmatrix}}_{\tilde{C}} \underbrace{\begin{bmatrix} x \\ w \end{bmatrix}}_{\tilde{x}} + \underbrace{\begin{bmatrix} 0 \\ J \end{bmatrix}}_{\tilde{F}} r \\
&z = \underbrace{\begin{bmatrix} H & 0 \end{bmatrix}}_{\tilde{H}} \underbrace{\begin{bmatrix} x \\ w \end{bmatrix}}_{\tilde{x}} \\
&u = -\underbrace{\begin{bmatrix} K & L \end{bmatrix}}_{\tilde{K}} \underbrace{\begin{bmatrix} y \\ v \end{bmatrix}}_{\tilde{y}}
\end{aligned}
\tag{3.14}
$$

Which for the problem presented here becomes Equation 3.15.

$$
\begin{aligned}
\underbrace{\begin{bmatrix} \dot{\alpha} \\ \dot{Q} \\ \dot{e}_I^Q \end{bmatrix}}_{\tilde{x}} &= \underbrace{\begin{bmatrix} -11.5 & 0.7 & 0 \\ -26.2 & -1.6 & 0 \\ 0 & -1 & 0 \end{bmatrix}}_{\tilde{A}} \underbrace{\begin{bmatrix} \alpha \\ Q \\ e_I^Q \end{bmatrix}}_{\tilde{x}} + \underbrace{\begin{bmatrix} -1.8 \\ -8.4 \\ 0 \end{bmatrix}}_{\tilde{B}} \delta_e + \underbrace{\begin{bmatrix} 0 \\ 0 \\ 1 \end{bmatrix}}_{\tilde{G}} r \\
\underbrace{\begin{bmatrix} \alpha \\ Q \\ e_I^Q \end{bmatrix}}_{\tilde{y}} &= \underbrace{\begin{bmatrix} 1 & 0 & 0 \\ 0 & 1 & 0 \\ 0 & 0 & 1 \end{bmatrix}}_{\tilde{C}} \underbrace{\begin{bmatrix} \alpha \\ Q \\ e_I^Q \end{bmatrix}}_{\tilde{x}} + \underbrace{\begin{bmatrix} 0 \\ 0 \\ 0 \end{bmatrix}}_{\tilde{F}} r \\
z &= \underbrace{\begin{bmatrix} 0 & 1 & 0 \end{bmatrix}}_{\tilde{H}} \underbrace{\begin{bmatrix} \alpha \\ Q \\ e_I^Q \end{bmatrix}}_{\tilde{x}} \\
u &= -\underbrace{\begin{bmatrix} K_\alpha & K_Q & L_{e_I^Q} \end{bmatrix}}_{\tilde{K}} \underbrace{\begin{bmatrix} \alpha \\ Q \\ e_I^Q \end{bmatrix}}_{\tilde{y}}
\end{aligned} \tag{3.15}
$$

Note that for the case with no angle of attack feedback K_α is zero.

The control problem is to find $\tilde{K}$ such that the control law $u = -\tilde{K}\tilde{y}$ drives the performance output z to follow the reference command in some optimal way. Optimality here means minimizing the value of some performance index or cost function J. Many different cost functions can and have been used. Perhaps the most common form of cost function is that of Equation 3.16.

$$
J = \frac{1}{2}\int_0^\infty x^T Q x + u^T R u \, dt \tag{3.16}
$$

Where Q and R are weighting matrices with Q positive semi-definite and R positive definite. Minimizing this cost function finds the controller that minimizes the state errors and control inputs given weights specified by the designer. For a state feedback system, the solution is well known and given by

$$K = R^{-1} B^T P \tag{3.17}$$

Where P is the solution to the algebraic Riccati equation in Equation 3.18.

$$PA + A^T P - PBR^{-1} BP + Q = 0 \tag{3.18}$$

This is known as the linear quadratic regulator (LQR) problem. There are many tools that can be used to solve this equation. In general system characteristics are modified by tuning the values of the Q and R matrices, which in turn modifies the gain matrix K. With some conditions holding true, this solution guarantees infinite gain margin and 60° degrees of phase margin. This is the design method used to find the gains when angle of attack feedback is included, since that design corresponds to the state feedback case.

Unfortunately, for many practical airplane control problems (including the problem presented here with no alpha feedback), state feedback is not a possibility and this method is not directly applicable, although an implementation that includes an optimal state observer (Linear Quadratic Gaussian, LQG) also provides good characteristics with well known solutions. Another drawback is that as the number of states increases, so does the number of weighting parameters in the Q and R matrices. Intuition about what changes should be made to alter the system performance can be quickly lost. It can also be unclear how the cost function relates to design requirements.

A more practical and intuitive approach to finding the gain matrices is given in [10]. Here, output feedback is used with a variety of different cost functions that are based on intuitive and reasonable goals for the system performance. The one chosen to be used here is given in Equation 3.19.

$$J = \frac{1}{2}\int_0^\infty [(t^k \hat{x}^T P \hat{x} + \hat{x}^T (Q + \tilde{C}^T \tilde{K}^T R \tilde{K} \tilde{C}) \hat{x}] \, dt \tag{3.19}$$

Where *k* is a positive integer and P, Q, and R are weighting matrices chosen by the designer and $\hat{x}$ is the state deviation from the nominal steady state value. A sensible design goal is to minimize the tracking error of the system while keeping the control effort small. This can be accomplished by using $P = \tilde{H}^T \tilde{H}$, $Q = 0$ and $R = rI$ in 3.19. This results in the cost function:

$$J = \frac{1}{2}\int_0^\infty (t^k e^T e + r u^T u) \, dt \tag{3.20}$$

Equation 3.20 is a desirable cost function because it has a direct intuitive relationship to tracking performance, the time weighted term encourages a control solution that penalizes long term steady state errors, and there are now only two design parameters to be tuned: *k* and *r*.

Due to the term t^k the strictly optimal solution of Equation 3.20 would be time varying. This is undesirable because it would greatly complicate gain scheduling in a practically implementable control law. In order to obtain a useful solution, we will instead find the suboptimal time-invariant solution to 3.20. The other drawback to using this cost function as compared to Equation 3.16, is that the solution is not as straightforward as solving an algebraic Riccati equation.

As shown in [10], we can find the value of *J* for a given value of $\tilde{K}$ in Equation 3.20 by successively integrating by parts and then solving the nested Lyapunov equations in Equation 3.21.

$$
\begin{aligned}
&0 = g_0 \equiv A_c^T P_0 + P_0 A_c + P \\
&0 = g_1 \equiv A_c^T P_1 + P_1 A_c + P_0 \\
&\vdots \\
&0 = g_{k-1} \equiv A_c^T P_{k-1} + P_{k-1} A_c + P_{k-2} \\
&0 = g_k \equiv A_c^T P_k + P_k A_c + k! P_{k-1} + Q + C^T K^T RKC \\
&A_c = \tilde{A} - \tilde{B}\tilde{K}\tilde{C}
\end{aligned} \tag{3.21}
$$

Then, the value of Equation 3.20 is given by

$$
\begin{aligned}
&J = \frac{1}{2} tr(P_k X) \\
&X = A_c^{-1} B_c r_0 r_0^T B_c^T (A_c^{-1})^T \\
&B_c = \tilde{G} - \tilde{B}\tilde{K}\tilde{F}
\end{aligned} \tag{3.22}
$$

Here r_0 is a unit step input of magnitude r_0.

To find the optimal gain $\tilde{K}$, the equations in 3.21 and 3.22 were solved iteratively and the MATLAB simplex optimization routine *fminsearch* was used to minimize J over all possible values of $\tilde{K}$. A practical consideration in running this design algorithm comes from choosing the initial gain $\tilde{K}_0$ to initialize the iterative algorithm. The gain must make the closed loop system stable, that is $A_c = \tilde{A} - \tilde{B}\tilde{K}_0\tilde{C}$ is Hurwitz. This is not always a trivial task, especially for a complex system. One possible technique, and the one used here, is to first solve a state feedback problem (for which many solution techniques exist), then modify the cost function to penalize the gains corresponding to the states which are not used in the output feedback configuration. So in 3.22 J becomes

$$
J = \frac{1}{2} tr(P_k X) + \sum g_{i,j} k_{i,j} \tag{3.23}
$$

Where $g_{i,j}$ is a weighting term corresponding to $k_{i,j}$ the i,j^{th} element of the gain matrix and is large for gains to be zeroed and small for all others. For the design where only pitch rate feedback is used, the state feedback solution is used as the initial gain, and the weighting corresponding to the angle of attack feedback gain is set to 10^4.

Using this design technique with *k=2* and *r=1* in Equation 3.20, the longitudinal gain matrices for the inner loop pitch rate controllers are found to be:

$$
\begin{aligned}
&\textit{With } \alpha \textit{ feedback}: \\
&\tilde{K} = \begin{bmatrix} 0.9917 & -1.1283 & 3.1623 \end{bmatrix} \\
&\textit{Without } \alpha \textit{ feedback}: \\
&\tilde{K} = \begin{bmatrix} 0 & -1.3620 & 4.9136 \end{bmatrix}
\end{aligned}
\tag{3.24}
$$

The gain and phase margins for each configuration were computed using the MATLAB *margin* command with a 50 millisecond delay included to represent processing and data transmission delays. Figure 3-6 shows the open loop bode diagram showing the gain and phase margins. As can be seen in the figure, the gain and phase margins are similar for all three design configurations with the gains given here. The gain margins are all close to 10 dB and the phase margin is approximately 70 degrees.

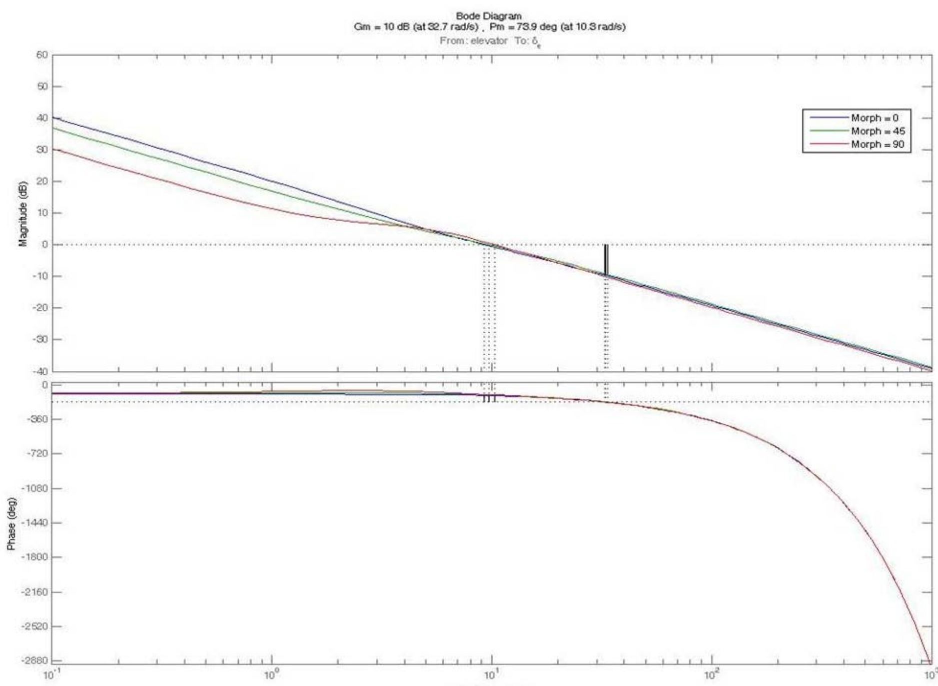

Figure 3-6: Pitch Bode plot showing phase and gain margins

Figure 3-7 shows the closed loop step response of each configuration to a 10 degree/sec step command and compares the two controllers to each other. The step responses are consistent between the two controllers and from configuration to configuration.

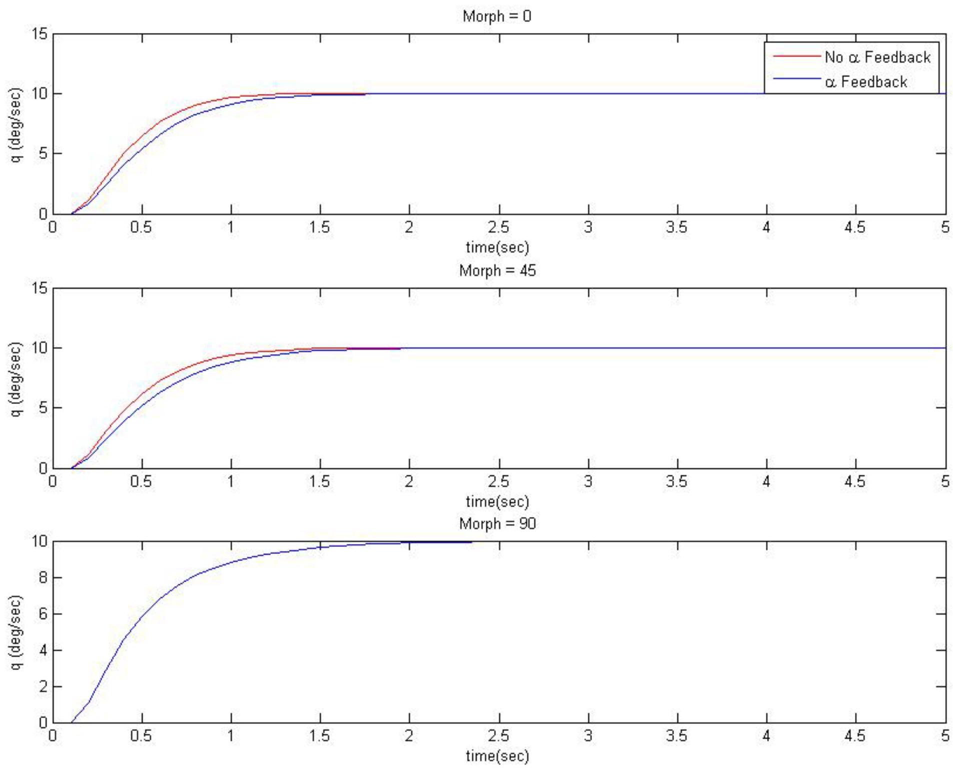

Figure 3-7: Step response to a *Q* command of 10 degrees/sec for the low-speed (top), gull-wing (middle), and high-speed (bottom) configurations at a trim airspeed of 6 m/s for both the case of angle of attack feedback and no angle of attack feedback with 50ms delay included

Figure 3-8 and Figure 3-9 show the pitch rate step response for the controller without angle of attack feedback and the controller with angle of attack feedback respectively. Both controllers provide good step response characteristics, although the controller without angle of attack feedback uses slightly more control effort. Since the controller with no angle of attack feedback provides acceptable performance, the simulations that follow will use the controller without angle of attack feedback. The final decision regarding α feedback should be made following flight tests.

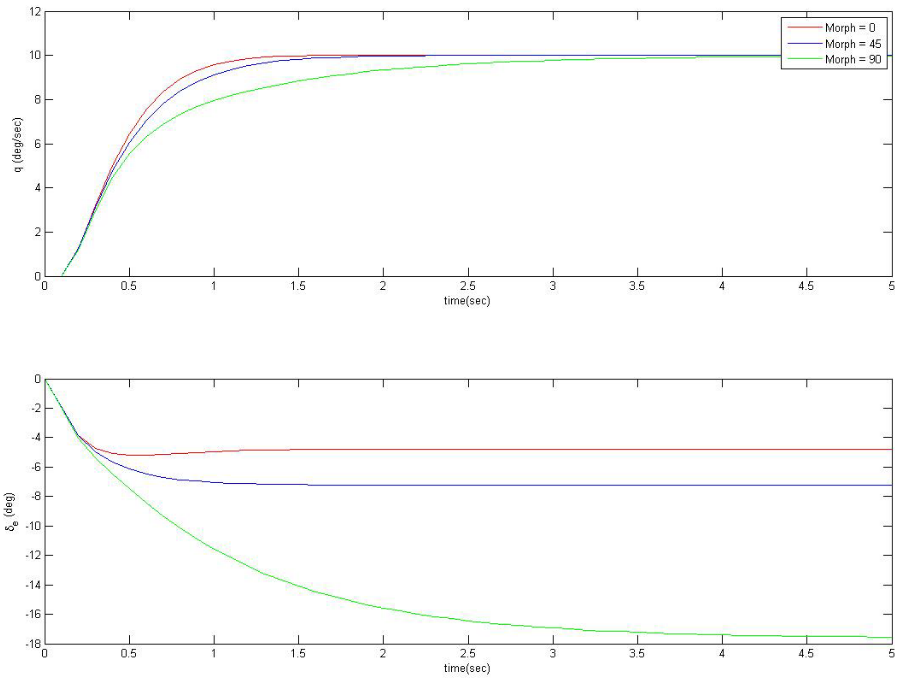

Figure 3-8: Pitch rate step response and elevator deflection to a 10 degree/sec command for the longitudinal controller without angle of attack feedback with 50ms delay included

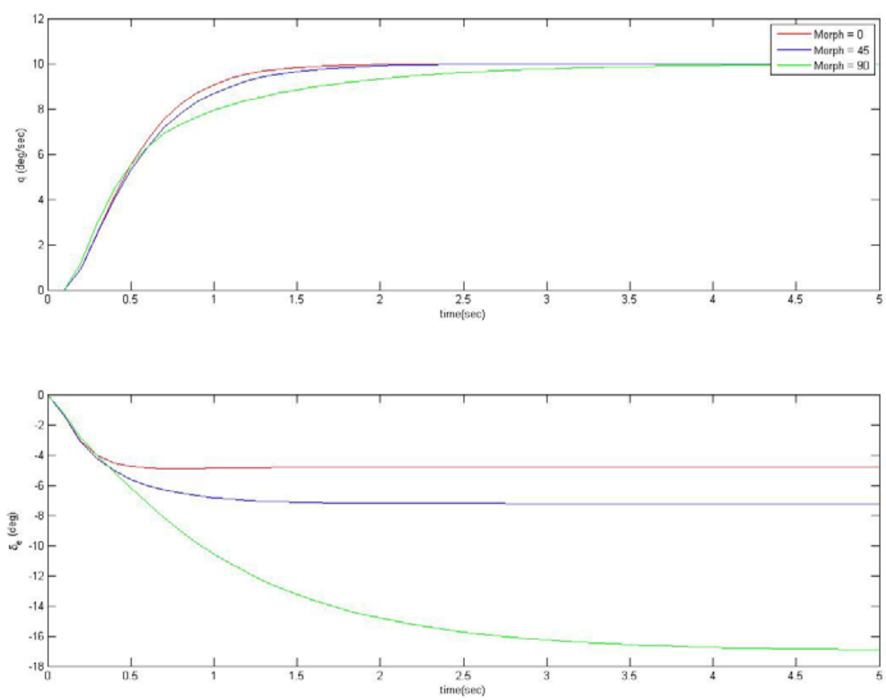

Figure 3-9: Pitch rate step response and elevator deflection to a 10 degree/sec command for the longitudinal controller with angle of attack feedback with 50ms delay included

To assess the performance of the controller more closely to how it will be used during flight, a simulation was built in Simulink. The simulation uses aerodynamic data at several values of the morph angle and linearly interpolates between them as a function of the morph angle. The input is pitch angle command which is then passed through a proportional compensator on pitch angle error. The gain for this compensator was set empirically to 2 rad/s/rad. The simulation also includes a representative time delay for data acquisition and processing of 50ms an actuator rate limit of 5 rad/sec and total throw limits of +/- 30 degrees . Figure 3-10 shows the vehicle response to series of step pitch commands while the morph angle is swept. As can be seen, the tracking performance is good with only minimal overshoots, even during the configuration changes.

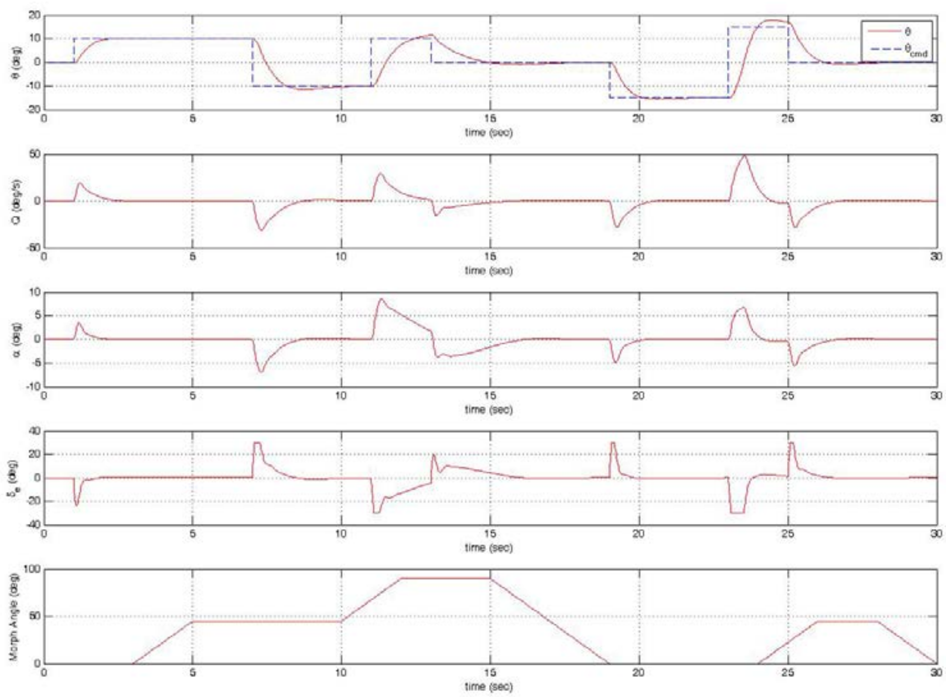

Figure 3-10: Longitudinal response to 3-2-1 command in pitch angle while undergoing configuration change. Includes 50ms time delay, 5 rad/sec actuator rate limit, and 30 degree actuator throw limit

As discussed earlier, this simulation does not contain a model for the unsteady dynamics that could be present during morphing and the control law used does not attempt to make any adjustments for those dynamics. Later an adaptive control law that could be used to add more robustness in the presence of such dynamics will be discussed.

Lateral Directional Axes

The lateral directional axes control structure was designed to allow two dimensional trajectory tracking. The guidance law computes a turn rate command based on track error from a Bezier waypoint scheme as described previously. An intermediate controller translates this command into a bank to turn command that creates a body axis roll angle command. Finally, the inner loop controller is a roll rate and sideslip tracking design that uses explicit model following to provide desirable Dutch roll and roll mode characteristics to allow for acceptable trajectory tracking performance. Because the lateral directional dynamics vary widely as the morph angle is changed, gain scheduling as a function of the morph angle is used to compensate for the changes in dynamics.

Lateral Directional Inner Loop Controller Design

The goal of the lateral-directional inner loop controller is to regulate the aircraft to a given sideslip angle β and roll rate P as commanded by the guidance and outer loop control laws. The method employed was an explicit model following tracker designed using linear quadratic techniques. A reference model was chosen based on the desired inner loop dynamics, and the control goal was to minimize the integrated error between the reference model and the aircraft state. The design process was repeated at the low-speed, gull-wing, and high-speed configurations producing three independent sets of gains. The control structure is shown in Figure 3-11 and is similar to that described in [13] as well as [4].

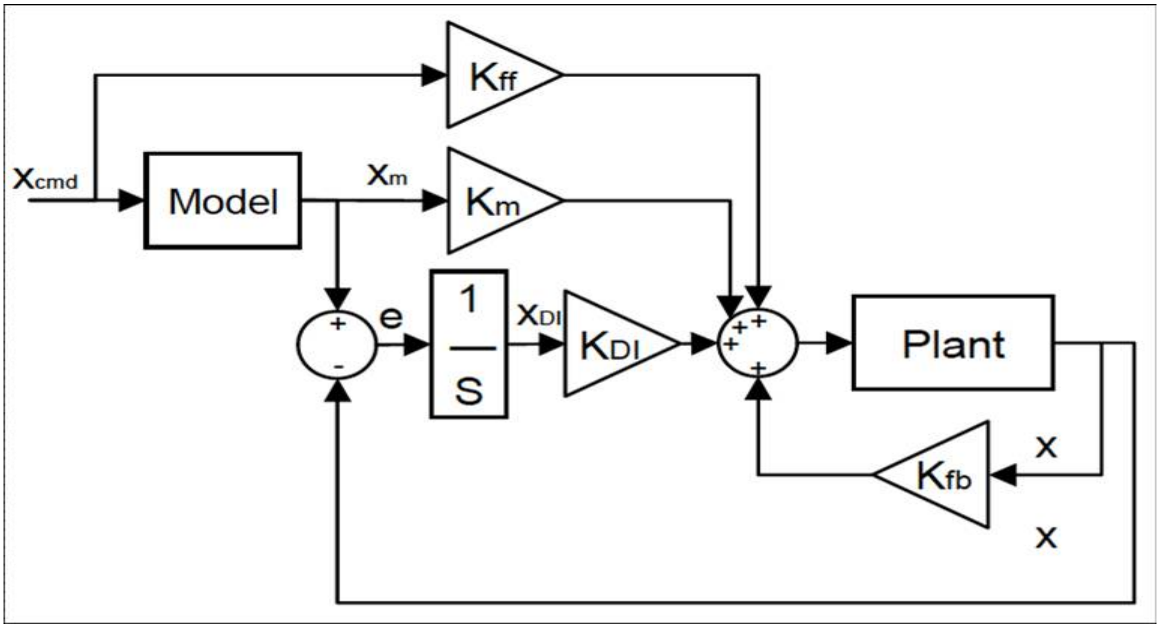

Figure 3-11: Explicit model following, integral LQ tracker architecture [4].

Equation 3.25 describes the control law dynamics.

$$\underbrace{\begin{bmatrix} \dot{e}_{yI}^{\beta} \\ \dot{e}_{yI}^{P} \\ \dot{\beta}_{m1} \\ \dot{\beta}_{m2} \\ \dot{P}_m \end{bmatrix}}_{\dot{x}_{claw}^{latd}} = \underbrace{\begin{bmatrix} 0 & 0 & 1 & 0 & 0 \\ 0 & 0 & 0 & 0 & 1 \\ 0 & 0 & 0 & 1 & 0 \\ 0 & 0 & -2\zeta_{\beta}\omega_{\beta} & -\omega_{\beta}^2 & 0 \\ 0 & 0 & 0 & 0 & -\omega_P \end{bmatrix}}_{A_{claw}^{latd}} \underbrace{\begin{bmatrix} e_{yI}^{\beta} \\ e_{yI}^{P} \\ \beta_{m1} \\ \beta_{m2} \\ P_m \end{bmatrix}}_{x_{claw}^{latd}} + \underbrace{\begin{bmatrix} -1 & 0 & 0 & 0 & 0 \\ 0 & -1 & 0 & 0 & 0 \\ 0 & 0 & 0 & 0 & 0 \\ 0 & 0 & 0 & \omega_{\beta}^2 & 0 \\ 0 & 0 & 0 & 0 & \omega_P \end{bmatrix}}_{B_{claw}^{latd}} \underbrace{\begin{bmatrix} \beta \\ P \\ R \\ \beta_{cmd} \\ P_{cmd} \end{bmatrix}}_{u_{claw}^{latd}}$$

$$\underbrace{\begin{bmatrix} \delta_a \\ \delta_r \end{bmatrix}}_{y_{claw}^{latd}} = -\underbrace{\begin{bmatrix} [K_{DI}] & [K_m] \end{bmatrix}}_{C_{claw}^{latd}} \underbrace{\begin{bmatrix} e_{yI}^{\beta} \\ e_{yI}^{P} \\ \beta_{m1} \\ \beta_{m2} \\ P_m \end{bmatrix}}_{x_{claw}^{latd}} - \underbrace{\begin{bmatrix} [K_{fb}] & [K_{ff}] \end{bmatrix}}_{D_{claw}^{latd}} \underbrace{\begin{bmatrix} \beta \\ P \\ R \\ \beta_{cmd} \\ P_{cmd} \end{bmatrix}}_{u_{claw}^{latd}} \tag{3.25}$$

The 3rd through 5th rows of the state equation represent a 2nd order β response model and 1st order P response model. The model parameters are chosen to give the aircraft good response characteristics to β commands and P commands. In piloted aircraft, this technique is often used to give the aircraft consistent handling qualities across a wide range of the flight envelope. Here the dynamics will be defined in a way that will ensure good performance of the inner loop controllers in regulating to the outer loop guidance commands. The values for the model parameters chosen are shown in Equation 3.26.

$$\begin{aligned}\omega_\beta &= 4\ rad/s \\ \zeta_\beta &= 0.7 \\ \omega_P &= 10\, rad/s\end{aligned} \tag{3.26}$$

The beta response model is defined as follows:

1. The frequency is comparable to the Dutch roll frequency of the configuration with the slowest Dutch roll
2. The damping is comparable to the damping of the configuration with the highest damping.

Figure 3-12 shows the step response represented by these ideal models. This response will be the ideal goal for the closed loop dynamics of the aircraft.

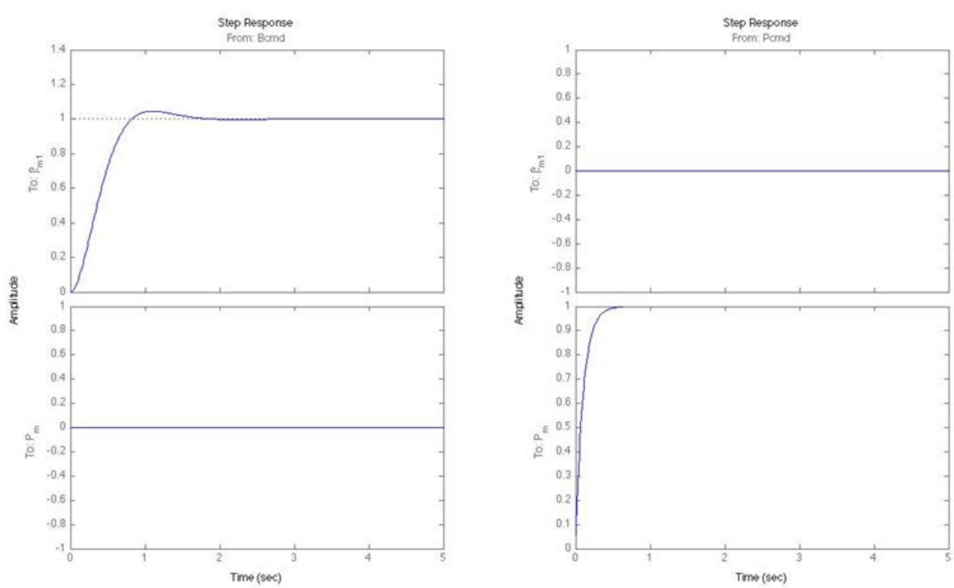

Figure 3-12: Ideal model step response for $\omega_\beta = 4$ rad/s, $\zeta_\beta = 0.7$, and $\omega_P = 10$ rad/s.

We proceed with design of the controller by augmenting the open loop with states for the ideal models and the integrated difference of the plant outputs to the ideal model states as shown in Equation 3.27.

$$\underbrace{\begin{bmatrix} \dot{x}_p^{latd} \\ \dot{x}_{claw}^{latd} \end{bmatrix}}_{\dot{x}^{syn}} = \underbrace{\begin{bmatrix} A_p^{latd} & 0 \\ B_{claw}^{latd}(1:5,1:3) & A_{claw}^{latd} \end{bmatrix}}_{A^{syn}} \underbrace{\begin{bmatrix} x_p^{latd} \\ x_{claw}^{latd} \end{bmatrix}}_{x^{syn}} + \underbrace{\begin{bmatrix} B_p^{latd} \\ 0 \end{bmatrix}}_{B^{syn}} \underbrace{\begin{bmatrix} \delta_a \\ \delta_r \end{bmatrix}}_{u^{latd}} + \underbrace{\begin{bmatrix} 0 \\ B_{claw}^{latd}(1:5,4:5) \end{bmatrix}}_{B_r^{latd}} \underbrace{\begin{bmatrix} \beta_{cmd} \\ P_{cmd} \end{bmatrix}}_{r^{latd}} \tag{3.27}$$

$$y^{lqr} = C^{syn} x^{syn} + D^{syn} u^{latd}$$

Output weighted LQR will be employed to find gains $K^{latd}=(K_{fb}\ K_{DI}\ K_m)$ such that the cost function given in Equation 3.28 is minimized by the control law $u^{latd}=-K^{latd}x^{syn}$.

$$J = \int_0^\infty (y^{syn^T} Q y^{syn} + u^{p^T} R u^p)dt \tag{3.28}$$

Again, Q and R are weighting matrices with Q positive semi-definite and R positive definite. Similar to the state weighted case in Equation 3.16, it can be shown that the gain matrix K^{latd} that minimizes Equation 3.28 is given by Equation 3.29.

$$K^{latd} = R^{-1} B^{syn^T} P \tag{3.29}$$

P in Equation in 3.29 is again the solution to the algebraic Ricatti equation in Equation 3.30.

$$\begin{gathered} PA^{syn} + A^{syn^T} P - PB^{syn} \overline{R}^{-1} B^{syn} P + \overline{Q} = 0 \\ \begin{bmatrix} \overline{Q} & 0 \\ 0 & \overline{R} \end{bmatrix} = \begin{bmatrix} C^{syn^T} & 0 \\ D^{syn^T} & I \end{bmatrix} \begin{bmatrix} Q & 0 \\ 0 & R \end{bmatrix} \begin{bmatrix} C^{syn} & D^{syn} \\ 0 & I \end{bmatrix} \end{gathered} \tag{3.30}$$

Q and R as used for the lateral directional control law design are shown in Equation 3.31.

$$
\begin{aligned}
Q &= \begin{bmatrix} 1 & 0 \\ 0 & 1 \end{bmatrix} \rho \\
R &= \begin{bmatrix} 1 & 0 \\ 0 & 1 \end{bmatrix}
\end{aligned}
\tag{3.31}
$$

where ρ is a constant factor that is changed from very small to very large until a combination with acceptable gain margins, phase margins, and performance for each of the three configurations is attained. Phase and gain margins are calculated based on the smallest singular values of the closed loop control system, as outlined in [15]. Control law performance and robustness properties are evaluated with a 50 millisecond delay included to take into account the feedback and processing delays.

The output weighting method employed here has the advantage of being able to apply several techniques to shape the variables y^{lqr} by changing the structure of the C^{syn} and D^{syn} matrices. In [13], for example, criterion outputs y^{lqr} are constructed that can be used with frequency weighting methods to add some classical control theory intuition to the process. Similarly in [4], the author uses another dynamic model in the output equation to effectively create zeros in the closed loop transfer function. This is also closely related to the implicit model following techniques presented in [10]. The simplest form of the controller, and that which is used here, simply uses the integrated error between the plant and reference model outputs as the criterion outputs to be used in the quadratic cost function. This is accomplished by using the C^{syn} and D^{syn} matrices given in Equation 3.32.

$$
\begin{aligned}
C^{syn} &= \begin{bmatrix} 0 & 0 & 0 & 1 & 0 & 0 & 0 & 0 \\ 0 & 0 & 0 & 0 & 1 & 0 & 0 & 0 \end{bmatrix} \\
D^{syn} &= \begin{bmatrix} 0 & 0 \\ 0 & 0 \end{bmatrix}
\end{aligned}
\tag{3.32}
$$

Note that the feed forward path gain matrix K_{ff} shown in Figure 3-11 and Equation 3.25 is not computed by the LQR design routine. The feed forward path functions independently of the feedback gains, and has no impact on the closed loop stability of the system. They can be used to tailor the transient response characteristics as necessary to achieve the desired response characteristics, and are used extensively in the application of this type of control law to piloted aircraft to enhance flying qualities criteria. These gains will initially be set to 0 for the design process and if necessary, increased to enhance the transient response of the system to boost tracking performance.

The above control law design technique was carried out on each of the three configurations at a trim airspeed of 6 m/s. The value of ρ was progressively increased until the phase margin drops below 30 degrees or the phase margin drops below 6 dB. The gains for each configuration are shown in Figure 3-13.

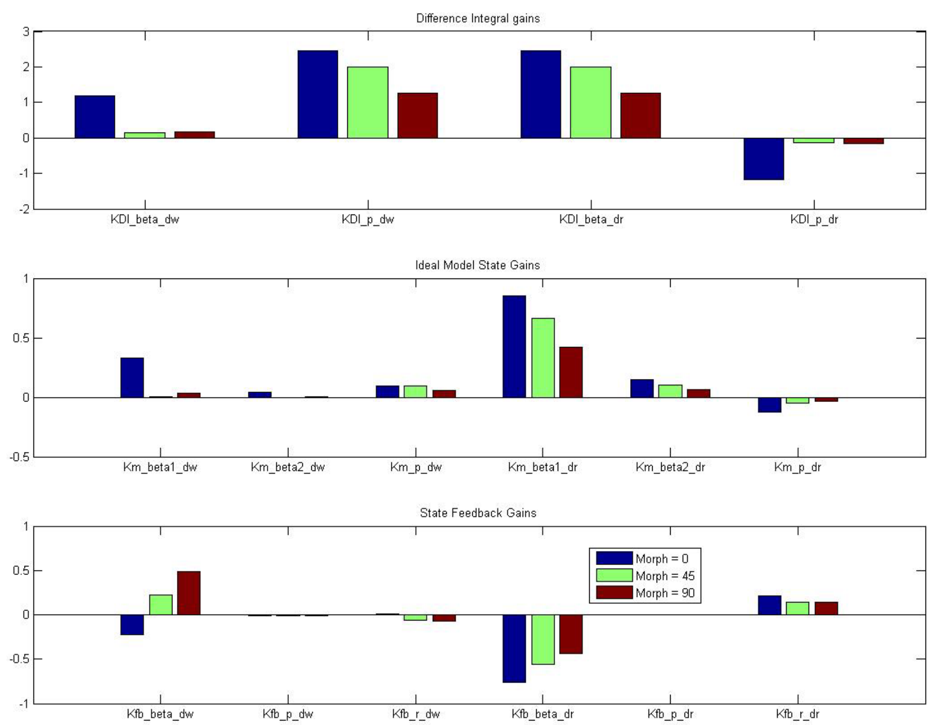

Figure 3-13: Lateral-directional controller gain variation with morph angle

As is often the case with state feedback optimal controllers, there are a large number of gains determined in this routine, 16 in this instance. It can also be seen that the variation from configuration to configuration does not seem to follow a pattern. It is worth noting that in general the gains on the difference integral are the highest and are thus the driver of most of the commands. It can also be seen that in most cases the cross control gains are relatively small, i.e. the gains to wheel input from roll rate error are larger than the gains from roll rate error to rudder, etc.

We begin ascertaining the controller performance by looking at the response of the controllers to an initially non-zero sideslip angle β. We use initial condition response here rather than step response, because in general the controller will be commanding β to zero, so its main function will be disturbance rejection.

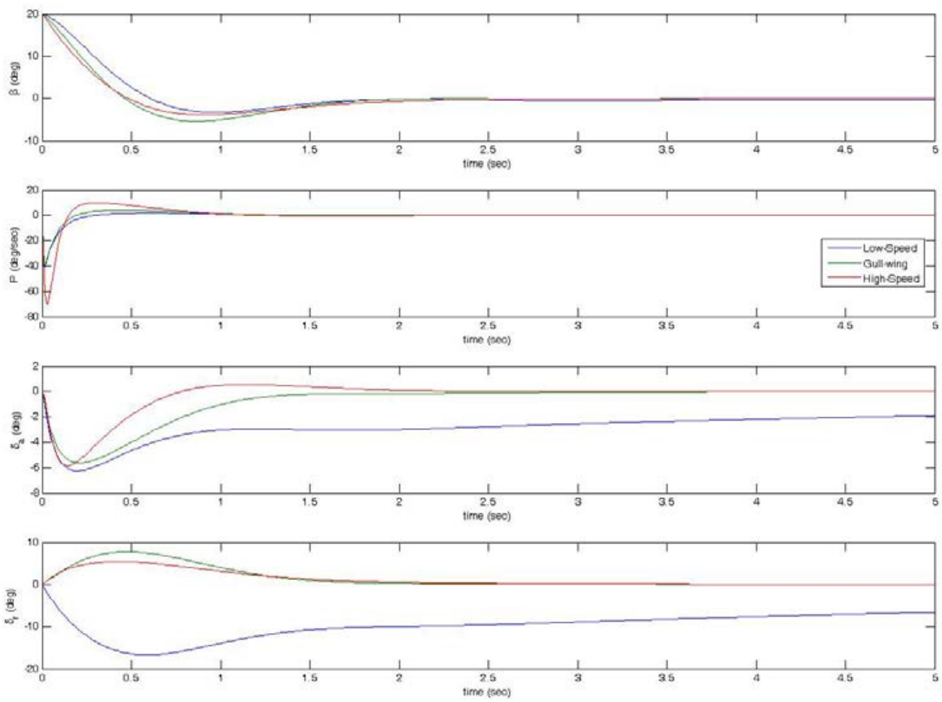

Figure 3-14: Closed loop response to initial non-zero sideslip angle with 50 ms delay included

As seen in the figure, all three controllers do a decent job of returning the system to zero sideslip and zero roll rate. Figure 3-15 shows the step response of all three configurations to a 30 deg/sec roll rate step command.

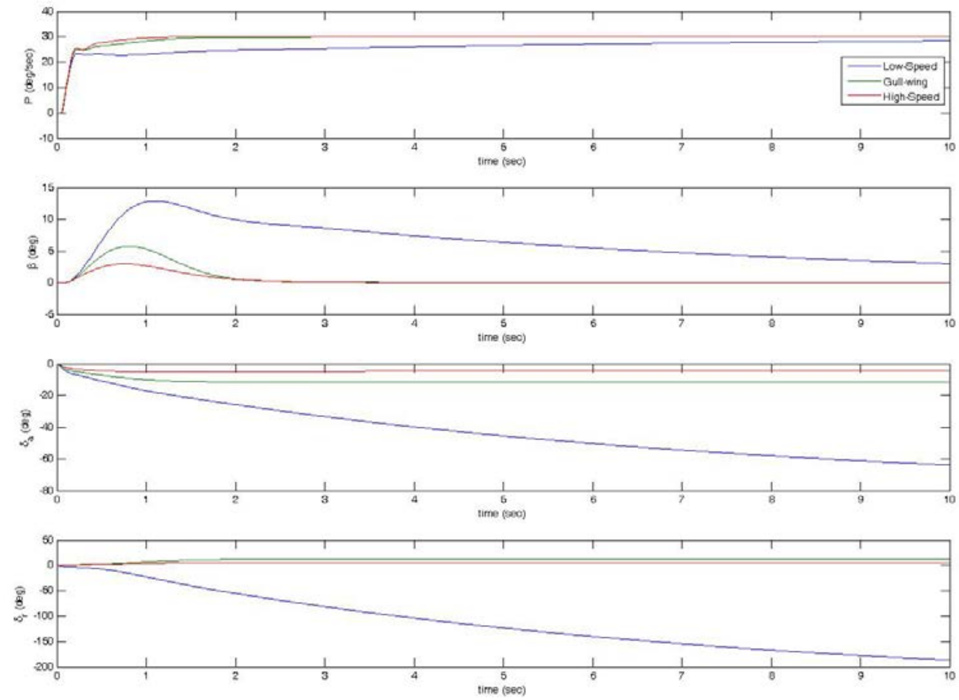

Figure 3-15: Step response to 30deg/sec roll rate command with 50 ms delay included

As can be seen in the figure, this command results in the aileron command growing very large in the low-speed configuration before the roll rate reaches its command. One can also see that in the low speed configuration a large amount of sideslip occurs. The combination of the low-speed configuration's large roll damping, large roll due to sideslip, and very low side force control power results in poor performance. The performance of the gull-wing and high-speed configurations look acceptable and both achieve zero-error within a couple of seconds.

Before giving up on the low-speed configuration, let us look at its performance to a step command in roll angle rather than roll rate when it is integrated with the outer loop control law. Similar to as was done for the longitudinal case, a Simulink simulation of the lateral directional dynamics was built. The simulation issues a roll angle (φ) command and can simulate each of the configurations individually or use a table lookup to dynamically change the plant dynamics. The actuators are limited to +/- 45 degrees and 5 rad/sec.

Figure 3-16 shows the step response of the low speed configuration to a 30 degree φ command.

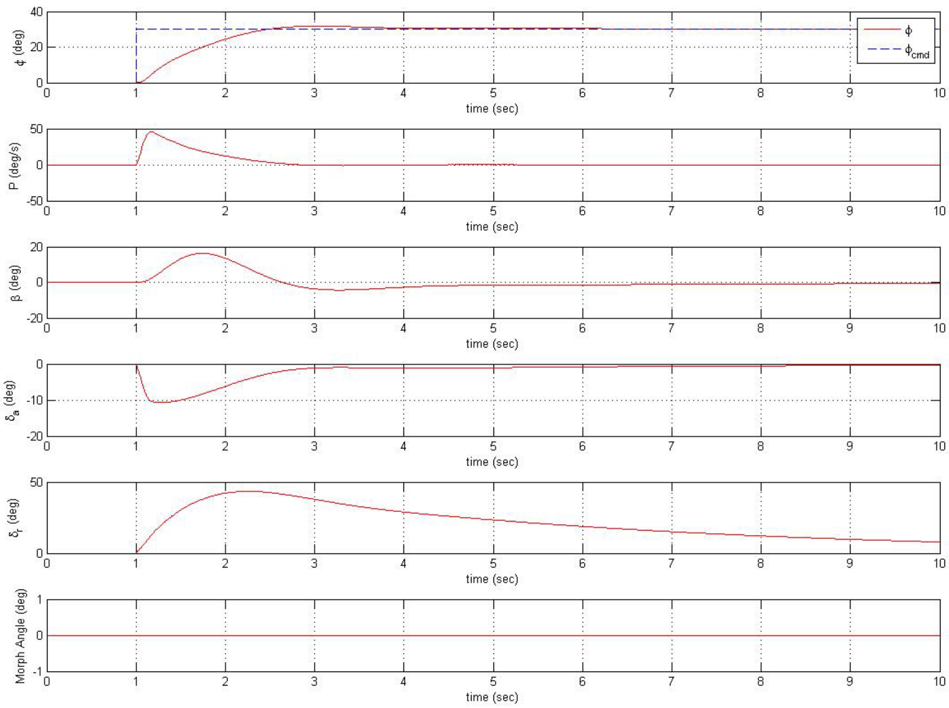

Figure 3-16: Step response of low-speed configuration to 30 degree φ command with 50 ms delay, 5 rad/s actuator rate limit, and +/- 45 degree actuator position limit

As can be seen in the figure, the tracking performance to φ is good. The sideslip does build up as P increases, but then dies back down as the commanded roll angle is achieved. Despite the poor tracking performance to large roll rate commands, the overall goal of the controller is achieved. Figure 3-17 and Figure 3-18 show the same step response for the gull-wing and high-speed configurations respectively.

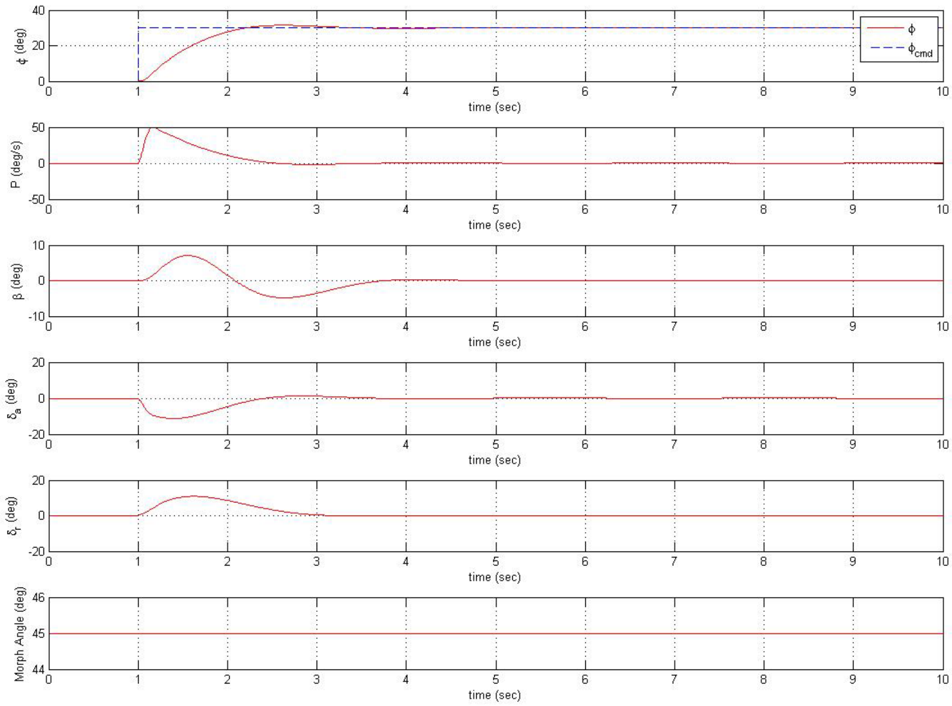

Figure 3-17: Step response of gull-wing configuration to 30 degree φ command with 50 ms delay, 5 rad/s actuator rate limit, and +/- 45 degree actuator position limit

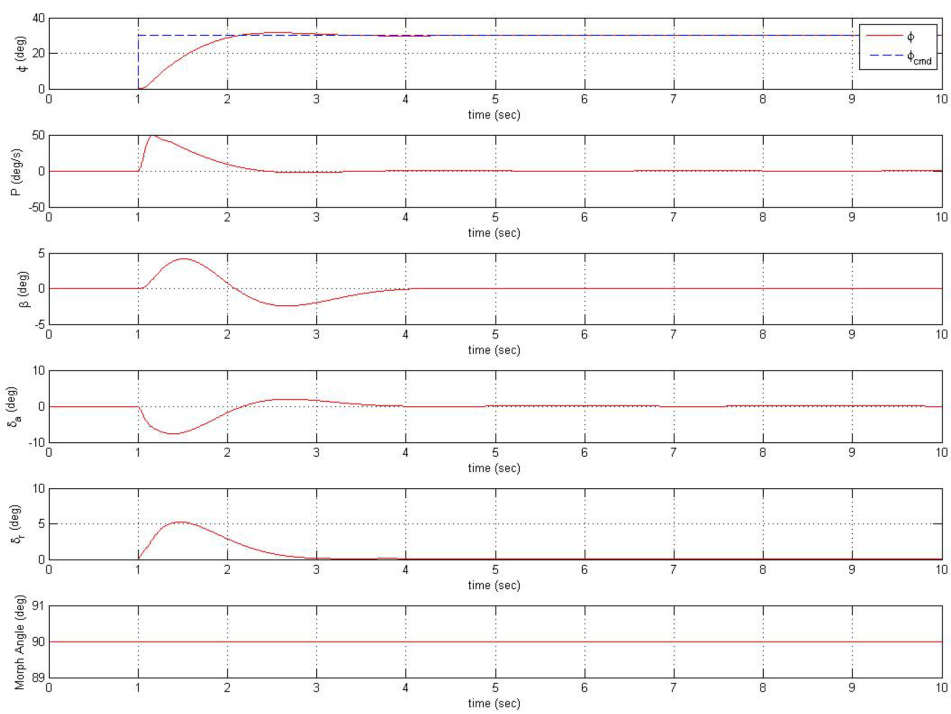

Figure 3-18: Step response of high-speed configuration to 30 degree φ command with 50 ms delay, 5 rad/s actuator rate limit, and +/- 45 degree actuator position limit

Both the gull-wing and high-speed configurations also show adequate roll angle tracking performance.

With the longitudinal controller, it was possible to simply use the gull-wing gains for all configurations. This does not work so well for the lateral directional case. First, let us examine the case where the gull-wing gains are used with the high-speed configuration. This scenario is shown in Figure 3-19.

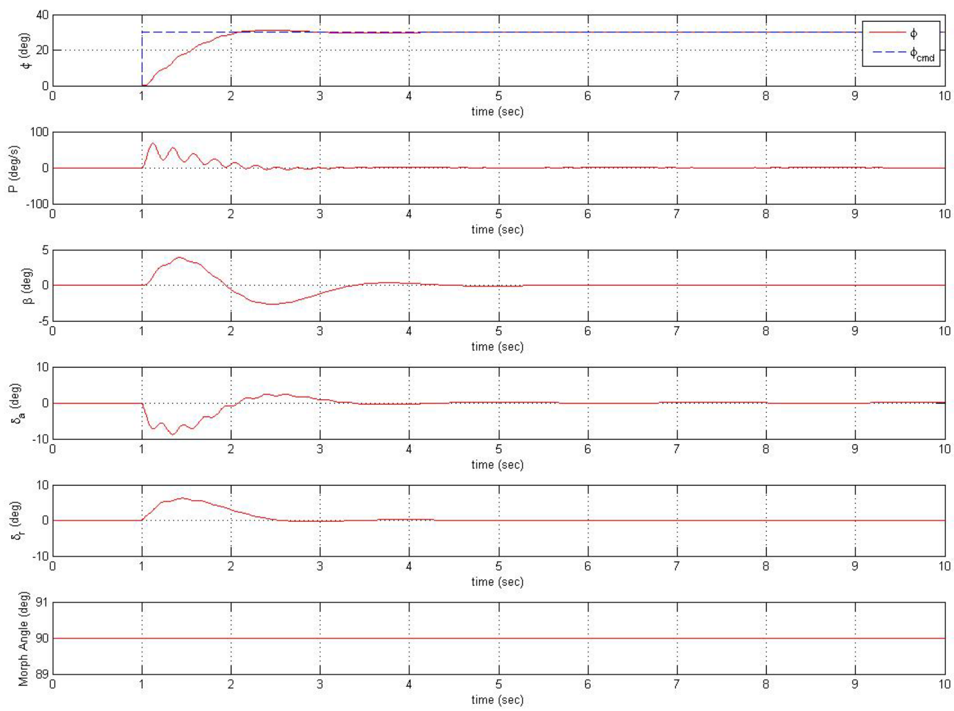

Figure 3-19: Step response of high-speed configuration to 30 degree φ command using gull-wing gains with 50 ms delay, 5 rad/s actuator rate limit, and +/- 45 degree actuator position limit

As can be seen in the figure, the performance with this setup is somewhat reduced from the performance with the specifically designed gains. The commanded bank angle is eventually achieved, but it oscillates around the desired bank a couple of times before settling there. It is also apparent that there are some significant and undesirable oscillations in the roll rate and control surface deflections. Next we consider the opposite case - the gull-wing configuration using the high-speed gains. This situation is shown in Figure 3-20.

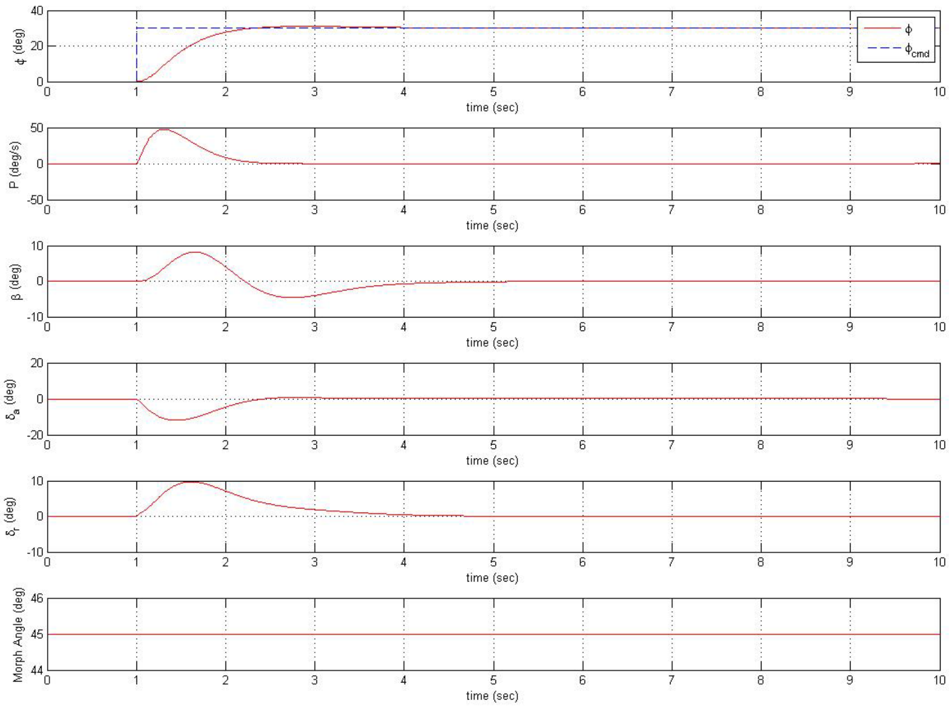

Figure 3-20: Step response of gull-wing configuration to 30 degree φ command using high-speed gains with 50 ms delay, 5 rad/s actuator rate limit, and +/- 45 degree actuator position limit

In comparison to the step response of the gull-wing configuration with its own gains shown in Figure 3-17, the response of Figure 3-20 is very comparable. This implies that the high-speed gains should be an acceptable solution for the gull-wing configuration as well. Figure 3-21 shows the step response of the low-speed configuration using the high speed gains.

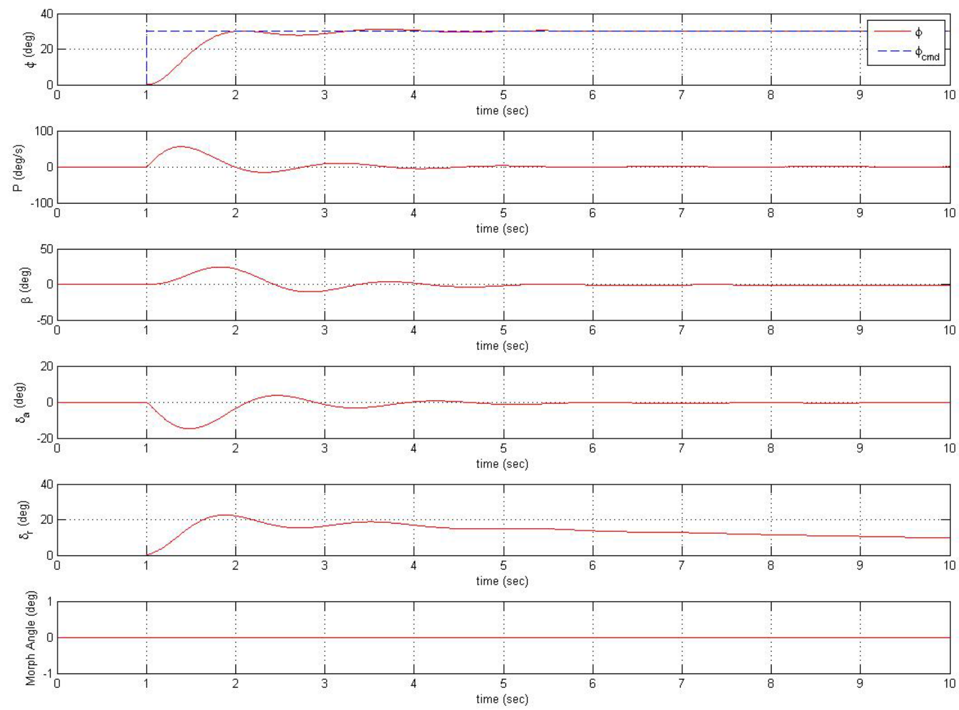

Figure 3-21: Step response of low-speed configuration to 30 degree φ Command using high-speed Gains with 50 ms delay, 5 rad/s actuator rate limit, and +/- 45 degree actuator position limit

Once again the low-speed configuration is the problem; the step command in roll angle results in a slowly decaying oscillation and steadily increasing amounts of rudder deflection. It can also be seen that the sideslip angle is very large early on in the maneuver when the roll rate is high.

It is obvious from the above results that a single set of gains is not going to work in the lateral-directional axis. The approach taken instead, was to implement a gain schedule that changes the gains as a function of the current morph angle. A couple of possibilities exist for the definition of the gain schedule. The most straightforward method will be to simply use a linear interpolation between the gains in one configuration and the gains in the next configuration. The other possibility is to create a gain schedule that follows a more exotic shape such as a spline curve or sigmoid. It is desirable to minimize the number of design points that are used to define the gain schedule to limit complexity and design cycle time. Therefore we start by using only the three design configurations that have already been discussed.

First let us try the simplest approach, which is to simply use a linear interpolation method between the design points. To check the performance of such an approach, the controller performance at off-design morph angles of 60 and 15 degrees was investigated. The step responses of these configurations are shown in Figure 3-22 and Figure 3-23 respectively.

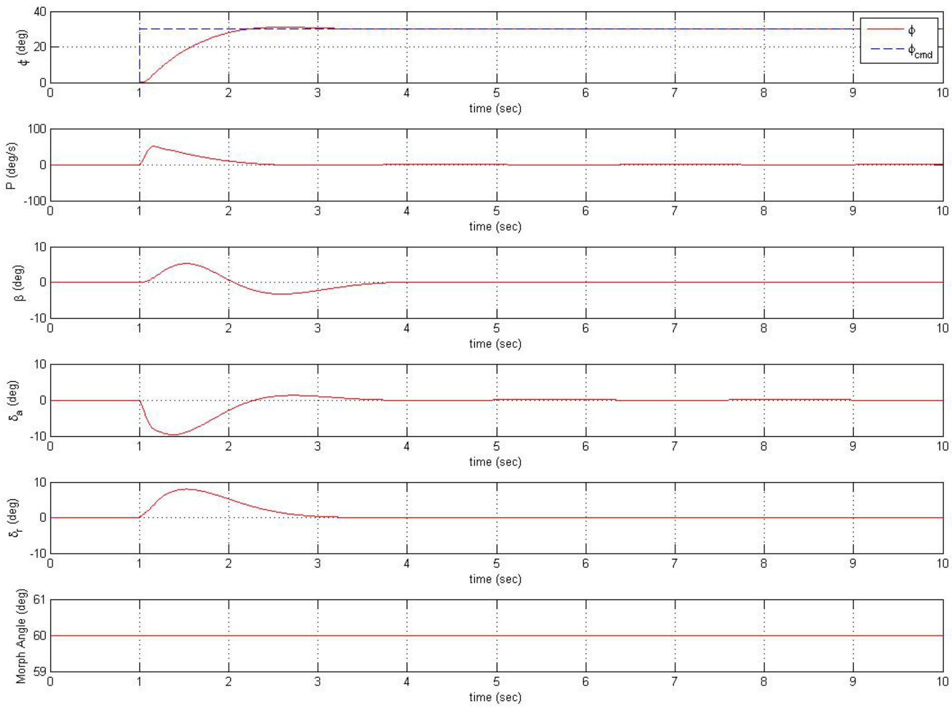

Figure 3-22: Step response of off-design configuration (morph angle = 60 degrees) to 30 degree φ command with linear gain scheduling with 50 ms delay, 5 rad/s actuator rate limit, and +/- 45 degree actuator position limit

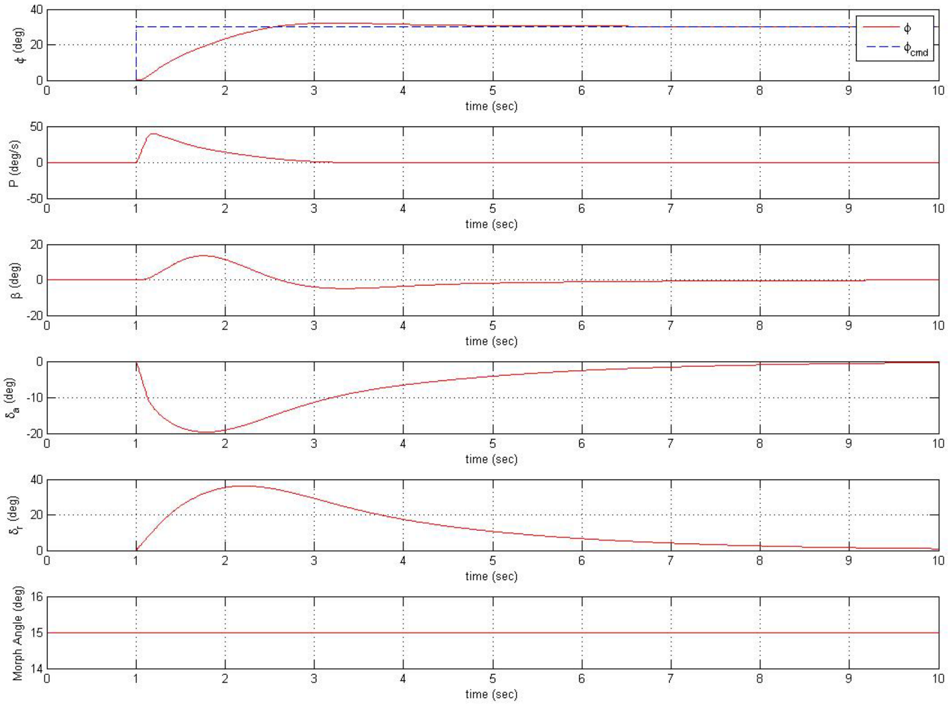

Figure 3-23: Step response of off-design configuration (morph angle = 15 degrees) to 30 degree φ command with linear gain scheduling with 50 ms delay, 5 rad/s actuator rate limit, and +/- 45 degree actuator position limit

These configurations and the linear gain schedule show good performance. The results appear similar to those for the design cases shown above.

The final check of the performance of the control strategy and linear gain scheduling was a simulation in which the plant dynamics continually change from one configuration to the next while trying to track a command. Figure 3-24 shows such a scenario. In this plot, the vehicle is commanded to a series of bank angles while the morphing configuration is changed from configuration to configuration.

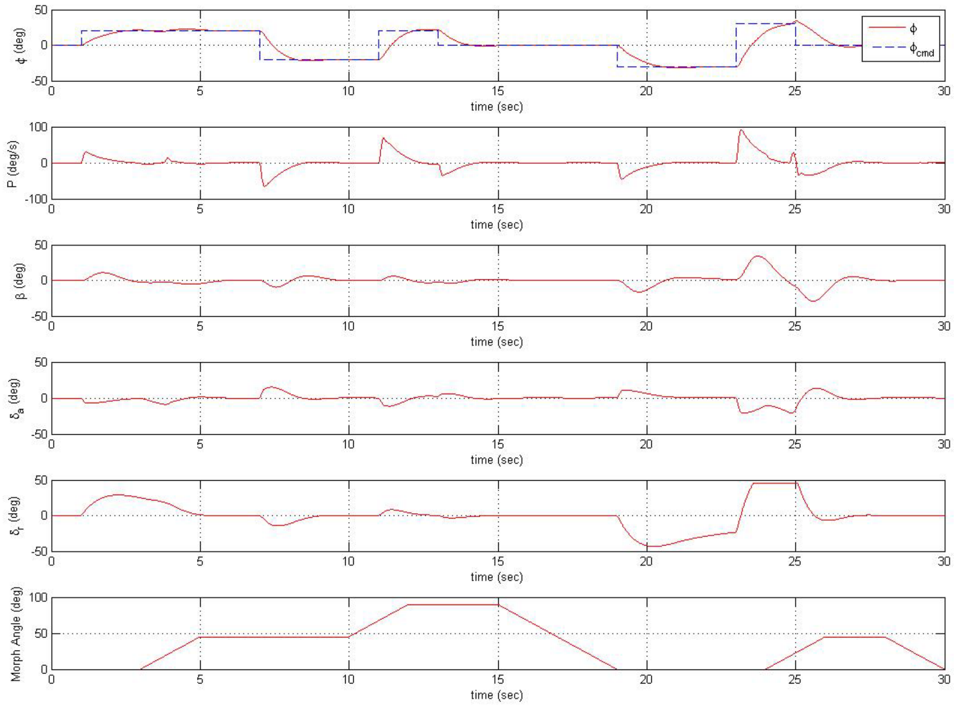

Figure 3-24: Lateral-directional response to 3-2-1 command in bank angle while undergoing configuration changes with 50 ms delay, 5 rad/s actuator rate limit, and +/- 45 degree actuator position limit

Figure 3-24 shows that overall the performance is good. There is a slight bobble during the first transition from low-speed to gull-wing configuration at around the 4 second mark. It is also seen that the step command to go from -30 degrees to 30 degrees while in the low speed configuration near the 23 second mark results in a large amount of sideslip and full rudder. This confirms our intuition from inspection of the dynamics that the low-speed configuration is not the best suited configuration for aggressive maneuvering.

The combination of the linear gain scheduling and the control surface mixing scheme described in Chapter 2, work together well to achieve the desired performance in the simulation studies. It is important to remember that the simulations used here represent linear and steady aerodynamic models created with the vortex lattice code. In the presence of nonlinear effects from “fast” configuration changes due to unmodeled aerodynamic effects or inertial effects, the performance of the controller may degrade.

Model Reference Adaptive Control (MRAC)

This section briefly discuses the development of a model reference adaptive controller to maintain system stability and performance during configuration changes in the face of unmodeled nonlinear and unsteady effects. First the theory is reviewed followed by its application to the longitudinal dynamics. The pitch dynamics were chosen because the modeled nonlinearity has a more straight forward effect on the longitudinal motion, but the same theory could also be applied to the lateral-directional dynamics.

The approach taken here was to use the adaptive control law as augmentation of the baseline controller described previously. This means that if the model is perfectly known and there are no nonlinear effects, the adaptive control contribution will be zero. To check the performance of the controller, a simple model of one possible unsteady effect of "fast morphing" is introduced and implemented in the simulation. The form of the controller and the theoretical discussion that follows is taken from [16]. More information and background information on MRAC control and adaptive control in general can be found in [17] and [18]. Figure 3-25 shows the basic form of this arrangement.

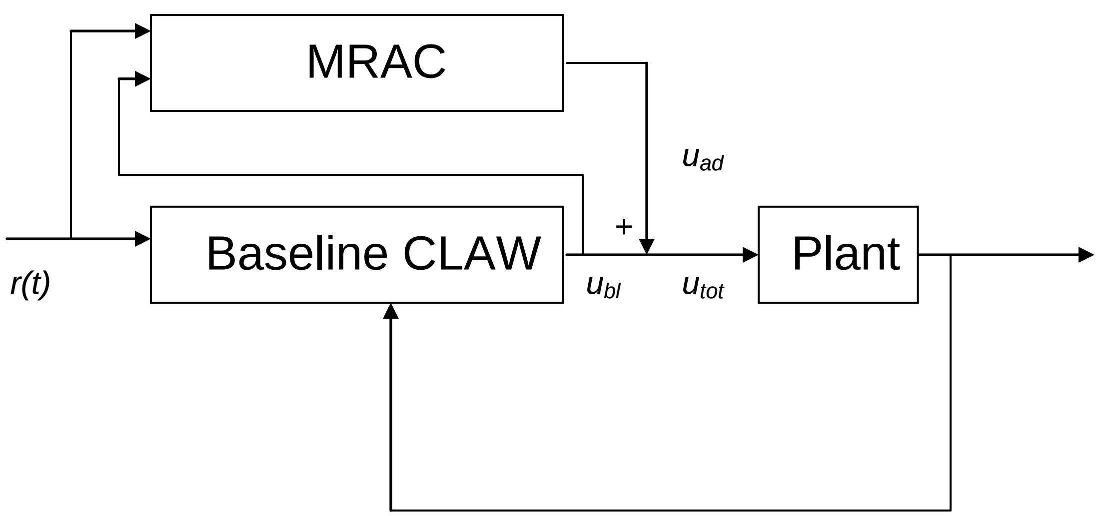

Figure 3-25: Augmentation of Baseline Controller with Model Reference Adaptive Control (MRAC)

We start by formulating the control problem. Consider a class of uncertain MIMO systems with matched nonlinear uncertainty *d(x)* given in the form of Equation 3.33.

$$\dot{x}_p = A_p x_p + B_p \Lambda \left(u + \overbrace{\Theta_d^T \Phi_d(x_p)}^{d(x_p)} \right) \tag{3.33}$$

Where $A_p \in R^{nxn}$ is unknown, $B_p \in R^{nxm}$ is known, $\Lambda = diag\{\lambda_i\}$ with λ_i unknown, but $sign(\lambda_i)$ known represents control input effectiveness variation, and *d(x)* is represented as a linear combination of *N* known basis functions Φ with unknown constant coefficients Θ. The control goal is asymptotic tracking of the performance output to the reference input $r(t) \in R^m$ in the presence of the uncertainties. So we must find *u* such that the performance output $y \in R^m$ given in Equation 3.34

$$y = C_p x_p + D_p \Lambda \left(u + d(x_p) \right) \tag{3.34}$$

asymptotically tracks *r(t)*. The baseline PI controller described above achieves this goal in the case of no uncertainty, i.e. $\Lambda = I_{mxm}$ and $\Theta = 0_{Nxm}$. Adding the baseline controller dynamics to Equation 3.33 yields the system dynamics shown in Equation 3.35.

$$\dot{x} = \tilde{A}\tilde{x} + \tilde{B}\Lambda \left(u + \Theta_d^T \Phi_d(x) \right) + \tilde{G}r \tag{3.35}$$

The baseline control law has the form $ubl = -\tilde{K}\tilde{x}$ as described previously, where $\tilde{x}$ includes the plant dynamic states, and the difference integral state of the compensator as shown in Equation 3.15.

To begin the formulation of the MRAC controller, we first define a reference model. We will choose the reference model here to be the closed loop system formed by the plant dynamics and the baseline controller. This results in a model of the form of Equation 3.36.

$$\begin{aligned} \dot{x}_{ref} &= A_{ref} x_{ref} + \tilde{G} r \\ y_{ref} &= C_{ref} x_{ref} \end{aligned} \tag{3.36}$$

Where

$$\begin{aligned} A_{ref} &= \tilde{A} - \tilde{B}\tilde{K} \\ C_{ref} &= I_{nxn} \end{aligned} \tag{3.37}$$

with $\tilde{G}$ from Equation 3.15 and A_{ref} is Hurwitz by design. The model matching conditions for applicability of this technique require that ideal gains K_x and K_r exist such that:

$$\begin{aligned} A + B\Lambda K_x^T &= A_m \\ B\Lambda K_r^T &= B_m \end{aligned} \tag{3.38}$$

However, the ideal gains need not be known.

The total control input is the sum of the baseline control input and the control input from the adaptive controller.

$$u_{tot} = -\tilde{K}\tilde{x} + u_{ad} \tag{3.39}$$

Next we substitute 3.39 into 3.33 and do some algebra using the model matching conditions.

$$\dot{x} = \tilde{A}\tilde{x} + \tilde{B}\Lambda\left((u_{ad} + u_{bl}) + \Theta_d^T \Phi_d(x)\right) + \tilde{G}r$$

$$\downarrow$$

$$\dot{x} = A_{ref}\tilde{x} + \tilde{B}\Lambda\left(u_{ad} + \begin{bmatrix}\Lambda^{-1} & K_x^T & \Theta_d^T\end{bmatrix}\begin{pmatrix}u_{bl} \\ -x \\ \Phi_d(x)\end{pmatrix}\right) + \tilde{G}r \tag{3.40}$$

$$\downarrow$$

$$\dot{x} = A_{ref}\tilde{x} + \tilde{B}\Lambda\left(u_{ad} + \overline{\Theta}^T\overline{\Phi}(u_{bl}, x)\right) + \tilde{G}r$$

With the redefined regressor vector $\overline{\Phi}(u_{bl}, x)$ and unknown/ideal parameters $\overline{\Theta}$ given by Equation 3.41.

$$\begin{aligned}\overline{\Phi}(u_{bl}, x) &= \begin{bmatrix}u_{bl} & -x & \Phi_d(x)\end{bmatrix}^T \\ \overline{\Theta} &= \begin{bmatrix}K_u^T & K_x^T & \Theta_d^T\end{bmatrix}^T\end{aligned} \tag{3.41}$$

The adaptive control is then chosen such that it negates the matched uncertainty $\overline{\Theta}^T\overline{\Phi}(u_{bl}, x)$ as shown in Equation 3.42.

$$u_{ad} = -\hat{\overline{\Theta}}^T\overline{\Phi}(u_{bl}, x) \tag{3.42}$$

Where $\hat{\overline{\Theta}} \in R^{(n+N+m)xm}$ is the matrix of adaptive parameters. Substituting Equation 3.42 into the final form of 3.40 gives Equation 3.43.

$$\dot{x} = A_{ref}\tilde{x} - \tilde{B}\Lambda\underbrace{\left(\hat{\overline{\Theta}} - \overline{\Theta}\right)^T}_{\Delta\overline{\Theta}} + \tilde{G}r \tag{3.43}$$

We then define the tracking error as $e = x - x_{ref}$ then the tracking error dynamics can be calculated by subtracting the reference dynamics in Equation 3.36 from the system dynamics in Equation 3.43 gives:

$$\dot{e} = A_{ref} e - B_{syn} \Lambda \Delta \overline{\Theta}^T \overline{\Phi} \tag{3.44}$$

We will now use Lyapunov arguments to design an adaptation law to determine the values of $\hat{\overline{\Theta}}$ that ensure that *e* asymptotically goes to zero. Consider the candidate Lyapunov function of Equation 3.45.

$$V(e, \Delta\overline{\Theta}) = e^T P_{ref} e + trace(\Delta\Theta^T \Gamma_{\overline{\Theta}}^{-1} \Delta\dot{\hat{\overline{\Theta}}} \Lambda) \tag{3.45}$$

In Equation 3.45, $\Gamma_{\overline{\Theta}} = \Gamma_{\overline{\Theta}}^T > 0$ is the symmetric positive definite constant matrix of adaptation rates and $P_{ref} = P_{ref}^T > 0$ is the unique symmetric positive definite solution to the algebraic Lyapunov equation 3.46.

$$A^T P_{ref} + P_{ref} A = -Q_{ref} \tag{3.46}$$

Where $Q_{ref} = Q_{ref}^T > 0$ is symmetric and positive definite. We now take the time derivative of 3.45 along the state trajectories of 3.44 and apply the trace identity $a^T b = trace(ba^T)$.

$$\dot{V} = -e^T Q_{ref} e + 2trace\left(\Delta\overline{\Theta}^T \left\{ \Gamma_{\overline{\Theta}}^{-1} \dot{\hat{\overline{\Theta}}} - \overline{\Phi} e^T P_{ref} \tilde{B} \right\} \Lambda \right) \tag{3.47}$$

We will select adaptation laws as shown in Equation 3.48.

$$\dot{\hat{\overline{\Theta}}} = \Gamma_{\Theta} \overline{\Phi}(u_{bl}, x) e^T P_{ref} \tilde{B} \tag{3.48}$$

Then Equation 3.47 reduces to:

$$\dot{V} = -e^T Q_{ref} e \le 0 \tag{3.49}$$

Which proves ultimate boundedness of the error e and $\Delta\overline{\Theta}$. Through extension of this argument to the boundedness of the state vectors and regressor components and Barbalat's Lemma it can be proven that in fact the error is not only bounded, but also asymptotically goes to zero. See [17] for details.

The adaptation law of Equation 3.48 can be broken into component parts.

$$\begin{aligned}
\dot{\hat{K}}_u &= \Gamma_u u_{bl} e^T P_{ref} \tilde{B} \\
\dot{\hat{K}}_x &= -\Gamma_x x e^T P_{ref} \tilde{B} \\
\dot{\hat{\Theta}} &= \Gamma_\Theta \Phi(x) e^T P_{ref} \tilde{B}
\end{aligned} \tag{3.50}$$

The total control input can now be written as,

$$u = u_{bl} + u_{ad} = -\tilde{K}\tilde{x} + [-\hat{K}_u^T u_{bl} - \hat{K}_x^T x - \hat{\Theta}^T \Phi(x)] \tag{3.51}$$

In the preceding discussion, Φ is a known set of basis functions that are used to estimate parametric unmodeled dynamics in the system. The basis functions can be a wide variety of functions (as long as they are continuous) and any desired number can be used. In general a set of basis functions is chosen that can approximate a large class of different functions, such as a Fourier series or a set of polynomial functions. Other techniques include artificial neural networks comprised of sigmoids or radial basis functions [17].

It is important to incorporate as much physical knowledge of the system and the possible unmodeled dynamics as possible into selecting the basis functions. Here for example, it is clear that the nonlinearities and unsteady effects are related to the morph angle and the morph angle rate, as such it would make sense to use those as the independent variable for the basis functions chosen. That is, $\Phi = \Phi(\mu, \dot{\mu})$. It should be noted that this differs slightly from what is shown in the preceding derivation, namely, that μ and $\dot{\mu}$ are not explicitly state variables used in the design of the control, and thus are not included in the plant dynamics equations. It is known, however, that their values are bounded and continuous, so using them in the basis functions do not change the stability arguments above.

In order to investigate the efficacy of this particular control law structure, the simulation dynamics should include some uncertainty and/or nonlinear effects. The vortex lattice code cannot give accurate representations of the nonlinear aerodynamics so next an approximation of one possible unsteady nonlinear effect caused by the morphing motion on the pitch dynamics was developed. Figure 3-26 shows a cartoon of wing motion during morphing configuration changes.

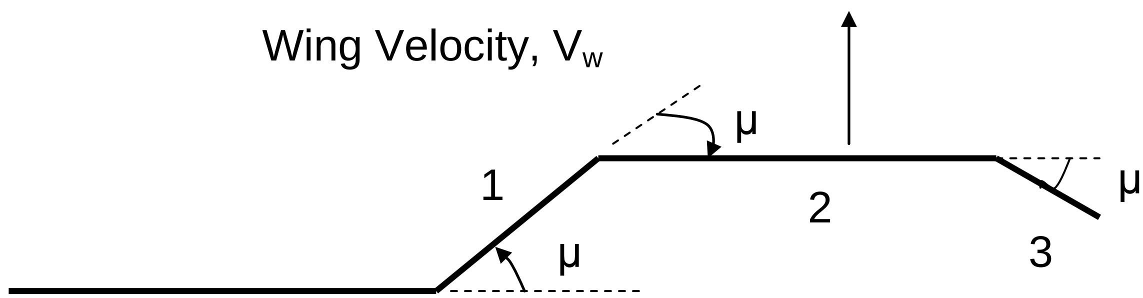

(a)

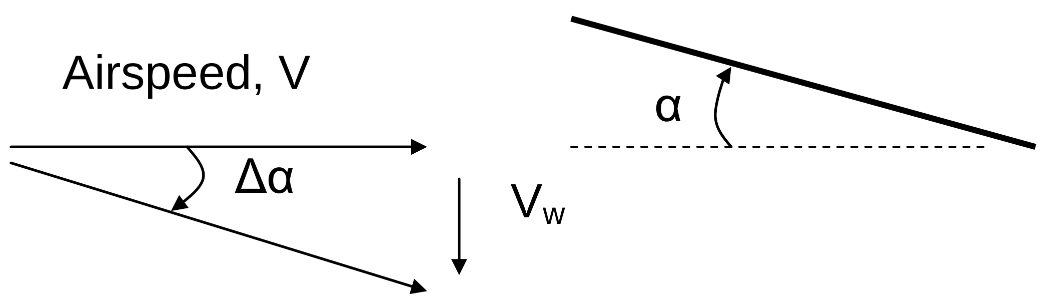

(b)

Figure 3-26: Cartoon of wing motion during morphing (a) front-view (b) side-view

The figure shows that the effect on the airframe caused by morphing is similar to an angle of attack change that is related to the vertical speed of the wing. By examining the figure, it can be seen that the change in angle of attack is given by:

$$\Delta\alpha = \tan^{-1}\left(\frac{V_w}{V}\right) \tag{3.52}$$

We can also derive an expression for the vertical velocity of the individual wing sections. Starting with the inboard section, the surface follows a circular arc around the hinge point, this means that the tangential velocity of any point *p* at a distance *r* from the hinge is given by $V_{t,p} = r\dot{\mu}$ where $\dot{\mu}$ is the angular rate of morphing. Only the vertical velocity is important. This can be represented by Equation 3.53.

$$V_{w,p} = r\dot{\mu}\cos\mu \tag{3.53}$$

This can be plugged into Equation 3.52 to find the angle of attack change at each point *p*. In reality, the change in angle of attack at each point on the wing will be slightly different and thus the lift change will be slightly different. Since this is just an approximation it was assumed that there is a value of $\Delta\alpha$ that can be used over the entire wing that effectively represents the physical phenomenon, and the final change in alpha for section 1 was taken as:

$$\Delta\alpha_1 = C\tan^{-1}\left(\frac{\dot{\mu}\, r_{avg}\cos\mu}{V}\right) \tag{3.54}$$

Where *C* is a constant and r_{avg} is the midspan of the wing section. This derivation can be carried over to the remaining wing sections resulting in similar expressions. Since this is just an approximation, Equation 3.54 was used for the effect airplane wide with r_{avg} set to the quarter span, and the effects of changing the value of *C* on the results was investigated. Figure 3-27 shows the effect of the value of *C* on the nonlinearity.

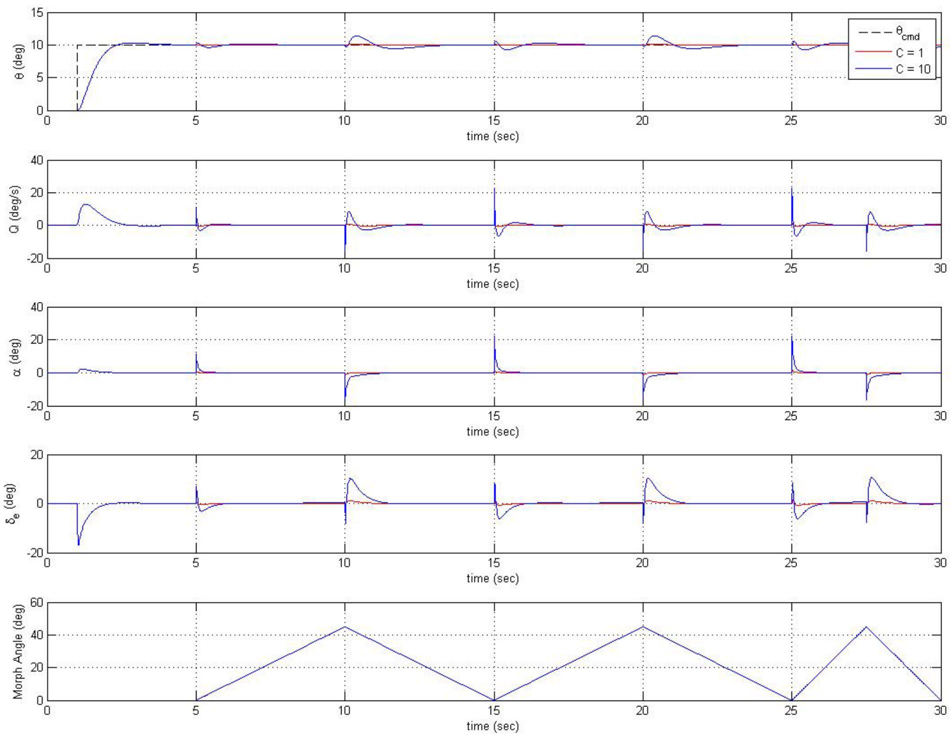

Figure 3-27: Nonlinearity effect on dynamics with varying values of the constant *C*

Figure 3-27 shows that the effect is very small with *C =1*, but can be made substantial by setting *C = 10*, which is the value that was used for the rest of the investigation. It is clear from Equation 3.54 and Figure 3-26 and Figure 3-27 that the magnitude of the angle of attack change is greatly influenced by the rate of morphing relative to the free stream velocity. Faster angular rates result in a greater α disturbance. In addition, the effect is the largest at morph angles near the low-speed configuration as the majority of the angular motion is in the vertical direction.

Equation 3.54 can also be used as the form of the basis function Φ in the adaptive control law. The unknown parameter coefficient Θ then, will represent the unknown value of *C* and $\hat{\Theta}$ will be the estimate of *C* determined by the adaptive control law.

$$\Phi(\mu, \dot{\mu}) = \tan^{-1}\left(\frac{\dot{\mu}\, r_{avg} \cos \mu}{V}\right) \tag{3.55}$$
$$\hat{\Theta} \approx \Theta = C$$

This is straightforward to implement when designing a controller based purely on a simulated nonlinearity that is known and explicitly defined. In practice, a larger set of basis functions would be used to try to capture the nonlinearity described above as well as any other nonlinearities. Since the goal here was demonstrate the concept of adaptive control as it applies to morphing, the basis function in Equation 3.55 was used.

Under certain conditions on the command signals (persistent excitation) and the nature of the nonlinearity it can be shown that $\hat{\Theta}$ will go to the correct value of Θ [17], however, this is not required for acceptable tracking performance. It is important to note also that in the presence of nonlinearities and non-parametric uncertainties such as system time delays and disturbances, the mismatch between the actual values of the parameter and the estimates can lead to problems such as parameter drift. This is dealt with in practice by the application of the dead zone modification [17], which stops parameter adaptation when the error between the real system and the ideal model is small.

As can be seen from the derivation above, implementation of an MRAC controller involves picking a large number of gains, weighting matrices, and dead zone parameters. There are very few set in stone methods for successfully selecting all of the variables required. After some experimentation with the simulation the following values of the free parameters were used.

$$
\begin{aligned}
Q &= \begin{bmatrix} 1 & 0 & 0 \\ 0 & 1 & 0 \\ 0 & 0 & 0.1 \end{bmatrix} \\
\Gamma_x &= \begin{bmatrix} 1 & 0 & 0 \\ 0 & 1 & 0 \\ 0 & 0 & 0 \end{bmatrix} \\
\Gamma_\Theta &= 1 \\
\Gamma_u &= 1
\end{aligned}
\tag{3.56}
$$

Figure 3-28 shows a simulation of the baseline controller with no MRAC and the baseline controller with MRAC augmentation.

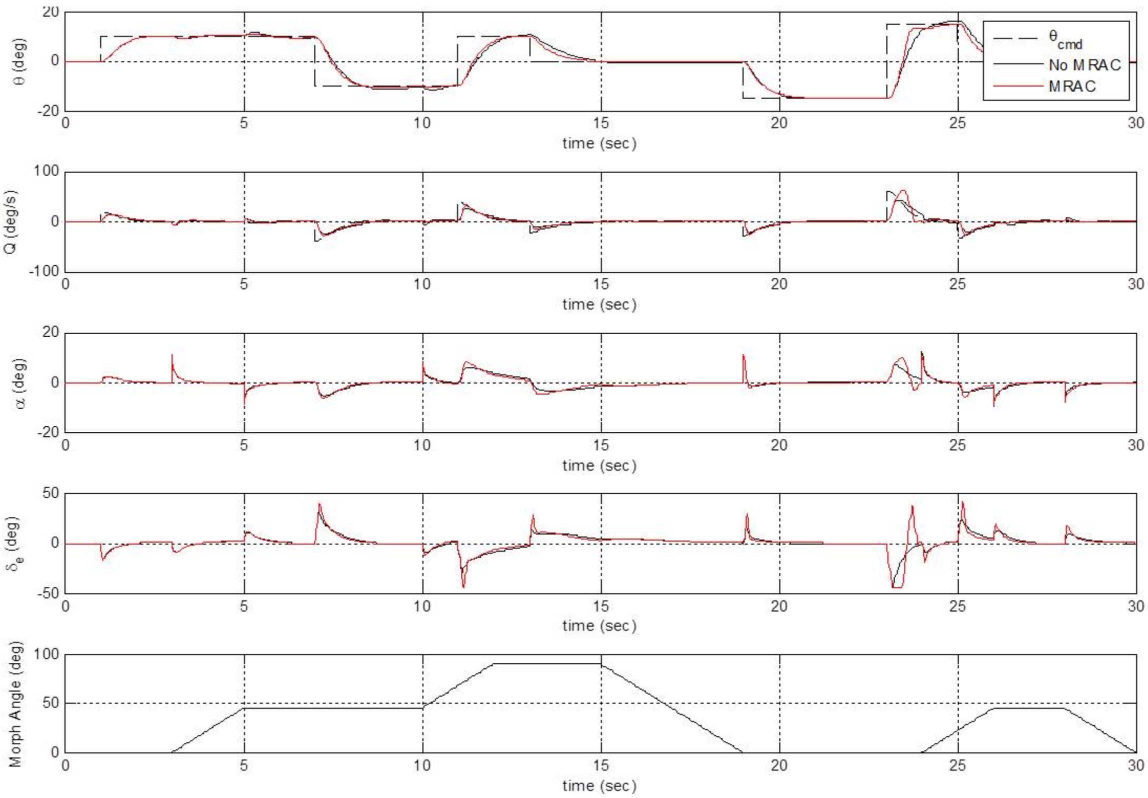

Figure 3-28: Comparison of longitudinal response with MRAC and without MRAC. Includes 50ms time delay, 5 rad/sec actuator rate limit, 30 degree actuator throw limit and nonlinearity with C = 10

As the figure shows, only a small performance improvement is achieved using the MRAC augmented controller. In some cases the response is somewhat faster and shows less overshoot, but the differences are slight. Overall, the MRAC controller achieves a 10% reduction in total error to the pitch rate command in relation to the baseline controller with no MRAC.

One reason for the only small gain in performance is the short term nature of the nonlinearity as modeled here. The nonlinear effect is only present while the configuration change is occurring. This means that the adaptive law readjusts $\hat{\Theta}$ while there is no morphing occurring and there is no nonlinearity back towards its baseline value. This can be seen in Figure 3-29. In the times when the configuration is changing and the nonlinear effect is present, $\hat{\Theta}$ increases rapidly to compensate. When the configuration is constant, it slowly moves back towards zero.

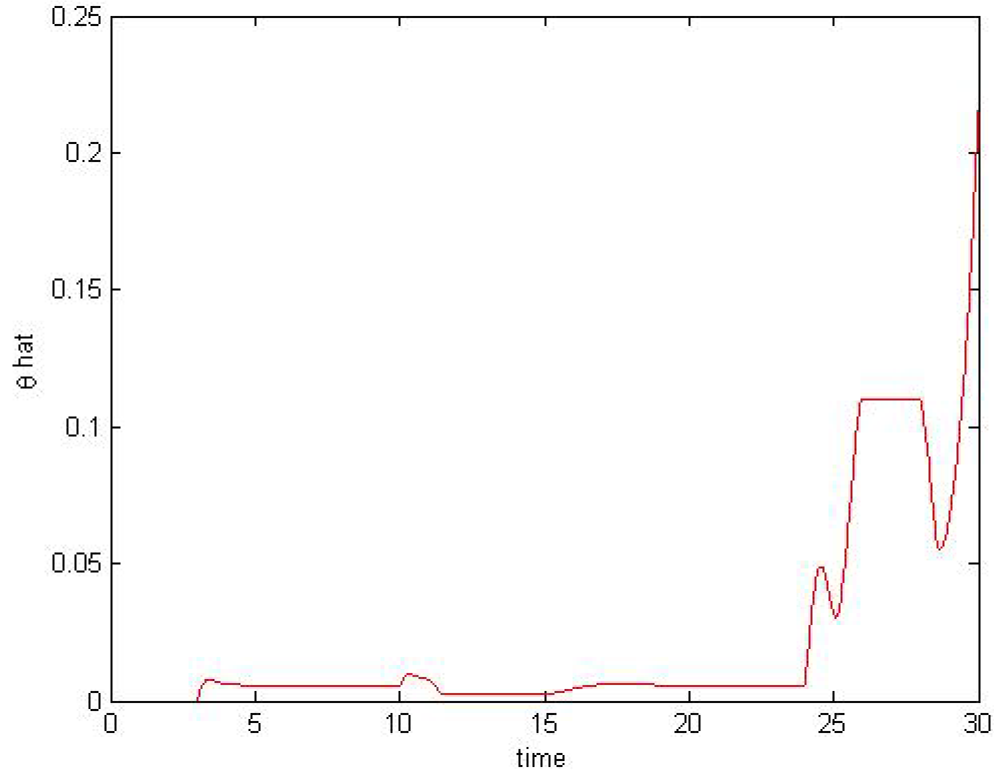

Figure 3-29: Change in $\hat{\Theta}$ during simulation run shown in Figure 3-28

A possible solution to this could be to use an adaptive control technique known as concurrent learning. The idea behind concurrent learning is that the controller retains useful knowledge of where it has been in the state space and the values of the gains that worked well, so that when it returns to that point, it effectively remembers what worked well, see for example [24]. This would be a good direction to explore in the future.

Another issue that limits the performance achieved is the robustness of the controller to actuator rate and position saturation. With a very small increase in the gains used, the controller saturates the actuators and quickly becomes unstable as shown in Figure 3-30.

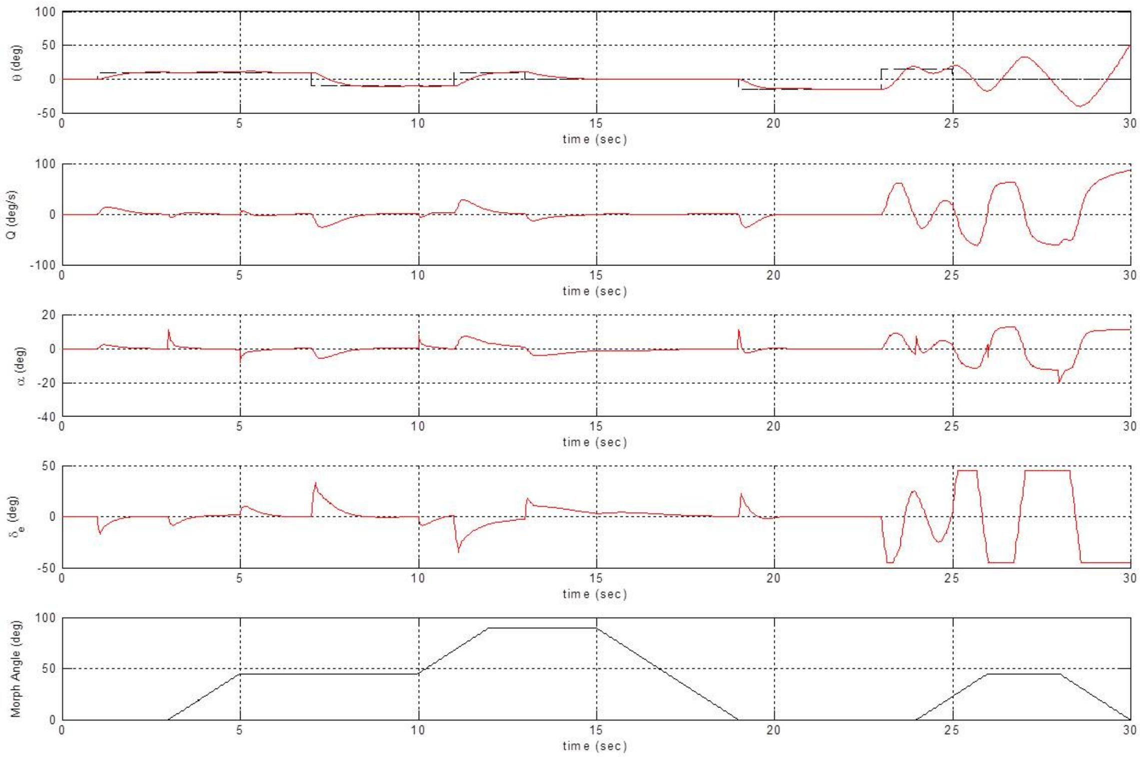

Figure 3-30: Instability of MRAC controller when faced with actuator rate and position saturation

It can be seen that with these higher gains, the performance of the controller is quite good, until the actuators saturate and drive the system unstable. Another future direction then, would be to explore implementing the positive μ-modification which adds stability in the face of saturation [25].

Adaptive control methods show promising results in accounting for the nonlinear effects associated with morphing, however, further work is needed to overcome the issues mentioned here in order to obtain the best performance.

Chapter 4- Flight Test

In this section we will discuss a series of flight tests performed in the Boeing Vehicle Swarm Technology Lab in Seattle, WA. Testing consisted of autonomous powered flight in static configurations representative of the design configurations described earlier. This section will begin with a discussion of the lab facility and the flight test vehicles then continue on to discuss the preliminary results and possible future directions to take to continue the practical application of the theory already presented.

Test Facility

The Boeing Vehicle Swarm Technology Lab (VSTL) is an indoor flight test environment that provides cost-effective rapid prototyping capability for the integration and testing of autonomous vehicle systems [22]. This includes health-monitoring enabled adaptive collaboration algorithms, cooperative path planning, collision avoidance, flight in the presence of gusts, formation flight, and many other past and future projects. The lab can support up to 20 heterogeneous vehicles simultaneously. Vehicle types include fixed wing aircraft, rotorcraft, ground robots, and wall climbing robots. Figure 4-1 shows a photograph of the facility.

Figure 4-1: Boeing VSTL [22]

The lab features a 100'x 50'x 20' flight area and a VICON vision-based motion capture system [23]. The VICON system consists of high resolution digital cameras that triangulate the location of reflective markers placed on each vehicle that reflect light from the camera's LED strobe ring. The result is high rate, high resolution position and attitude information with sub-millimeter position accuracy and sub degree angular accuracy. Data is provided at 100 Hz, with approximately 10ms latency.

In the application presented here, all guidance, navigation, and control processing is performed off-board the vehicle on a PC. The VICON system provides the required data on vehicle position, attitude, and velocity and control laws implemented in C perform the requisite calculations and issue control surface and throttle commands to the vehicle via 802.11 wireless radio transmission. The vehicle is equipped with a digital processor board with custom software that receives the commands and issues the proper outputs to control standard servos and speed controllers like those used in hobby type radio-controlled (R/C) vehicles. Currently, the digital board is capable of commanding 4 individual channels, with capability in development to accommodate up to 8 channels. For this project, the limitation means that for the moment, it is not possible to easily implement the control mixing for the low-speed configuration due to a lack of available channels.

Test Vehicles

As described in Chapter 2, the vehicles were assembled from Depron foam. In addition, carbon spars and fiberglass reinforced tape were used where further stiffness was necessary. The propulsion system consists of a brushless motor made by AXI, a Jeti electronic speed control, and a 3 cell lithium polymer battery pack. The servos used are Hitec HS-503s; one for each control surface. The vehicles are also equipped with a set of landing gear from an R/C model kit.

Two of the three configurations were built and flown. The most successful configuration thus far has been the high-speed configuration. The completed high-speed flight test vehicle is shown in Figure 4-2. The complete flight weight for the high-speed configuration was around 350 grams, and the gull-wing configuration was approximately

330 grams. These weights are somewhat higher than the estimated design weights from Chapter 2, but a quick run through the VLM code confirmed that the vehicles were still flyable at these weights.

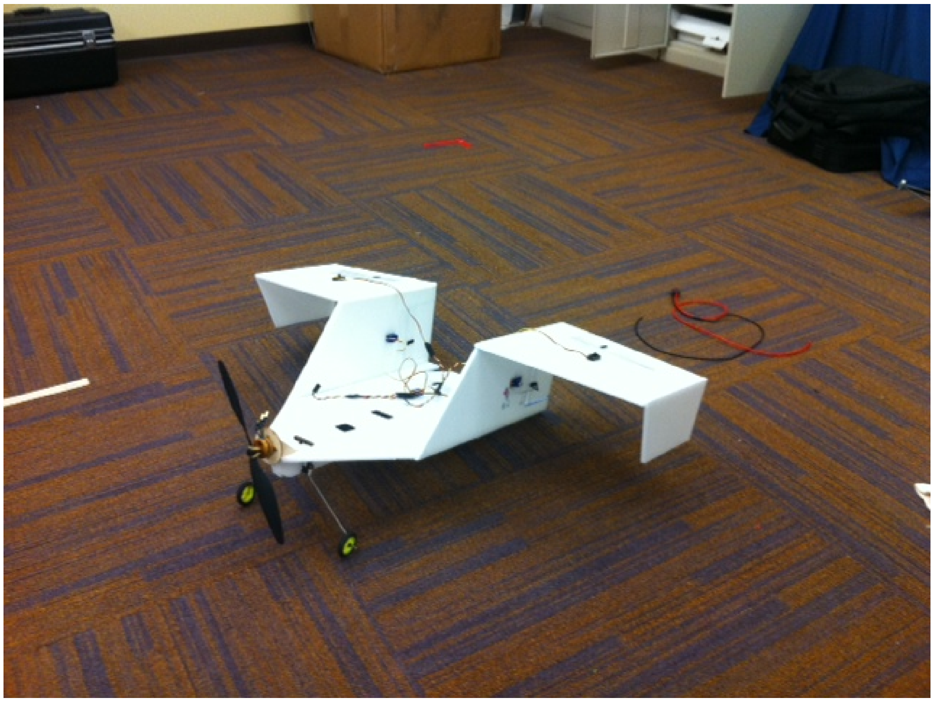

Figure 4-2: High-speed flight test vehicle

Results

Approximately 40 flights with the high-speed configuration and 20 flights with the gull-wing configuration were completed over the course of 5 days in the VSTL. First ground runs were performed to verify proper integration with the lab systems followed by straight leg flights and finally turning flight.

High-Speed Configuration

The first configuration chosen for flight test was the high-speed configuration. This choice was made because it is the most "conventional" configuration of the three in terms of its lateral-directional control surface layout. Initial flight consisted of straight leg segments with the elevator deflection fixed trailing edge up and slow increases in the commanded speed. After a few runs the vehicle was able to successfully skim along the ground and do a fairly consistent job of tracking to the command straight flight path. Figure 4-3 shows flight data for an example of one of these ground runs.

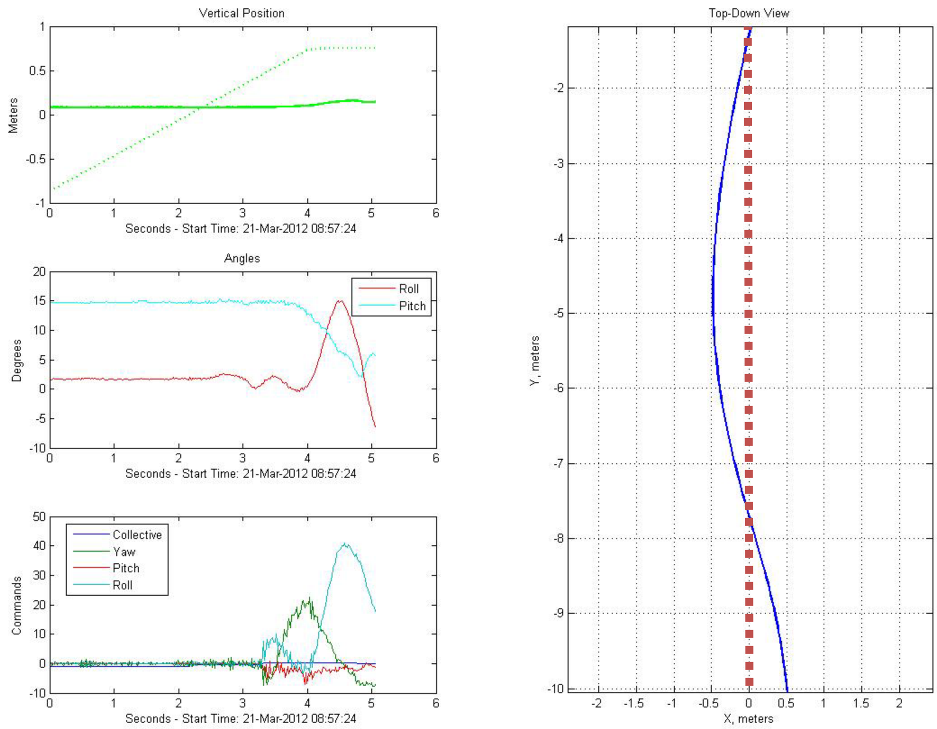

Figure 4-3: High-speed configuration ground run

The commanded path is from bottom to top of the top-down view and right down the middle. Note that as it gets off track, it successfully returns to the desired path smoothly. Also note that as the vehicle's velocity increases, it rotates nose down to lift its tail off the ground as it starts to make lift. This characteristic is common to tail-dragger configuration landing gear such as this. Looking back to the initial configuration development in Chapter 2, we recall that the predicted angle of attack for trimmed flight was approximately 17 degrees. The attitude of the vehicle as it is resting with its tail on the ground is very close to this attitude, but the nose down rotation seen in the data reduces this significantly, this means that in order to rotate and lift off, the vehicle is required to basically hold its tail on the ground until airborne.

After several ground runs were made with acceptable lateral-directional tracking, we attempted to force it to takeoff by commanding a given pitch angle until reaching the desired altitude. As the predicted trim angle of attack is 17 degrees, the initial commanded pitch attitude was set to 20 degrees. Then once airborne, the controller transitioned to altitude hold. Figure 4-4 shows the data for one of the first successful closed loop straight leg flights.

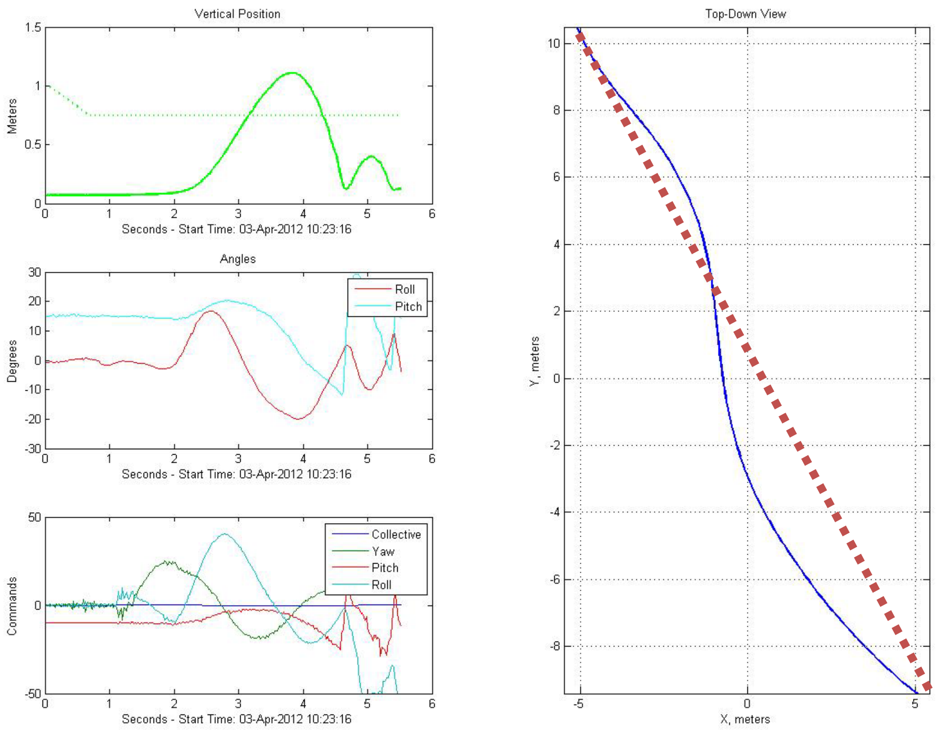

Figure 4-4: High-speed closed loop straight leg flight

Here the commanded path is diagonal from the top left to the bottom right of the top-down view. We see that the lateral-directional tracking performs well. We can also see that in pitch it at first overshoots the commanded altitude around the 3 second mark and then aggressively over corrects, and reaches a nose down pitch angle of approximately 15 degrees to regain the commanded altitude. The overshoots look dramatic on the plot, but they were only about 0.5 meters.

Figure 4-5 shows another successful straight leg flight of the high-speed configuration. This flight came later, when the pitch controller gains had been reduced somewhat based on gull-wing flight tests.

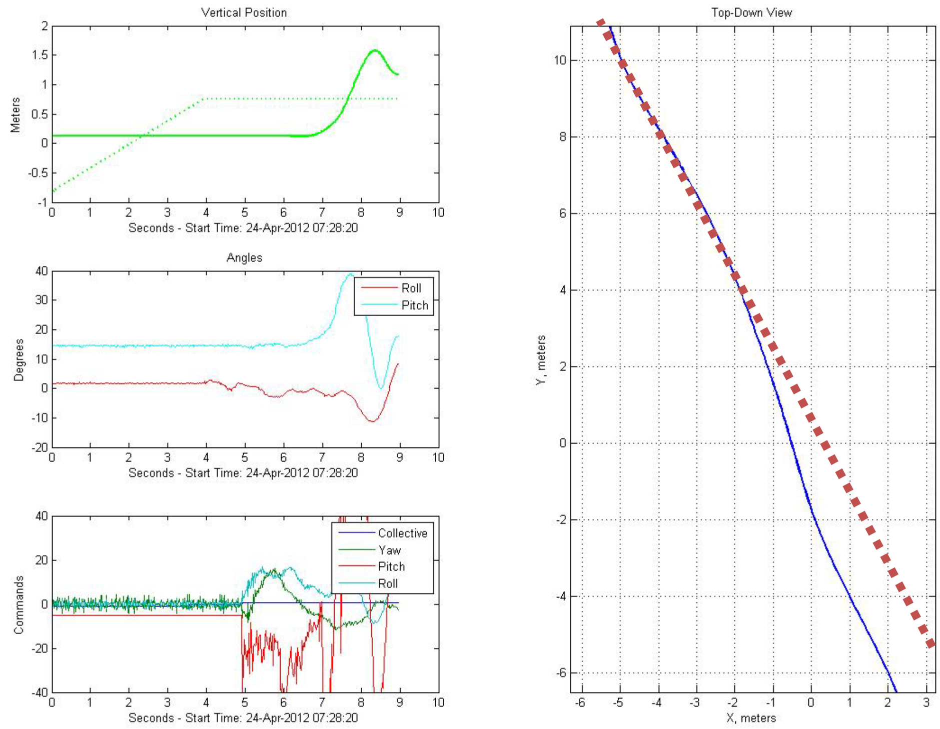

Figure 4-5: High-speed diagonal straight leg with reduced gains

Again the lateral-directional tracking is good, and we can see that the nose down pitch correction following the initial overshoot is not as aggressive. Many other similar straight leg flights were flown at various flight speeds from 6 m/s up to 7.5 m/s. Because the flights were short and relatively dynamic, it is difficult to really call any of the points in trim, but looking at a few points that are close to being in trim, the trim angle of attack was approximately 17.6 degrees a 6.2 m/s with an elevator deflection of about 20 degrees trailing edge up. All three values are slightly higher than predicted as shown in Table 2-2, but in general are very close. This is a strong indication that the VLM is doing a good job of predicting the basic characteristics of the airplane.

The final few flights of the high-speed configuration were an attempt to takeoff in a straight path and then transition into a circular orbit with a 4m radius. Figure 4-6 shows the data from the first such attempt.

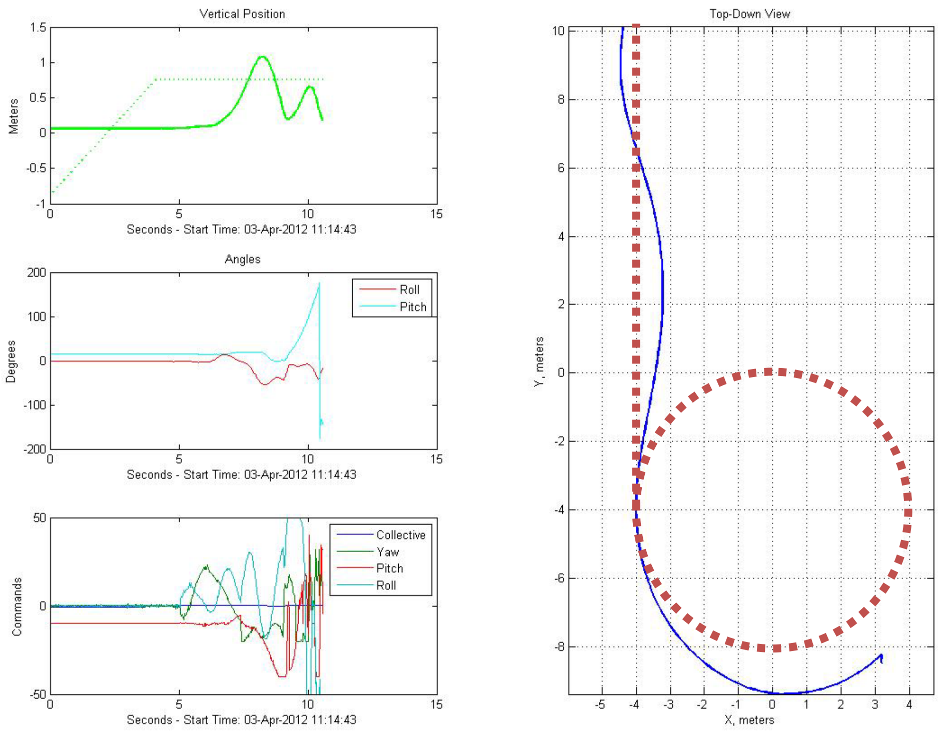

Figure 4-6: High-speed configuration turning flight at 6.0 m/s

As shown in the figure, the airplane does a good job of tracking the lateral-directional path guidance up to the very end. We also see, however, that as the turn begins, the pitch angle grows large, and eventually the airplane stalls, loses altitude, and eventually ends up back on the ground. This indicates that the airplane attempted to turn too tightly resulting in the necessity to command too high of an angle of attack and thus stalling. The wing does not have enough lift capability left to accelerate the vehicle into and around the turn at this airspeed (6.0 m/s).

This problem has a small number of solutions:

- Make the vehicle lighter
- Make the wings bigger (with negligible weight gain)
- Fly in a larger space to allow for bigger diameter turns
- Vary the airspeed to allow for better performance

Since the first 3 options are somewhat difficult, a quick analysis of the vehicle's turning performance was completed. Using the VLM trim routine, the vehicle was trimmed in a

4 m radius turn at various airspeeds in all three of the design configurations. The vehicle was allowed to have nonzero sideslip angle to help it turn, but the total force in the body y-axis was held at zero (coordinated turn constraint see [10]). The trim routine used a commanded earth reference heading rate as its criteria. This turn rate was determined based on the 4 meter turn radius, and the vehicle airspeed. Figure 4-7 shows a plot of the angle of attack required for a 4m radius turn as a function of vehicle airspeed for all three configurations

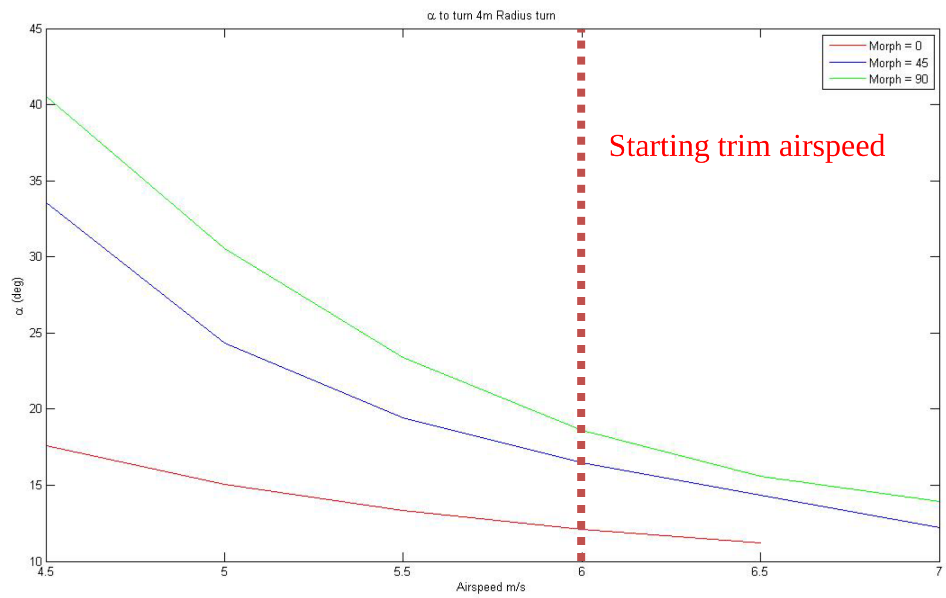

Figure 4-7: Angle of attack required for a 4m radius coordinated turn at a given flight speed

Figure 4-7 indicates that going faster may be a good solution. Assuming that the control inputs required for these trim conditions are not excessive, going faster means a lower baseline angle of attack, and a higher dynamic pressure to create lift in the turn to accelerate the airplane around the turn. To see if this prediction translated into reality more turning flights were conducted at a higher airspeed. The data from one such flight is shown in Figure 4-8.

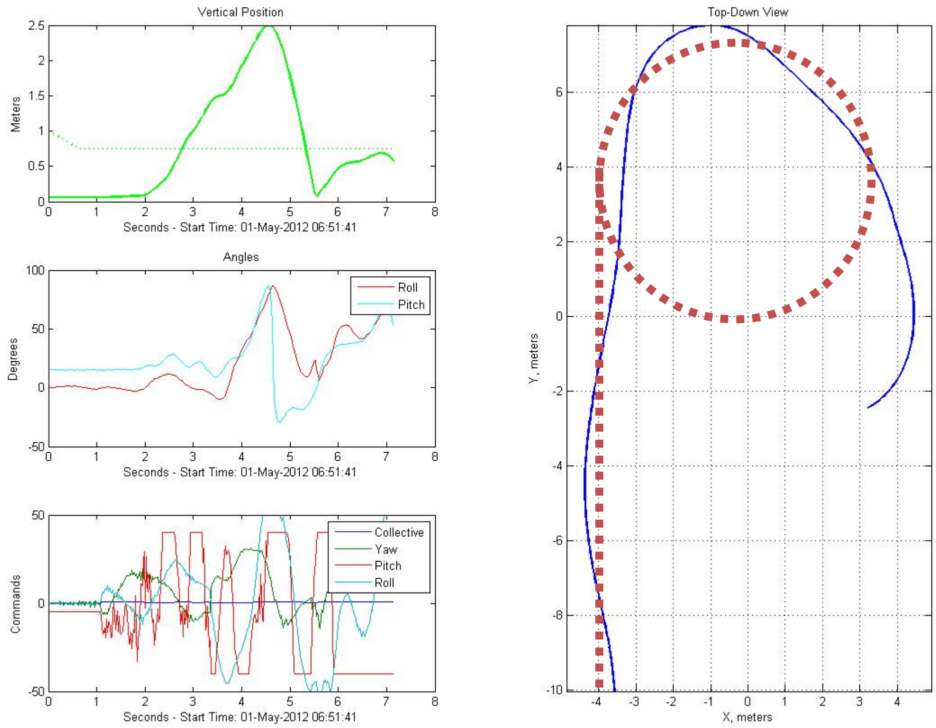

Figure 4-8: High-speed configuration turning flight at 7.5 m/s

While the vehicle did get further around the turn, we see that it still loses significant altitude and again the angle of attack grows very large and the vehicle is again stalled. We also see that the bank angle grows very large (>90 degrees) in the turn. Also evident is that the pitch axis in this condition becomes unstable. The elevator is being commanded from full nose up to full nose down as the vehicle goes around the turn. Further refinements to the vehicle design including reduced weight, improved aerodynamics, and further simulation studies of maneuvering flight are required to successfully complete turns with this configuration.

It is also clear from Figure 4-7 that changing morphing configuration is an even better alternative. At a constant airspeed and turn radius, moving to the gull-wing configuration reduces the required angle of attack, and changing to the low-speed configuration reduces it even further. As was discussed earlier, the low-speed configuration's dynamics are such that its turning performance is limited. In light of this and the data in Figure 4-7, we see that the gull-wing configuration should be an excellent configuration for low-speed maneuvering.

Gull-Wing Configuration

The next configuration flown was the gull-wing configuration. Once again straight leg flights were the first conditions flown. Figure 4-9 shows the test data from the first flight of the gull-wing configuration.

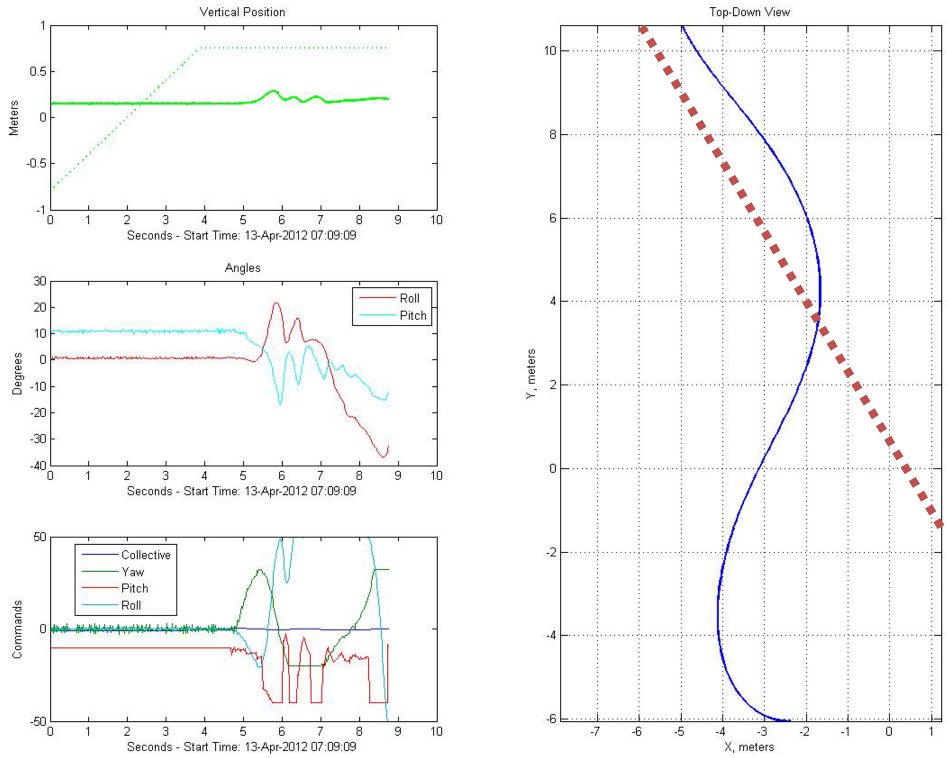

Figure 4-9: Gull-wing configuration first flight

From this data it is apparent that there is a problem. The vehicle shows strong pitch oscillations as indicated by the approximately 3 Hz sinusoid in the pitch angle data at the 6 second mark. It does not show up in the data available, but this 3 Hz oscillation was also coupled into the wing structural modes. As the vehicle pitched up and down, the wings flapped symmetrically. To combat this two changes were implemented: 1) stiffened the structure of the vehicle and 2) turned down the pitch rate feedback gain to 2 instead of nearly 5. This resulted in much better characteristics as is seen in Figure 4-10

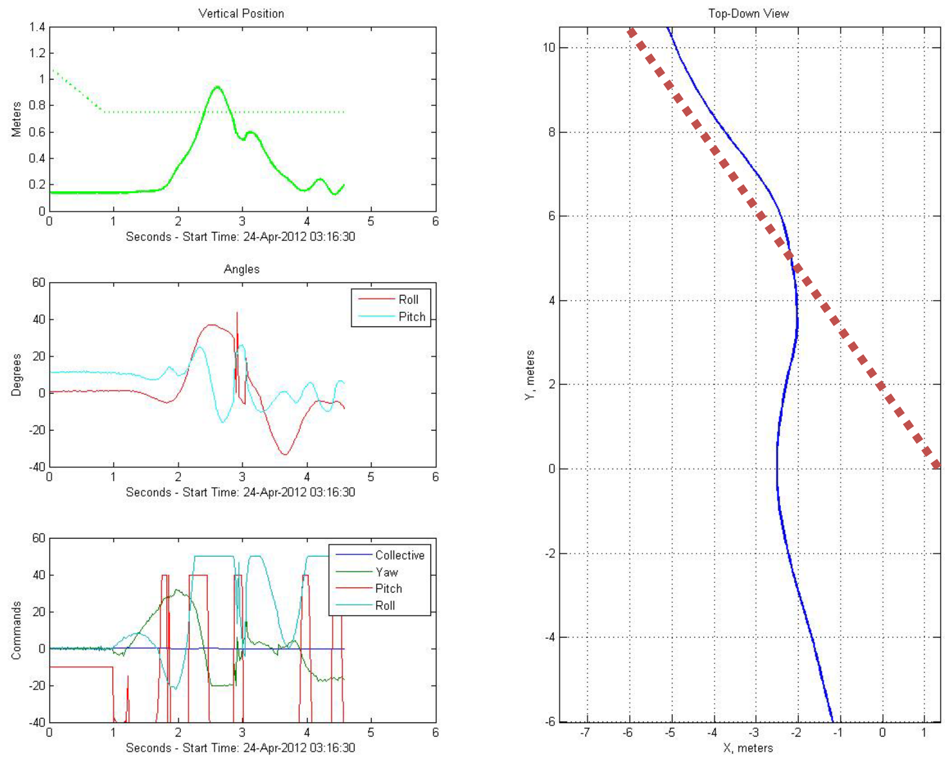

Figure 4-10: Gull-wing flight data with increased structural stiffness and lowered pitch rate feedback gains

Here we see that the magnitude and frequency content of the pitch oscillations are somewhat reduced but still present, and once again as observed by those of us in attendance, the vehicle still flaps its wings right in rhythm. We also see that the elevator commands basically jump from full travel one way to full travel the other way repeatedly (red trace in the graph at lower right). In addition to the structural coupling, this also seems to indicate that this configuration is unstable in pitch, contrary to predictions. This could be caused by the influence of the propeller wash on the surface, a misplaced center of gravity, or issues with the construction method.

Lessons Learned and Future Testing

The capability provided by the VSTL allowed rapid and successful design and flight of a working prototype. Two separate prototypes were flown with only a small amount of effort to get them built and integrated into the lab environment. The hands on aspect of taking an airplane from paper to flight is an invaluable experience and highlighted some of the challenges of building flight vehicles in general and small lightweight vehicles in particular.

In the end, the high-speed configuration proved very capable of straight leg flights under closed loop control. Turn performance was hampered by:

- Airplane ended up too heavy for its wing area. The vehicle was ~50% heavier than other aircraft flown in the VSTL, but with a similar wing area.
- After a few crashes and repairs, the airplane got heavier and the CG became harder to control.
- Insufficient control power for the aggressive maneuvers required.

These issues are solvable through the use of lighter materials, larger control surfaces and further study of the vehicles maneuvering capabilities, possibly through reachability analyses.

The construction method of the gull-wing aircraft resulted in a vehicle that was too flexible and unable to maintain a consistent configuration to allow well controlled flight. Further work needs to be done on improving the structural rigidity of this vehicle while keeping the weight low. Both configurations would benefit from adding camber to the wings. This would allow the wing to produce more lift and increase the stall angle of attack. The camber could also reduce drag and possibly add some rigidity to the wings. Both vehicles would also benefit from refinement of the CG location and wing twist so that more of the available pitch control authority can be used for maneuvering as opposed to trimming for level flight.

The small size of the vehicles created additional challenges that must be kept in mind going forward.

- Small changes in CG location and inertia properties have large effects on vehicle dynamics.
- Small imperfections in the build of the vehicle can create large aerodynamic effects.

Learning from these challenges and the performance of the vehicles to date sets a good foundation for further exploration of the practical issues of morphing flying vehicles in the VSTL.

Chapter 5 - Conclusions and Future Work

In this thesis the stability and control characteristics of a vehicle capable of significant shape change were explored. The vehicle featured a single morphing degree of freedom that allowed it to fold its wings similar to a bird transitioning from soaring low-speed flight to diving high-speed flight. The configuration was sized and analyzed using a vortex lattice code. The design process included initial sizing, basic stability analyses and the design of a lateral-directional control surface mixing scheme. The analyses confirm some of the benefits of morphing; while the low-speed configuration has good aerodynamic efficiency, it has limited control power in the directional axis, a bird or vehicle in this configuration then could benefit from changing shape when encountering gusty conditions or performing aggressive maneuvers.

The resulting linear models of the vehicle were used to design and analyze control laws capable of autonomous flight in Boeing's indoor flight facility – the Vehicle Swarm Technology Lab (VSTL). A linear inner loop control law for the pitch axis was designed that captures and tracks a commanded pitch angle that is issued by the nonlinear guidance control laws implemented in the VSTL. Analysis showed that the pitch control law has acceptable performance and stability margins to control all vehicle configurations without the use of gain scheduling. For the lateral-directional axes, an explicit model following inner loop controller was designed to track a commanded sideslip angle and roll rate and combined with the nonlinear guidance laws in the VSTL to track a commanded bank angle. Controllers designed at one configuration proved to be unacceptable at off design points, so a linear gain schedule based on the morph angle was implemented.

Early flight test results show that the basic design of the vehicle is sound, but prove that the reality of building prototypes and implementing controllers in the real world is a difficult problem. The capabilities provided by the Vehicle Swarm Technology Lab (VSTL) allowed rapid development and flight test of the configuration. Initial vehicle buildup required less than two complete days of work, and the aircraft was successfully flying in the lab on the third day with only minor integration issues. After the initial effort to get the vehicle working properly in the lab, the VSTL allowed a large number of flights to occur rapidly to quickly investigate issues and collect useful data. In the end, the final flight vehicles successfully completed numerous straight leg flights, but due to weight growth and high wing loading, turning flight and continuous maneuvering were not achieved.

Future Work

This project has laid the foundations for a significant amount of future exploration of the concepts and realities of morphing vehicles and as any good research project does, has created more questions than definitive answers. Solidifying the current configuration and getting it flying more successfully are the first steps towards answering some of these other questions.

The fabrication techniques should be re-evaluated to lighten the vehicle and make it stiffer. It would also be beneficial to investigate adding camber to the wing surfaces to increase lift and decrease drag to improve the aerodynamic performance. It may also be prudent to build a vehicle with a more conventional configuration that also includes morphing. Perhaps the vehicle planform developed here as a main wing shape, and add a conventional tail by attaching a boom. This could improve the pitch stability issues and allow for a conventional rudder to be easily included to simplify the lateral-directional control mixing, while still allowing the wing shape to change and providing a useful experimental research platform for further investigation into morphing.

Once the vehicle flies successfully it opens the door to exploring other aspects and challenges of morphing vehicles. One area is the investigation of the unsteady aerodynamics and inertial effects associated with the configuration change. The VSTL has several system identification tools that could allow different sets of sweeps to be run to determine the parameters of a given model of the dynamics. The models developed could then be fed back into the simulation to allow better design of controllers to take these effects into account. With better models of the morphing dynamic effects comes better and deeper research into the applicability of adaptive control techniques to the control of these vehicles. In particular, the concurrent learning techniques described in [24] sound like a promising extension of adaptive control that would be well suited to a morphing vehicle.

Another area of interest is control mixing. This project employed a fairly simple lateral control mixing design process to attempt to maintain consistent control derivatives as the morphing configuration changed. Others have implemented online optimal control mixing techniques that could be used instead that could improve the performance of the vehicle and the control laws in each configuration, for example see [20] and [21]. The addition of varying control effectiveness as a function of the morphing angle adds a new twist to this type of problem and is one that could easily be explored further with a working morphing vehicle in the VSTL.

The other control mixing area of interest is maintaining linearity of the control derivatives throughout the full travel range of the virtual effectors. The VLM models used forced this issue by using small perturbation dynamics, but in general with large surface deflections, the control effectiveness may not always be linear. Designing a mixer that enforces this linearity across the entire virtual command range (as well as across morphing configurations) is an important aspect of guaranteeing linear controller performance in dynamic maneuvers. The configuration developed here would also be a good platform for investigating these techniques further.

As the analyses above show, the control capability of the vehicle greatly changes as the morph angle is varied, the high-speed configuration is capable of more aggressive maneuvering than the low speed configuration because of its increased directional stability and directional control power. The gull-wing configuration offers a good balance between the aerodynamic capabilities of the low-speed configuration with the control power and stability of the high-speed configuration. It is easy to envision scenarios where changing the morphing configuration could thus be used to improve mission performance. A vehicle that is in a long loiter pattern could maximize its endurance by operating in the low-speed configuration, but if it gets struck by a gust, changing to the gull-wing configuration would allow it to reject the disturbance more quickly. A vehicle that needs to make a rapid course change could maximize its performance by changing to the high-speed configuration. Alternatively, asymmetric configuration changes could be made to allow for very aggressive maneuvers or gust rejection. Perhaps one configuration outperforms the others during takeoff and landing. The flexibility of the configuration changes and the related changes in the flight dynamics opens up new possibilities for enhancing operational performance. It would be interesting to explore these ideas along with control algorithms that take these characteristics into account and automatically adjust the configuration for different flight phases, gust encounters, upcoming flight path requirements, etc.

References

1. Norris, Guy, “Boeing Unveils Plans for Trailing Edge Variable Camber on the 787 to Reduce Drag, Save Weight.” Flight International Online, June 12, 2006. http://www.flightglobal.com/news/articles/boeing-unveils-plans-for-variable-camber-on-787-to-reduce-drag-save-207172/ .

2. Yue, T., Wang L. and Ai J., “Multibody Dynamic Modeling and Simulation of a Tailless Folding Wing Morphing Aircraft.” AIAA Atmospheric Flight Mechanics Conference 2009. AIAA 2009-6155.

3. Obradovic, R. and Subbarao, K., “Modeling of Flight Dynamics of Morphing-Wing Aircraft.” Journal of Aircraft; Vol. 48, No. 2, March-April 2011.

4. Halass, D. and Bieniawski, S., “Guidance & Control of Micro Air Vehicles: Rapid Prototyping & Flight Test.” AIAA Guidance, Navigation, and Control Conference 2010. AIAA-2010-8415.

5. Seigler, T. and Neal, D. et al, “Modeling and Flight Control of Large-Scale Morphing Aircraft.” Journal of Aircraft; Vol. 44, No. 4, July-August 2007.

6. Seigler, T., “Dynamics and Control of Morphing Aircraft.” PhD Dissertation at Virginia Polytechnic Institute and State University, August 2005.

7. RC Foam Website., http://www.rcfoam.com/stpg/php?page_id=depron_epp_density. Accessed February 2nd, 2012.

8. Vortex Lattice Utilization, NASA SP-405, NASA, Washington, D.C. 1976.

9. Moran, J., An Introduction to Theoretical and Computational Aerodynamics, John Wiley & Sons, 1984.

10. Stevens, B. and Lewis F., Aircraft Control and Simulation 2nd Edition, John Wiley & Sons, 2003.

11. Rodriguez, A. “Morphing Aircraft Technology Survey.” 46th AIAA Aerospace Sciences Meeting and Exhibit 2007. AIAA 2007-1258.

12. Smetena, F., Computer Assisted Analysis of Aircraft Performance, Stability, and Control, McGraw-Hill College, 1984.

13. Thompson, C., Coleman, E., and Blight, J., "Integral LQG Design for a Fighter Aircraft," AIAA Guidance, Navigation and Control Conference, AIAA, New York, 1987, pp.866-895.

14. Dorato, P., Abdallah, C. T., and Cerone, V., Linear Quadratic Control: An Introduction, Kreiger Publishing Company, Malabar, Florida, 2000.

15. Lehtomaki, N., Sandell, N., and Athans, M., "Robustness Results in Linear-Quadratic Gaussian Based Multivariable Control Designs," IEEE Transactions on Automatic Control, Vol. AC-26, No. 1, IEEE, 1981.

16. Gadient, R., Levin, J., and Lavretsky, E. "Comparison of Model Reference Adaptive Controllers Designs Applied to the NASA Generic Transport Model," AIAA Guidance, Navigation, and Control Conference , AIAA, Toronto, Ontario, Canada, 2010, AIAA-2010-8406.

17. Lavretsky E., "Adaptive Control: Introduction, Overview, and Applications," Course Notes: IEEE Robust and Adaptive Control Workshop, St. Louis, MO.

18. Hovakimyan, N, Cao, C., Kharisov, E., Xargay, E., Gregory, I. M., "L1 Adaptive Control for Safety-Critical Systems," IEEE Control Systems Magazine, October 2011.

19. Chen, C, Linear System Theory and Design, 3rd Edition, Oxford University Press, New York, New York, 1999.

20. Yang, L. and Shen, G., "A New Optimal Control Allocation Method for Aircraft with Multiple Control Effectors," AIAA Aerospace Sciences Meeting and Exhibit, AIAA, Reno, Nevada, 2007, AIAA 2007-1052.

21. Gundy-Burlet, K., Kreshnakumar, K., Limes, G. and Bryant, D., "Control Reallocation Strategies for Damage Adaptation in Transport Class Aircraft," AIAA Guidance, Naviagtion, and Control Conference, Austin, Texas, 2003, AIAA 2003-5642.

22. Saad, E., Vian, J., Clark, G., and Bieniawski, S., "Vehicle Swarm Rapid Prototyping Testbed," AIAA Infotech@Aerospace 2009 Conference and Exhibit, 6-9 April 2009, AIAA, Seattle, WA, 2009, AIAA 2009-1824.

23. VICON Website: http://www.vicon.com.

24. Chowdhary, G. and Johnson, E., "Concurrent Learning for Improved Convergence in Adaptive Flight Control," AIAA Guidance, Navigation, and Control Conference, Toronto, Ontario Canada, 2010, AIAA 2010-7540.

25. Lavretsky, E. and Hovakimyan, N., "Positive μ-modification for Stable Adaptation in the Presence of Input Constraints," Proceeding of the 2004 American Control Conference, Boston, MA, 2004.